FABRICATION OF METAL/OXIDE NANOSTRUCTURES BY ANODIZATION PROCESSES FOR BIOSENSOR, DRUG DELIVERY AND SUPERCAPACITOR APPLICATIONS

A Dissertation

by

PO-CHUN CHEN

Submitted to the Office of Graduate and Professional Studies of
Texas A&M University
in partial fulfillment of the requirements for the degree of

DOCTOR OF PHILOSOPHY

Chair of Committee,	Jun Zou
Co-Chair of Committee,	Sheng-Jen Hsieh
Committee Members,	Robert Balog
	Xing Cheng
Head of Department,	Chanan Singh

May 2014

Major Subject: Electrical Engineering

ABSTRACT

This dissertation proposed to initiate the research into the fabrication of metal/oxide nanostructures by anodization process for biosensor, drug delivery and supercapacitor applications by producing different nanostructures which lead to the potential for various applications. This study focuses on the establishment of the knowledge and techniques necessary to perform metal/oxide nanostructures on biological and energy applications. This study will investigate: (1) the sensor and drug delivery applications of micro/nano structures; (2) novel processes to innovate anodic aluminum oxide nanotube template; (3) the supercapacitor applications of anodic titanium oxide.

First, the extremely high surface area AAO coated microneedle and microneedle array can be developed as sensor and drug delivery devices. Due to the large surface area of the AAO, the film can absorb indicators to make it sensitive to testing targets. pH detection was demonstrated to show the sensing capability of the microneedle. Then, the microneedles were further built as an array by combining micromachining technique. The microneedle array provides a 3-D structure that possesses several hundred times more surface area and capacity than a traditional nanochannel template. Second, the nanoengineering process was conducted to innovate anodic aluminum oxide nanotube template. Guided anodization assisted by nanoimprint process formed AAO arrays that can be formed on controlled locations. More importantly, it shows the periodically ordered AAO array with different sizes of nanopores. With the improved AAO template, melting injection, electro/electroless deposition and sol-gel deposition were conducted to fabricate Ni nanowires/ TiO_2 nanotubes, Ni/$BaTiO_3$ core-shell nanotubes, and UHMWPE nanotubes. Third, various Ti-based alloys

were anodized to form ordered nanotubes for supercapacitor application. Ti alloy oxide contains some porous layers which are not presented on TiO_2 nanotube film. Thus, Ti alloys anodized oxide nanotubes have better supercapacitor behaviors than the conventional TiO_2 nanotubes. However, a high surface area nanoporous Ti/TiO_2 structure, which was fabricated by selective etching process, can accumulate large quantity of electrons and energy for supercapacitor needs. Additionally, nanoporous metals obtained by dealloying hold a unique combination of a highly conductive network and a bicontinuous open. The characteristics formed through dealloying also present a nice charge/discharge behavior and a good capacitance performance.

DEDICATION

To my parents and my wife

ACKNOWLEDGEMENTS

I would like to convey my sincerest gratitude to my advisors, Dr. Zou and Dr. Hsieh, who provide great help, guidance and support on this research. I also would like to to thank Dr. Balog, Dr. Cheng, and Dr. Kameoka for serving on my committee members and giving valuable comments on my research work and dissertation.

Thanks also go to the department faculty and staff at Texas A&M University for their help. I also want to extend my gratitude to TAMU Microscopy Imaging Center and TAMU Materials Characterization Facility for the use of SEM, and nanoindentor.

Especially, I am very grateful to all my colleagues, Alex, Issac, Henry, and Young in Dr. Zou's group for their help during my graduate years.

Finally, I would like to express my deepest appreciation to my father, mother, and sister for their support and encouragement and to my lovely wife Nikki for her patience, assistance, and love.

TABLE OF CONTENTS

Page

ABSTRACT ii

DEDICATION iv

ACKNOWLEDGEMENTS v

LIST OF FIGURES viii

LIST OF TABLES xi

1. INTRODUCTION 1

1.1 Background 1
1.1.1 Porous Metal and Metal Oxide Nanostructures 1
1.1.2 Applications for Biosensing and Drug Delivery 3
1.1.3 Applications for Supercapacitors 3
1.2 Dissertation Statement and Overview 4

2. BACKGROUND AND LITERATURE REVIEW 6

2.1 Background 6
2.1.1 Surface Treatment 6
2.1.2 Material Characterization Technique 8
2.2 Literature Reviews 9
2.2.1 Anodic Metal Oxide Nanostructures 9
2.2.2 AAO for Biosensing and Drug Delivery Applications 17
2.2.3 Capacitors for Energy Storage Applications 23

3. 3-D MICRONEEDLE AND MICRONEEDLE ARRAY WITH NANOPOROUS SURFACE 31

3.1 Introduction 31
3.2 Single AAO Microneedle 33
3.2.1 Experimental Work 33
3.2.2 Results and Discussion 34
3.3 AAO Microneedle Array for Drug Delivery 36
3.3.1 Experimental Work 36
3.3.2 Results and Discussion 37
3.4 Application in pH Sensing 41
3.5 Conclusion 43

4. AAO TEMPLATE NANOENGINEERING AND FABRICATION OF HYBRID NANOSTRUCTURES 45

4.1 Introduction 45
4.2 Hybrid Nanowire and Nanotube Fabrication 47
4.2.1 Experimental Work 47
4.2.2 Results and Discussion 51
4.3 Nanoengineering of the AAO Templates 55
4.3.1 Experimental Work 55
4.3.2 Results and Discussion 56
4.4 Conclusion 60

5. ANODIC TITANIUM BASED ALLOY OXIDE NANOTUBES 61

5.1 Introduction 61
5.2 Experimental Work 62
5.2.1 Materials and Methods 62
5.2.2 Electrolytic Characterization 64
5.3 Discussion and Conclusion 64

6. SELECTIVELY DEALLOYING Ti/TiO_2 NANOSTRUCTURE FOR SUPERCAPACITOR APPLICATION 77

6.1 Introduction 77
6.2 Experimental Work 79
6.2.1 Dealloying and Oxidation of NiTi Alloy 79
6.2.2 Electrolytic Characterization 79
6.3 Discussion and Conclusion 81

7. SUMMARY AND FUTURE WORK 87

7.1 Summary 87
7.2 Future Work 89

REFERENCES 90

LIST OF FIGURES

Page

Figure 1 Chart of surface treatment 6

Figure 2 Schematic diagram of the anodizing cell..... 11

Figure 3 The schematic of electric field and ion concentration on aluminum surface during anodization..... 13

Figure 4 The schematic diagram of AAO self-repair mechanism 14

Figure 5 The flow chart of two-step anodization process..... 15

Figure 6 The schematic diagram of the titanium anodic oxides 17

Figure 7 Schematic diagrams of types of sensing mechanism 20

Figure 8 Schematic diagrams of AAO for drug deliver..... 22

Figure 9 Schematic diagrams of (a) MIM capacitor and (b) electrolytic capacitor..... 26

Figure 10 Schematic diagram of mechanism of EDLC 27

Figure 11 Ragone Plot [107] © SAE International..... 29

Figure 12 SEM images of aluminum microneedle 35

Figure 13 Schematic diagram of the growth mechanism of AAO microneedle..... 35

Figure 14 Schematic diagrams of Al micropillar and microneedle arrays 36

Figure 15 SEM images of aluminums microneedle array 38

Figure 16 SEM images of the results of anodization on the indented aluminum 40

Figure 17 Schematic diagram of filling metals or polymer into micro/nano female mold..... 41

Figure 18 Images of 6061 Al rods morphologies 42

Figure 19 Images of microneedles covered by AAO..... 43

Figure 20 Schematic diagram of hybrid nanostructure fabrication 48

Figure 21 Schematic diagram of Ni/$BaTiO_3$ core-shell structure fabrication process..... 50

Figure 22 Schematic diagram of polymer melting injection 51

Figure 23 SEM images of Ni nanowire/ TiO_2 nanotube structure..... 52

Figure 24 SEM images and EDX results of $BaTiO_3$ nanotubes and Ni/BaTiO3 core-shell nanotubes..... 53

Figure 25 SEM images of UHMWPE nanotubes 54

Figure 26 SEM images of imprint mold; (a) pillar size of 120 nm and inter-distance of 240 nm, (b) pillar size of 160 nm and inter-distance of 360 nm, (c) vacancy size of 240 nm, and (d) vacancy size of 360 nm..... 56

Figure 27 Images of optical microscope of electropolished aluminum pieces; (a) un-annealed, (b) annealed..... 57

Figure 28 SEM images of imprinting mold of 160 nm pillar size with 120 nm pillar insertion; (a) every 3 pillar and (b) every 4 pillar..... 58

Figure 29 SEM images of AAO with different pattern; (a) smaller indentations surrounded by larger ones and (b) replace some smaller pores by larger ones..... 58

Figure 30 SEM images of AAO from inserting vacancies into patterns; a vacancy inserted (a) in every 3 indentations and (b) in every 4 indentations 59

Figure 31 SEM images of TiO_2 NT; (a) an unwanted film cover on TiO_2 NT, (b) removed partial unwanted film, (c) removed all unwanted film and presented TiO_2 NT, (d) TiO_2 NT side view, (e) TiO_2 NT bottom view, and (d) an barrier layer on the TiO_2 NT bottom..... 63

Figure 32 Pourbaix diagrams of (a) Ti, (b) Ta, and (c) Mo..... 65

Figure 33 SEM images of Ti-Ta NT film structure; (a) compact layer, (b) partial porous film, (c) porous film (d) net film, (e) Ti-Ta NT. 68

Figure 34 SEM images of TiO_2-Ta_2O_5 nanotubes film by anodizing Ti-20Ta alloy; (a) a net film on the NT top, (b) without a net film on the NT top, (c) a barrier layer on the NT bottom, (d) partial barrier layer on the NT bottom 69

Figure 35 SEM images of TiO_2-MoO_3 nanotubes film by anodizing Ti-10Mo alloy; (a) a top view of the net structure, (b) without a net film on the NT top, (c) smaller pores nanotubes, (d) barrier layer on the bottom 70

Figure 36 The schematic diagram of TiO_2-Ta_2O_5 NT or TiO_2-MoO_3 NT film structure; (a) compact layer, (b) partial porous film, (c) porous film (d) net film, (e) TiO_2-Ta_2O_5 NT or TiO_2-MoO_3 NT and barrier layer on the Ti-Ta or Ti-Mo alloy 71

Figure 37 Estimation of TiO_2 NT surface; (a) cone structure of inner tube with radius of R_3, and $R_{1,}$ and R_2 on the tube top and bottom, tube length with H (b) pore wall thickness with T_1 and T_2 on the tube top and bottom, (c) tube inner surface area, and outer surface area..... 72

Figure 38 Accumulated anodic Ti and Ti alloy NT inner and outer surface areas based on $1cm^2$ substrate..... 73

Figure 39 Capacitance performance evaluations for TiO_2 NT, TiO_2-10 Ta_2O_5 NT, TiO_2-20 Ta_2O_5 NT, and TiO_2-10 MoO_2 NT by Cyclic Voltammograms..... 75

Figure 40 SEM images of dealloyed nanoporous structures 80

Figure 41 XRD results of raw nitinol, dealloyed nitinol, pre-annealing and annealed samples 83

Figure 42 Cyclic Voltammogram (CV) curve of raw nitinol, pre-annealing, and annealed samples 84

Figure 43 (a) C-V curves and (b) schematic diagrams of structures comparison with dealloyed nanoporous TiO_2 and TiO_2 nanotubes 85

LIST OF TABLES

Page

Table 1 EDS results of Ti alloys oxide nanotubes 74

Table 2 Specific capacitance based on TiO_2 NT, Ti-10Ta NT, Ti-20Ta NT, and Ti-10Mo NT films 76

Table 3 Composition of Ti/Ni alloy 82

1. INTRODUCTION

1.1 Background

The main purpose of this dissertation is to initiate our research into “Fabrication of metal/oxide nanostructures by anodic process for sensor, drug delivery and supercapacitor applications” by producing different kinds of nanostructures which are fit for various applications. Before going in depth of this research, this subsection introduces a brief background of porous structure, biosensing and drug delivery, and supercapacitor nanotechnologies. These contents are important for better understanding of the purpose in this dissertation.

1.1.1 Porous Metal and Metal Oxide Nanostructures

Nanoporous materials have been widely investigated for various applications due to the high surface area, such as catalysis, sensors and energy devices. Metallic nanoporous structure is especially suitable to create continuous network for electronic transfer. Other than that, nanoporous metallic materials have useful unique properties, such as large surface-to-volume ratio, light weight, and excellent electrical/thermal conductivity. They are able to improve performance in chemical, electrical, optical behaviors, and they also can be used in catalysis, mircofiltration, sensors, drug delivery system. [1-5]

Various approaches have been approved to fabricate nanoporous metals and [6, 7] among these processes, selective removing is a promising method to generate uniform metallic nanoporous structures. Materials for selective removing are prepared by two well-mixed components, such as metal/oxide [8], metal/metal [9], and metal/polymer. [10]

Selective removing process is based on the difference of the stability of the two components, and it can be done through thermal, chemical and electrochemical processes. For instance, a three-dimensional colloidal crystal structure can first be filled with metal to form a continuous metal network. The colloidal nanosphere can then be removed by either thermal or chemical process to form a continuous metal nanoporous structure. The size and uniformity of the nanoporous structure can be easily controlled by the size of nanosphere and the arrangement of the colloidal crystal structure, respectively. Ni inverse opal nanoporous structure was fabricated by thermally removing polystyrene colloidal crystals. [11] However, there are some limitations to this method. For example, the metal filled into the 3-D colloidal crystal structure by chemical reduction, such as electroplating and electroless deposition. Thus, metals with high reduction potentials are very difficult to fill, such as Al and Ti.

Another selective removing method, dealloying, has been demonstrated to be very effective in generating free-standing 3-D nanoporous metals. Unlike traditional nanoparticle-based materials, nanoporous metals obtained by dealloying hold a unique combination of a highly conductive network and a bicontinuous open nanoporousity. Various nanoporous metals can be obtained by dealloying process, such as Al, Ti, Cu etc. Additionally, pore size and porousity can be determined by mechanical methods or heat treatments, such as rolling, and annealing. Dealloying in aqueous solution is a promising technique for preparing homogeneous nanoporous metals. Dealloying results are affected by many parameters, such as alloy composition, solution composition, temperature, and treatment time. Some alloy systems have been investigated to form uniform nanoporous structure, for example, Au/Zn, Au/Cu, Au/Ag, Pt/Si, Pt/Cu, and Al/(Au,Ag,Pd), etc. [12-17] Therefore, various metals

nanoporous structures can be generated in order to create different desired characteristics, such as high surface area and continuous conducting network.

1.1.2 Applications for Biosensing and Drug Delivery

Nanomaterials have unique properties which have developed into many biotechnology applications. In fact, nanomaterials are the smallest structures can be used for efficiently transport of electrons. A general nanomaterial property is exceptionally large surface area. In particular nanoporous materials have an advantage of high aspect ratio that can be applied on purification, separation, sensor and detection. First of all, nanomaterials have been demonstrated that it can be used for bio-sensing applications. Biosensors are the devices, which can produce optical, electrical or thermal output signals for further analysis. The biosensors can be defined by sensing aspect, such as DNA, proteins, glucose, microorganisms and even tissues. Additionally, nanostructures have been widely investigated as devices for drug delivery applications. The purpose of controlled drug delivery is to manage the necessary amount of drug to specific sites in the human body safely and effectively.

1.1.3 Applications for Supercapacitors

Nanomaterials contribute many improvements and developments to supercapacitors. There is a rising need for capacitors that can accumulate a large quantity of energy and then deliver it rapidly. A variety of military, aerospace, and commercial applications need this type of energy storage which can provide enough power with minimal reaction time. Moreover, these applications often require higher power and energy densities as well as higher charge/discharge rates. This growing demand has led to the creation of the

supercapacitor, which is an electrochemical double layer capacitor (EDLC). The charge storage mechanism includes double layer capacitance and pseudo capacitance. Pseudo capacitance involves electron transfer reactions, and when redox (the Faradaic reaction) occurs in the electrodes it made generating higher power and energy densities possible. However, nanomaterials have the potential to improve the performance of various types of capacitors. Nanomaterials with large surface areas can provide larger interface for forming double layer to charge/discharge in EDLCs. [18] Nanostructures also provide the possibility for a better mechanism for ion transportation in the redox reaction. These properties of capacitive nanomaterials can be applied to supercapacitors for a better and improved performance. [19]

1.2 Dissertation Statement and Overview

As introduced above, nanostructures have been widely investigated in biology and energy technologies. However, the current fabrication processes being used in these applications appear to be too complicated. Therefore, we propose to conduct anodization processes to develop nanostructures for biology and energy applications. Furthermore, several improvements for these applications can be achieved by our efforts on combining anodization and micromachining processes.

The goal of this dissertation is to establish knowledge and techniques necessary to perform metal/oxide nanostructures on biological and energy applications. This study will investigate: (1) the biological applications of micro/nano structures; (2) novel processes to innovate anodic aluminum oxide nanotube template; (3) the energy storage applications of anodic titanium oxide. To accomplish this goal, different electrochemical processes are

conducted to fabricate micro/nano structures, such as electrochemical polish, anodization, selective etching, etc. Micromachining techniques and e-beam lithography also play assisting roles to achieve our proposed results.

This dissertation contains seven chapters. Section 1 introduces the background and motivation of this dissertation, followed by the research objective and overview. In addition to literature reviews, Section 2 offers information required for better understanding of the contents of this dissertation. The contents include fabrication and characterization techniques and literature reviews. Section 3 shows the development of a microneedle with nanostructure by combining different electrochemical processes. [20] We further expand this micro/nano structure to build a 2-D array device. [21] Section 4 focuses on nanoengineering processes that can improve anodic aluminum oxide nanotube (AAO) template, and various hybrid nanowires and nanotubes that are fabricated with the help of AAO template. Section 5 studies the enhancement of capacitance performance of anodic titanium oxide nanotubes from titanium base alloys. [10] Section 6 demonstrates a selective etching process for producing a high surface area nanoporous structure for supercapacitor application. Final conclusions and future works are described in Section 7.

2. BACKGROUND AND LITERATURE REVIEW

2.1 Background

To better understand the contents presented in this dissertation, prerequisite knowledge regarding several different aspects of fabrication and characterization technology is required and provided in this subsection.

2.1.1 Surface Treatment

Understanding the surface treatments is important to have a clear idea how these processes assist to reach our expecting results. A chart of surface treatments is shown in Fig. 1, and there are two major categories which are removal and oxidation.

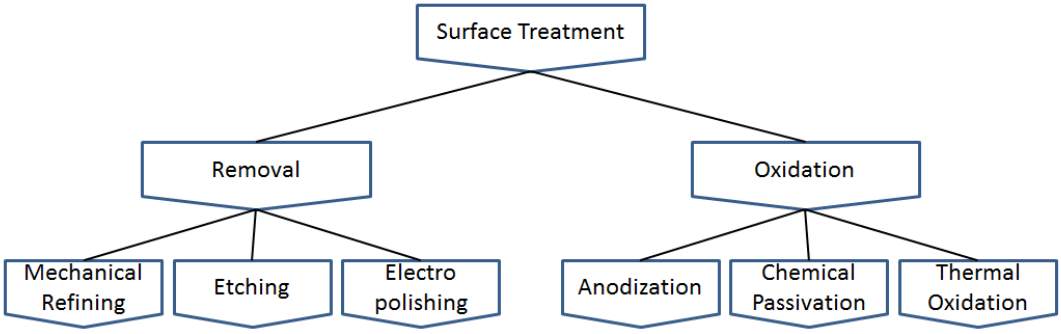

Figure 1 Chart of surface treatment

The first major surface treatment method is removal, including mechanical refining, etching and electropolishing. Mechanical refining usually starts from steps of grinding with hard materials, such as Al_2O_3, SiO_2, WC and diamond. Mechanical refining usually follows

by polishing, which is a process to encourage the surface mobility to reach a smooth surface. Another removal treatment is etching, that includes shifting of pH-value and complexation. The thermodynamic stability of materials with pH-value can be referenced from the Pourbaix-diagram. Etching rate could be increased by adding aggressive agents (acid or alkaline) in order to accelerate pH-value shifting and break the thermodynamic stability. Complexation reaction occurs at the interface between substrate and solution, and it causes a high concentration gradient to increase etching rate. [22] Chemical polishing is a typical etching technique to level substrate surface since higher dissolution rates happen at the rough spot. However, chemical polishing is not able to flatten all metals because some substrates, such as Ti and Al, have passive oxide layers that protect films from corrosion. Electropolishing is therefore more useful for flattening the metal substrate. The polishing occurs at the anode, and the reaction drives the equilibrium in Eq. 2-1 to the right to dissolve metal. The dissolution rates change with modifying applied voltages until smooth plane appears.

$$Me \rightarrow Me^{n+} + ne^{-} \qquad \text{(Eq. 2-1)}$$

The other major surface treatment is oxidation, which includes anodization, chemical passivation, and thermal oxidation. Anodization will be stated more in Section 2.2, anodization is an electrolytic process to grow a dense oxide layer on the metal surface. Chemical passivation usually happens when a strong etching agent is present, and the reactions are controlled by concentrations and bath temperatures. Lastly, thermal oxidation is a process that operated in 200°C or higher. Oxidation time, air composition and temperature can all contribute to influence the thickness and the composition of thermal oxide.

2.1.2 Material Characterization Technique

Material characterization of the micro/nano structure is a main focus of this dissertation, and this portion will cover some of the techniques used to characterize these features. Information and properties of our fabrications, such as thickness, feature size, morphology, elemental composition, and crystal structure, are crucial to understanding the micro/nano structure of the material. Three major techniques that are primarily used in this dissertation, SEM, XRM and EDS, are discussed below.

The surface images of the morphology of micro/nano structures can be acquired by scanning electron microscopy (SEM). The SEM utilizes a high-energy electron beam to scan the specimen surface. [23] A variety of signals, typically including secondary electrons, back-scattered electrons, and photons, are produced when the energetic electrons interact with the specimen. Moreover, these signals are collected to produce a 2-D image containing the information about the material surface morphology. FEI Qunta 600 and JEOL JSM-7500, located in Texas A&M University, were utilized to inspect the topography of our micro/nano structures. The resolution is 1 nm at 15 kV electron beam accelerating voltage for both instruments. The magnification ranges from 25x to 600,000x in the SEM mode.

X-ray Diffraction (XRD) is able to determine the atomic and molecular structure of our testing specimen by measuring the angles and intensities of the diffracted beams. Excited metal target (Cu is the most common) generates incident X-ray with specific wavelengths, and the incident X-ray interacts with the specimen surface. At certain angles, the incident X-ray impinging the testing sample satisfies the Bragg Equation, constructive interference occurs and a peak shows. [24] The patterns (angles and peaks) can identify the sample composition and crystalline structure. Bruker D2 PHASER was operated for characterization,

and the scanning range is from 10 degree to 80 degree at 0.05 degree/s of scan rate in this study.

Elemental analysis of a specimen can be done by energy dispersive X-ray spectroscopy (EDX, or EDS). It works dependently on the interaction between the excited X-ray and the sample. The abilities of characterization are based on the concept that every element has a unique atomic structure allowing a unique set of peaks on its X-ray spectrum. [25] When a high-energy beam is focused on our test specimen, the signal received by the energy-dispersive spectrometer can determine the composition of the testing specimen. Oxford EDS system was used for analyzing the composition of our testing specimen in this dissertation.

2.2 Literature Reviews

The first part of this subsection presents anodization and anodic oxide nanostructures. In addition, some innovative anodization process is also included. The second part introduces the biosensing and drug delivery applications with AAO nanostructure. The third part includes capacitor applications with anodic oxide nanostructures.

2.2.1 Anodic Metal Oxide Nanostructures

Anodization is an electrolytic process used to grow a passive layer on the metal surface at the anode. Metals, which can be anodized, are able to form a thin oxide film in oxygen-contented ambient. The dense and uniform layer of anodized oxide inhibits ionic conductivity, thus they can be regarded as barrier oxides to effectively protect the metal from further corrosion. [26] On top of that, the anodized oxide film can improve the surface properties of metal, such as wearing, galling, adhesion, and dielectric layer. Transition metals

are a common source for materials used in anodization, metals such as Al, Ti, Mg, Zn, Ta and W are often used during anodization process. Interestingly, some anodized metal oxide films can also be applied as decorations since the colors of anodized films are variable, also called interference layer. [27]

Fig. 2 shows an anodization cell, the working metal is set as the anode to oxidize during the electrochemical process. The cathode can be any electronic conductor that would not react in the anodizing bath. The electrolytes are chosen by the insolubility with the anodized oxide, or a higher growth rate of oxide when compared to its dissolution rate. When the reaction is taking place, electrons are withdrawn from the metal at the positive terminal, allowing ions at the metal surface to react with the water in electrolyte to form a dense oxide layer on the metal. The electrons later return back to the electrolyte where they react with hydrogen ions to generate hydrogen.

Many properties of these transition metals anodic oxides become more and more important when we explore the possibilities on a micro or nano scale. Anodic oxide films, with the inherent nanoporous structure, exhibit high surface area, and short solid-state diffusion path for catalysis, electrochemical devices, and energy applications. The other advantage of the anodic oxide micro/nano structures is that the fabrications are achieved by chemical or electrochemical processes that are relatively simple and cost effective. The morphologies of anodic oxides include powders, rods, wires and tubes. Materials ranging from Al, Ti, Zr, W to Ta have all been investigated to form self-assembly nanotubes structures. [28] Among these transition metals oxide nanotubes, anodic aluminum oxide (AAO) and anodic titanium oxide (ATO) are among the most widely studied for their functional properties.

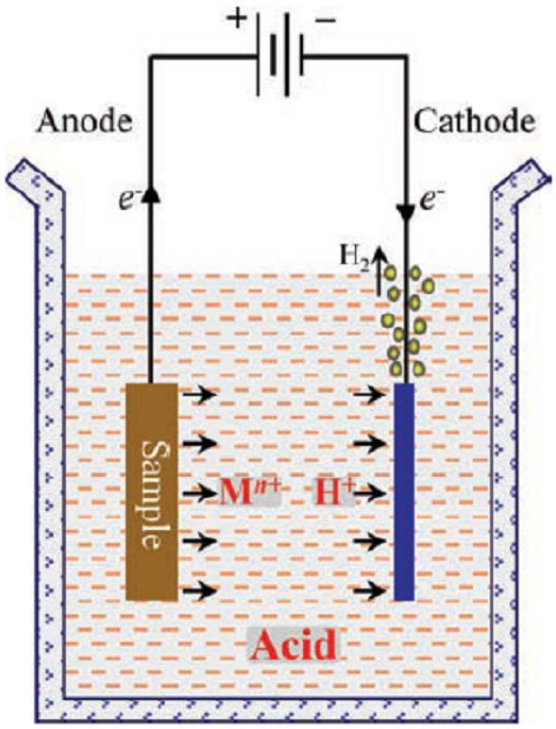

Figure 2 Schematic diagram of the anodizing cell

The AAO fabrication reaction can be described as below. At the anode, aluminum at the oxide/metal interface will be oxidized as Al^{3+} cations when electric field is conducted. (Eq. 2-2)

$$Al \rightarrow Al^{3+} + 3e^{-} \quad \text{(Eq. 2-2)}$$

The O^{2-} anions are coming from separation of water at the electrolyte/oxide interface. (Eq. 2-3)

$$\frac{3}{2}H_2O \rightarrow 3H^{+} + \frac{3}{2}O^{2-} \quad \text{(Eq. 2-3)}$$

Aluminum oxide is the product of the entire reaction. (Eq.2-4)

$$Al^{3+} + \frac{3}{2}O^{2-} \rightarrow \frac{1}{2}Al_2O_3 \quad \text{(Eq. 2-4)}$$

When the water continues decomposing, the H^+ ion will dissolve the alumina layers. (Eq. 2-5)

$$\frac{1}{2}Al_2O_3 + 3H^+ \rightarrow Al^{3+} + \frac{3}{2}H_2O \quad \text{(Eq. 2-5)}$$

However, the rate of water electrolysis is slower than the rate of aluminum oxide generation, so the aluminum oxide layer will not be dissolved completely. At the cathode, the H^+ ion reduces to form hydrogen. (Eq. 2-6)

$$H^+ + e^- \rightarrow \frac{1}{2}H_2 \quad \text{(Eq. 2-6)}$$

It is important to note that the main reason of the formation of the nanoporous structure is caused by the uneven electric field. [29] The irregularities of the aluminum surface will induce different electric field concentration. With the electric field concentrated in depressions results in a higher rate of ejection of $Al^{3+}$and a lower rate of oxide deposition. As the oxide thickens in other area, the concentrated electric field continues to prevent further crystallization in the bottom of the pores, forming the hollow structure that contributes to the nanaporous characteristics of AAO. The size and distribution of the initiating nanopores are adjusted until the reaction is stable, as shown in Fig. 3.

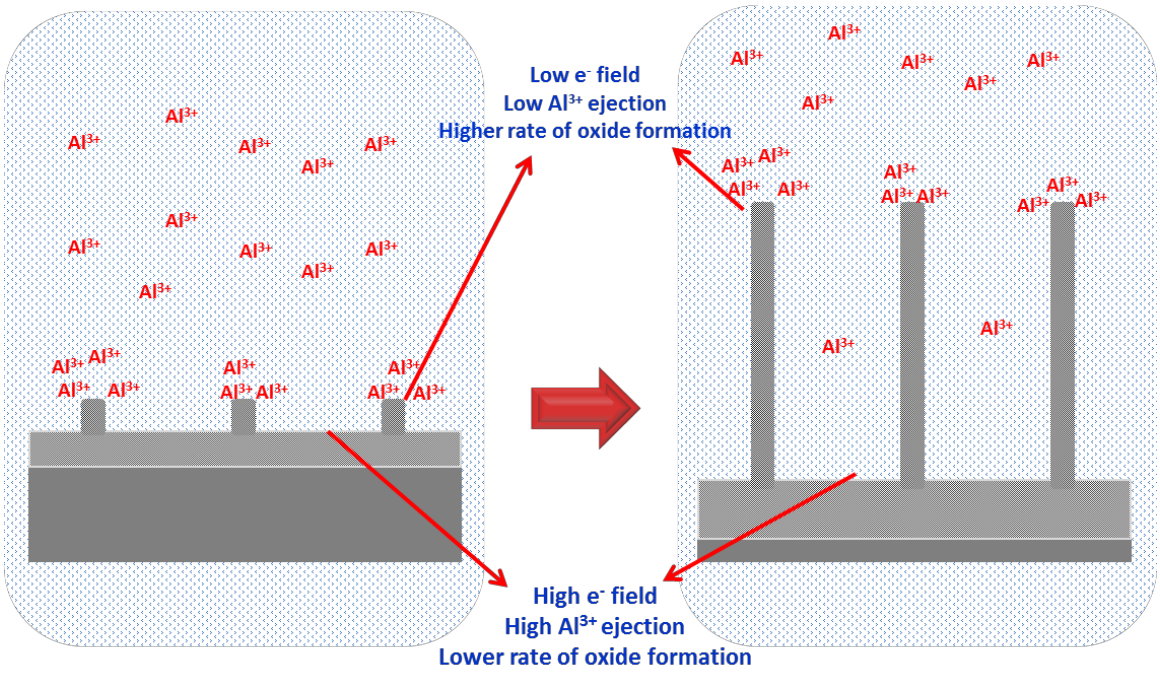

Figure 3 The schematic of electric field and ion concentration on aluminum surface during anodization

Anodic aluminum oxide (AAO) nanotubes can be formed in certain anodizing conditions. AAO nanopores are formed randomly on the aluminum surface, and nanopores self-assembly to a hexagonal structure. Self-assembly is a spontaneous organization of materials through noncovalent interactions without external interference. This phenomenon is evident in the highly ordered oxide nanotubes with high aspect ratios and the honeycomb arrays. It is possible to alter the tube lengths, pore sizes and densities by changing certain variables, such as acid electrolytes, voltages, temperatures and anodizing time. [30] However, extra sub-holes can still be found on the nanopores array. Fig. 4 demonstrates a mechanism of self-repaired process to remove the extra sub-holes. Under heat, aluminum and oxygen in ambient are able to diffuse easily into the AAO channel to react with the aluminum oxide,

and in doing so speed up the AAO self-diffusion process the lead to the reduction of the sub-holes. [31]

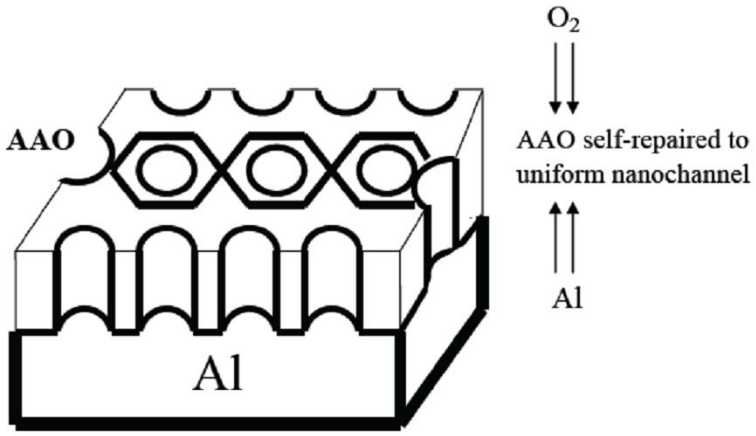

Figure 4 The schematic diagram of AAO self-repair mechanism

A two-step anodization is required to obtain an even AAO nanopores template since electropolishing does not guarantee a defect-free surface. The morphology of pre-anodizing aluminum is not a defect-free flat surface even after electropolishing. Therefore, sizes and inter-pore distances of AAO nanopores that are formed on a pretreated aluminum are not as uniform as one would expect. In order to obtain a uniform AAO nanopores template, a two-step anodization process is conducted. Fig. 5 is a process flow of the two-step anodization. After the first anodization, AAO nanoporous layer is removed and an ordered pattern with bowl-shape indentations is left on the aluminum surface. Nanopores formation follows the pattern during the secondary anodization. As a result, a much more uniform AAO nanoporous structure can be achieved.

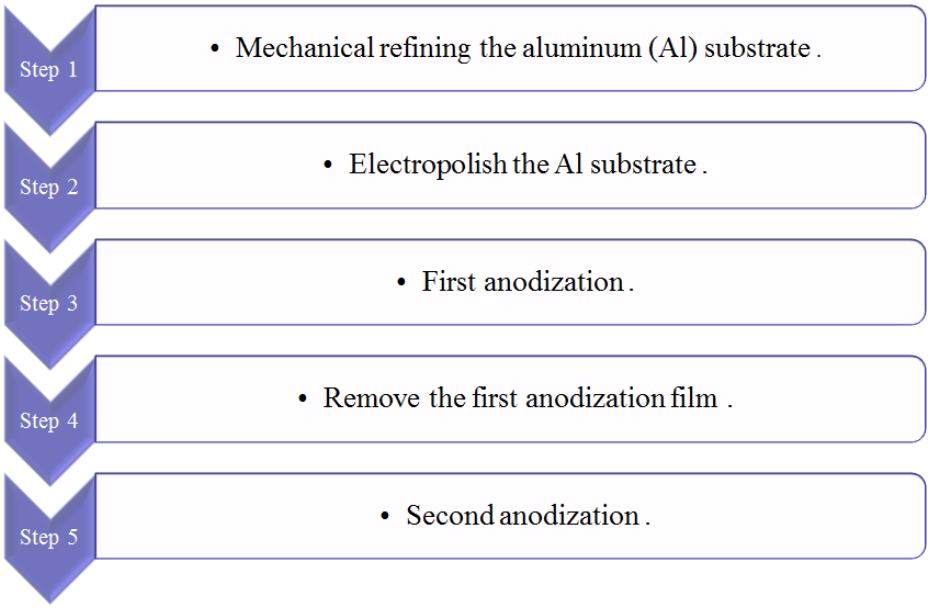

Figure 5 The flow chart of two-step anodization process

Highly-ordered AAO nanoporous structures have been used for various fields, including sensors, separation membranes, templates, and there are also breakthroughs in the fabrication of AAO. There are two main processes to fabricate AAO, one is mild anodization (MA) and the other is hard anodization (HA). Mild anodization is the traditional process that produced AAO with low current density. Under low current density, the slower process of MS allow for more time for the nanopores to form a highly-ordered structure. However, the time consuming process of MA limits the use in industrial manufacturing. Generally, HA is conducted under low temperature and high current density in order to increase the growth rate. [32] As a result, nanopores from HA are less ordered and easier to crack. Therefore, combining MA and HA has been reported to keep advantages of both anodization processes. [33] Pulse anodization process was demonstrated to fabricate a 3-D nanostructure by alternating MA and HA. [34]

Although AAO nanoporous template is a self-ordering structure, pretreatment shows a promising potential on controlling the AAO nanoporous structure. According to the concept of two-step anodization, many groups focus on the pretreatment of aluminum surface and attempt to control nanopores locations. Lee's group used the traditional photolithography fabrication to replicate a nickel imprint stamp with defectless hexagonal pattern in order to produce an ideal AAO nanoporous structure. [35] Focus ion-beam lithography [36], scanning probe microscopic lithography [37], optical diffraction grating [38], and microbeads [39] have been investigated as pretreatments for aluminum. However, these fabrication processes are slow and expensive. Comparing to the alternatives, nanoimprint method seems to be a promising technique to pre-pattern with low cost and high yield advantages. [40] Square array AAO nanopores were fabricated on Si assisted by nanoimprint. [41] Using nanoimprint pre-pattern can change the nanopore distance from the lattice constant. [42] Furthermore, AAO was not only fabricated long-range location controllable, but also created different sizes of nanopores on the same aluminum substrate with nanoimprint guiding anodization. [43]

Other than aluminum, titanium is another material widely recognized by its anodic oxide structure. There are various nanostructures of anodic titanium oxide (ATO), shown in Fig. 6, that can be obtained by controlling temperature, applied potential, viscosity, electrolyte and solvents etc. [28] As a result, different nanostructures can be formed, such as a flat compact film, a random porous structure, an ordered nanoporous film and a highly ordered nanotubular oxide layer. Self-ordered anodic titanium oxide nanotubes can also be formed in fluoride containing electrolytes, we will cover more details on this topic in Section 5.

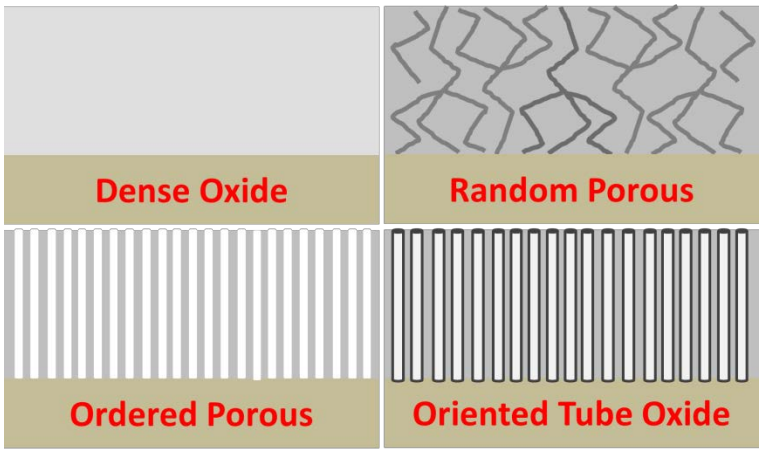

Figure 6 The schematic diagram of the titanium anodic oxides

2.2.2 AAO for Biosensing and Drug Delivery Applications

The ordered nanoporous structures are often used as templates for fabricating other nanoscale materials with specific functions. Processes have been developed to generate nanoporous structures, such as fibrous meshes [44], self-ordered block copolymers [45], silica [46], or metal oxides [28]. This dissertation will focus mainly on Anodic aluminum oxide (AAO), its nanopores have been found many applications on biotechnology due to its uniformity, high aspect ratio, highly ordered array, wide range of pore size and tube length and controllable porosity. AAO can also be fabricated on various substrates, such as Si, SiO_2 and Ti. [47, 48] More importantly, aluminum oxide is non-toxic, biocompatible and insoluble in aqueous solution, and it is also demonstrates remarkable chemical, physical and thermal stabilities. Therefore, AAO has recently been noticed and explored for many biotechnology applications that are listed below.

First of all, AAO has been demonstrated that it can be used for bio-sensing applications. Biosensors are the devices, which can produce optical, electrical or thermal

output signals for further analysis. The biosensors can be defined by sensing aspect, such as DNA, proteins, glucose, microorganisms and even tissues. AAO nanoporous structure provides a highly ordered array and controllable pore sizes from 10 nm to 500 nm for developing novel biosensors. For instance, AAO can be used for counting and identification. [49] It was designed for use as an identifier to capture targeted particles (as shown in Fig. 7a) and its sensitivity is considered to be ten times more than polycarbonate membranes. [50] Combining MEMS and anodization processes can produce a high-throughput micro-Petri dish for sensing microorganisms. [51] In addition, connecting other molecules to the inert AAO surface has enormous potential to utilize the high surface area of AAO. Fig. 7b shows a schematic diagram of attaching sensing materials within AAO nanotubes. A DNA hybridization sensor was investigated by ionic conductance through AAO nanoporous electrode to immobilize ss-DNA for detecting the target DNA. [52] Surface modification is able to change the basic properties of aluminum oxide, such as wetting ability, reflectivity, surface affinity, and selectivity. AAO can also be adjusted to become a hydrophobic material. [53] Polymer absorption or monolayer formation are usually applied for modifying the properties of AAO, for instance, coating polymer on AAO will allow the material to be able to bind with DNA structure. [54] DNA hybridization was successfully detected by using a capacitance sensor array with AAO template. [55] Au nanowires in the nanopores was coated as bottom electrode, and Au film on the surface of AAO served as top electrode. Therefore, the AAO-based sensor is highly sensitive for DNA detection since its large sensing area. A gold-deposited AAO layer chip has also been developed as an optical biosensor with localized surface plasmon resonance coupled for DNA detection. [56] In addition, biosensors can increase sensitivities when improved imagine technology assisted by AAO can lead to

higher resolution. Raman enhancement can be achieved by changing the properties of AAO surface. [57] AAO has low background signal with fluorescence measurements, thus helpful to improve the imaging technology for biosensors. [58] An AAO film platform was developed for Surface-Enhanced Raman Scattering (SERS) to examine protein and bacterial cells. [59]

Other than directly using AAO, various processes can produce nanostructures assisted by AAO template for building biosensors, such as nanowires, nanorods, nanotubes and even nanoparticles. For instance, polymer nanowires have been synthesized by extrusion through AAO template for cell research, such as tissue engineering or cell regeneration. [60] Fig. 7c presents that nanowires array can be isolated by dissolving AAO with NaOH solution. [61] Individual SiO_2 nanotube can be fabricated as a nano sensing tube assisted by AAO template and RIE process. [62] Nanoparticle sizes can be controlled by pore sizes of AAO with photo-polymerizing when monomer passing thru AAO. [63] Similarly, quantum dots, which can be grown within the AAO nanopores, increased the sensitivity of DNA detection. [64] More importantly, AAO-based glucose biosensors can offer faster and higher response than other nano biosensors. A glucose oxidase (GOx)/polymer nanofiber array biosensor based on AAO template was introduced [65], and they successfully improved the sensitivity to glucose. Fig. 7d is a schematic diagram of filling various sensing materials into AAO nanopores with a conducting layer for transmitting signal. Additionally, AAO-based nanostructural SnO_2 can be covalently attached with GOx as a biosensor. An improved sensitivity and a linear response can be observed with glucose concentration changes from the SnO_2/AAO biosensor. [66]

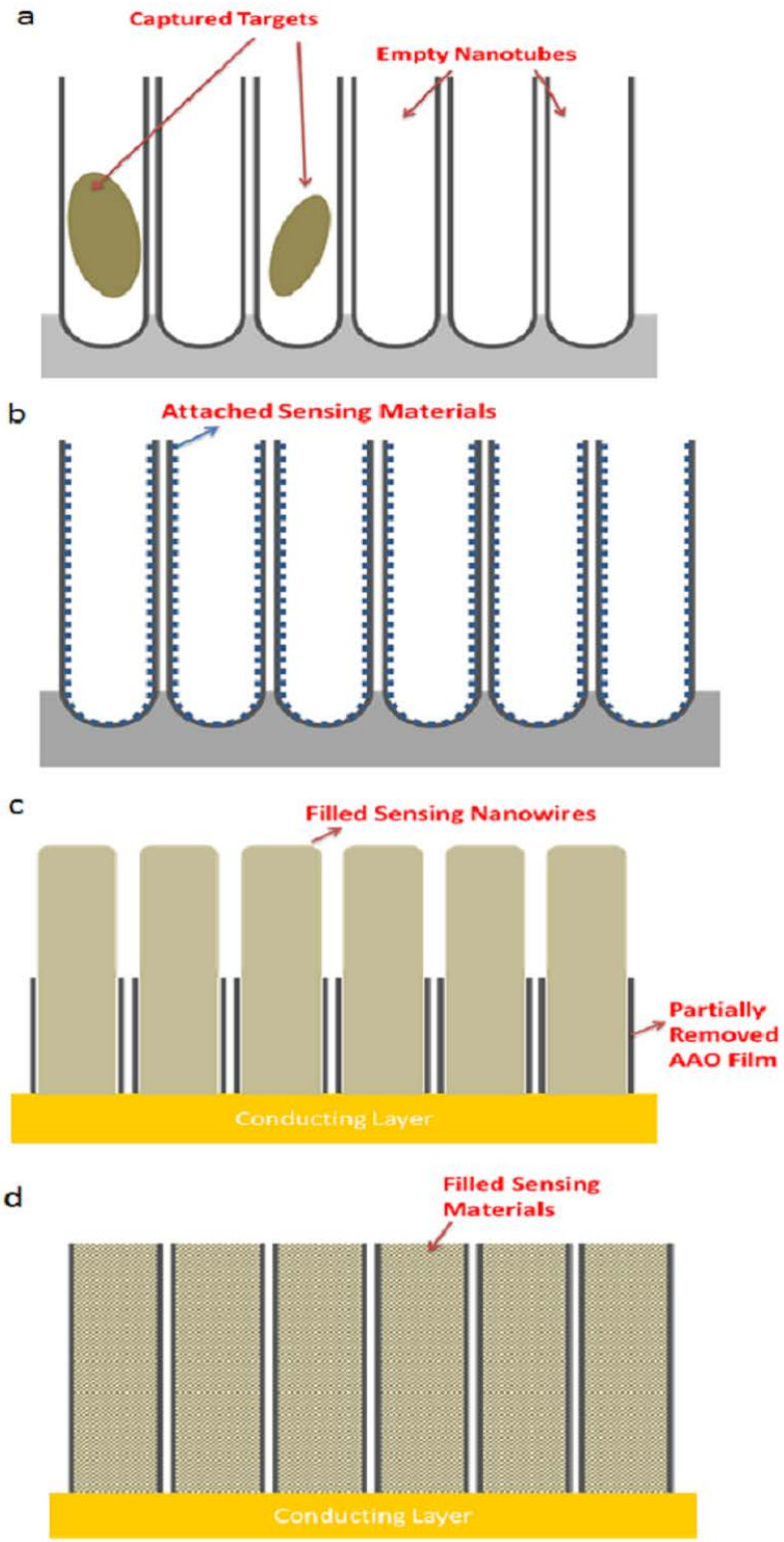

Figure 7 Schematic diagrams of types of sensing mechanism

Nanostructures have been widely investigated as devices for drug delivery applications. The purpose of controlled drug delivery is to manage the necessary amount of drug to specific sites in the human body safely and effectively. Traditionally, drug delivery devices fabricated by top-down approaches provide better controllability of the pores position and uniformity, but the fabrication based on photolithography is slow and costly. [67] On the other hand, bottom-up fabrications utilize self-assembly materials, such as AAO and block copolymer. AAO template as a membrane is a promising candidate for drug delivery, separation and purification. [68, 69] Recently, AAO nanopores have been widely investigated to satisfy the strong demand for controlling accurate drug delivery to cells, tissue and organs. Moreover, AAO nanopores can be directly grown on the Al coated surface of currently available implant devices. Generally, sustained release and on-demand release are two kinetics of drug delivery. For sustained release, the drug concentration is based on various diffusion mechanisms which can be controlled based on the size ratio of the carrier to the drug. The release profile demonstrated that molecular transport is possibly controlled by membrane pore size, and the smaller the particle size is the faster the release rate for AAO membrane. [70] Ryu et al. presented that through increasing the pore diameters can increases the amount of drug release, but increasing depth will decrease the amount of drug released. Thus, designing the pore diameter and depth of AAO film can fit various desired release rates. [71] Furthermore, a nanoporous alumina capsule was presented by Grimes's group, and they completed a tubular AAO capsule and studied the molecular releasing mechanism. [72] AAO capsule (as shown in Fig. 8a) has better biocompatibility, chemical and mechanical stability, and more uniform pore size distribution than polymeric membrane capsule. The tubular AAO

capsule was modified with poly(ethylene glycol) to reduce protein absorption and improve biocompatibility of the AAO membrane. [73]

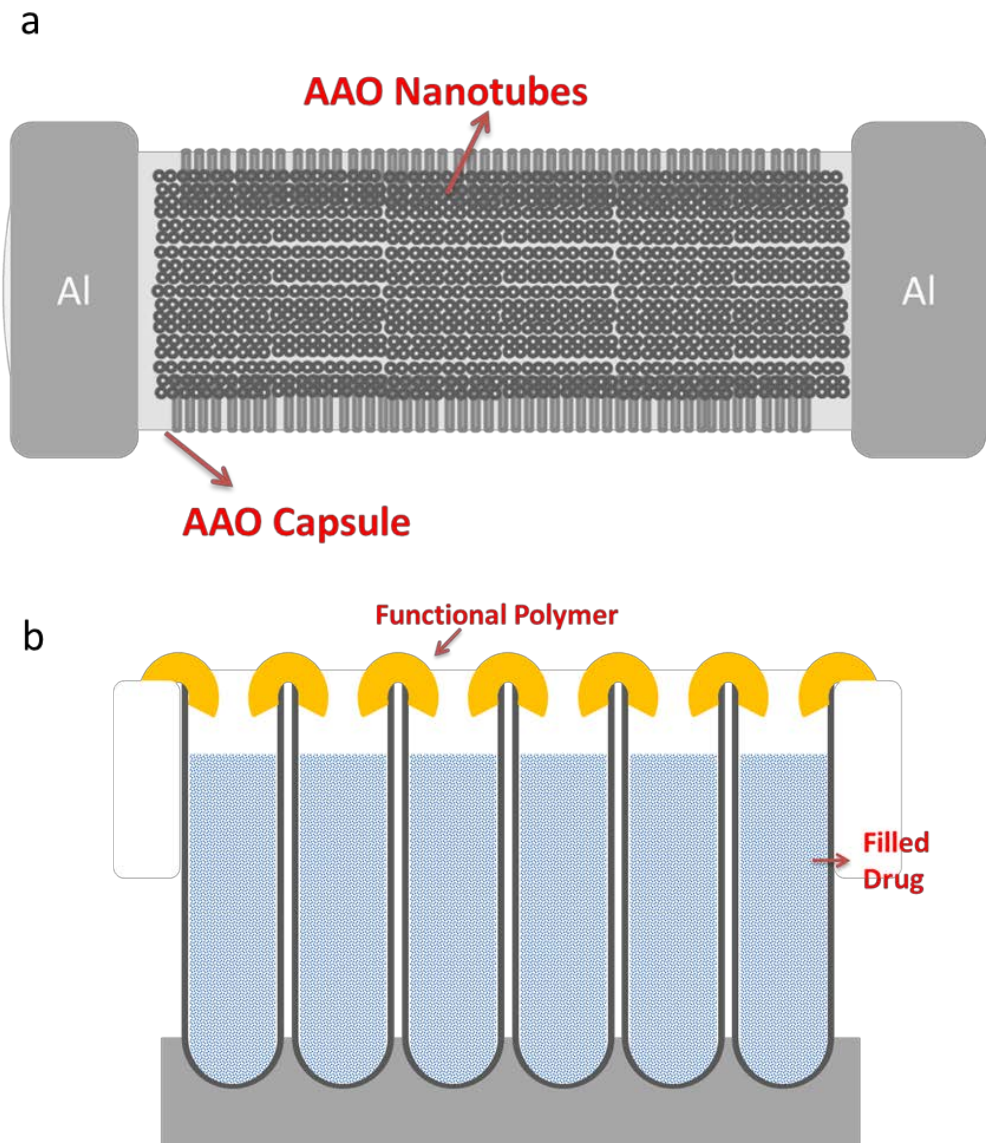

Figure 8 Schematic diagrams of AAO for drug deliver

The bottom-up fabrication can be widely used in various applications because the advantage of its flexibility for different mechanisms. [74, 75] One of the biomedical

applications utilizes the residual phosphate ions trapped within the nanopore walls when phosphoric acid is anodizing electrolyte. These trapped phosphate ions can be delivered into human bones to help in mineralization process and aid in the integration of implant with tissue for the orthopedic application. [76] Moreover, Fig. 8b presents a structure of controlling drug releasing rate by adjusting polymer thickness. For instance, Simovic et al. [77] reported AAO template was used as a drug carrier and they controlled releasing rate by coating polymer on top of the nanopores. The nanopores are easily mass produced within short processing time. Mesoporous silica with nanopores was fabricated with AAO template and performed controllable drug releasing. [78, 79] On the other hand, the on-demand releasing mechanism uses smart membranes to control the delivery by surrounding environment, such as pH value, temperature, magnetic and electric field. [80-82] An electrically actuated AAO membrane was designed for pulsatile drug delivery by coating electrically responding polymer. [83]

2.2.3 Capacitors for Energy Storage Applications

Energy storage is required in many areas, such as portable electronics, detectors, sensors, and electrical or hybrid vehicles. Energy density (Wh kg^{-1}) and power density (W kg^{-1}) are widely used to evaluate energy storages. Energy storage with high energy density is called battery which is able to keep supplying energy for the device. Batteries have high energy density but only low power density. On the other hand, many applications demand peak power to trigger or drive the devices, and capacitor happened to meet this particular high-power requirement. However, lack of energy density has always been a major concern to the traditional capacitor. Therefore, various groups have begun to seek for new generation

capacitors with high power as well as high energy density. In this subsection, a brief introduction of capacitors will be covered.

Electrostatic capacitor, also called MIM capacitor, is made of two metal plates and an insulator (dielectric) in between. It stores energy electrostatically when applying voltage across the capacitor, and charges are accumulated in the dielectric between the two electrodes, as shown in Fig. 9a. Charge/discharge electricity and block the current flow in a DC circuit are two main applications of MIM capacitor. The charge/discharge concept can be demonstrated as when a battery is connected to the capacitor, current flow includes the electron flow. Then, the electrons are attracted to the positive terminal of the battery and so they flow towards the power source. Therefore, an electron deficiency develops at the positive side and electro surplus develops at the negative side. The electron flow continues until the potential difference between the two electrodes becomes equal to the battery voltage, and it means the capacitor is charged. When the battery is removed, the electrons flow from the negative side to positive side to discharge. Different materials are used as dielectric layer in electrostatic capacitors, such as paper, paraffin, polyethylene, water, sulfur, mica, etc. [84], they can be used to store electrical energy in the form of charge separation when the electron distribution around constituent atoms or molecules are polarized by an external electric field. Dielectric capacitors based on highly polarizable inorganic materials have been used for pulse power applications. The energy stored (W) is given by: $W=1/2CV_{bd}^2$, where V_{bd} is the breakdown voltage. C is the capacitance, which can be calculated by $C=\mathcal{E}A/d$, where A, Ɛ, and d are electrode surface area, dielectric constant and thickness, respectively. However, the breakdown voltage (V_{bd}) is propotional to the dielectric thickness. Thus, there is a trade-off happened to build a capacitor because only high capacitance or high breakdown voltage can

be achieved. Ceramic materials are generally used in this kind of capacitors because they have high value of dielectric constants. For instance, $BaTiO_3$ and $SrTiO_3$ have high dielectric constant of 1700 and 2000, respectively.[85] However, ceramic materials have low inherent breakdown voltages which cause low energy density.[86] On the other hand, polymers have relatively high breakdown strengths which are up to 300 V/μm dielectric strength.[87] Nonetheless, polymers are typically low dielectric materials for capacitor application. Therefore, the objectives of high dielectric constant and high breakdown strength are not possibly achieved, and the best solution is to compromise. Polymer composites, which are polymers with high dielectric constant ceramics fillers, have been developed as dielectric layers. [88] In the polymer composites, polymers serve as the matrix and inorganic dielectric is filled into the polymer matrix to increase dielectric constant.[89] This concept utilizes high dielectric constant from ceramic and high breakdown strength by mixing ceramic capacitor layer with polymer dielectric in order to obtain better energy storage result.[90]

Traditionally, electrostatic capacitors have low energy density issue because only limited electrode surface charge and very thin dielectric layer can be used. Nanoporous structure can provide much more surface area for storing electrical charge, so both high power and energy density can be expected. [91] Therefore, electrostatic nanocapacitors can be used for military, aerospace, or other applications that require high energy and power.

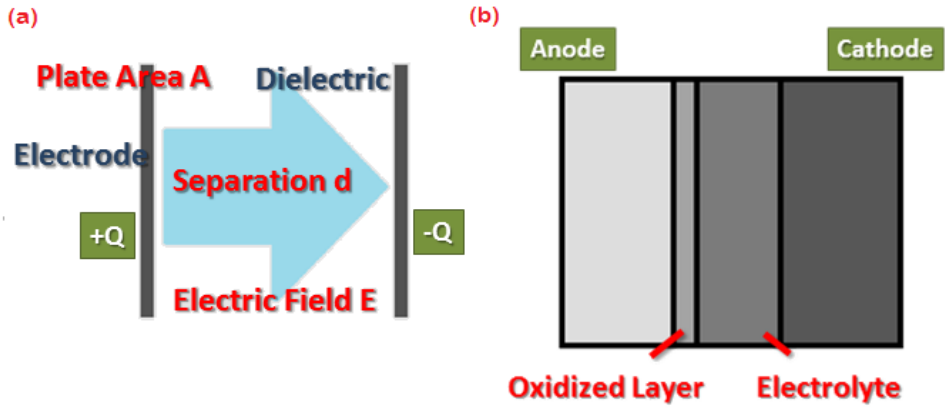

Figure 9 Schematic diagrams of (a) MIM capacitor and (b) electrolytic capacitor

Electrolytic capacitor (EC) is similar to batteries construction but the two electrodes use the same material, as shown in Fig. 9b. A typical electrolytic capacitor is an aluminum electrolytic capacitor includes an anode foil and a cathode foil separated by a dielectric layer. [92] Electrolytic capacitor uses an electrolyte as a conductor between the dielectric and electrodes. There are two types of conductors; solid electrolyte and liquid electrolyte. The performance of electrolytic capacitor can be improved by modifying the electrodes surface area or dielectric constant of electrolyte.

The other type of capacitor is the electric double layer capacitor (EDLC), where the electrical charge stored at the solid/liquid interface to construct an energy storage device. Fig. 10 shows the principle of EDLC that electric charges are accumulated on the electrode surface and opposite charged ions are arranged on the electrolyte side. The main component in the EDLC is carbon that creates both electrodes with organic and aqueous electrolytes. [93] Many types of carbon-based electrodes for EDLC have been investigated to increase the surface area, such as carbon aerogels, activated carbon and carbon nanotubes. [94] The

specific capacitance of carbon-based EDLCs is proportional to the specific surface area. However, in reality the specific capacitance also depends on other variables, such as the matching degree between the electrodes and the electrolyte. [95] For instance, an electrode was found to have higher capacitance in KOH electrolyte than in NaOH electrolyte due to a higher matching degree between the electrodes and the electrolyte in KOH. [96] However, there is one major disadvantage of carbon based EDLC that results in lower specific stored energy. Conventional EDLCs store charge in electric double layers, so they have large energy density storing on the electrode surface. Furthermore, the working environments are limited to conditions like temperature and cell voltage of EDLCs because the devices have electrolyte solution. Besides, liquid electrolyte requires high-standard safety packaging technique in order to avoid leakage of the electrolyte.

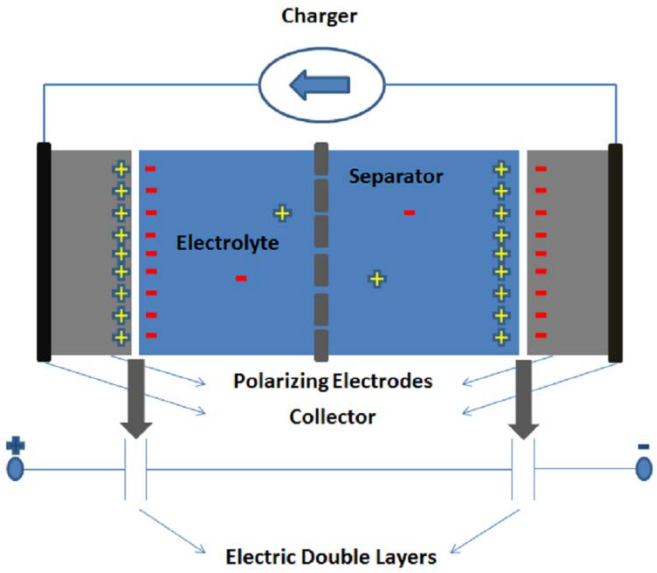

Figure 10 Schematic diagram of mechanism of EDLC

There is a rising need for capacitors that can accumulate a large quantity of energy and then deliver it rapidly. A variety of military, aerospace, and commercial applications need this type of energy storage which can provide enough power with minimal reaction time. Moreover, these applications often require higher power and energy densities as well as higher charge/discharge rates. This growing demand has led to the creation of the fourth generation capacitor, an electrochemical double layer capacitor (EDLC). The charge storage mechanism of the fourth generation EDLC includes double layer capacitance and pseudo capacitance. Pseudo capacitance involves electron transfer reactions, and when redox (the Faradaic reaction) occurs in the electrodes it made generating higher power and energy densities possible. Therefore, the EDLC is also called supercapacitor or pseudocapacitor. Transition metal oxide [97], metal oxide/ carbon composite, and conducting polymer/carbon composite [98] are electrode materials since they have high specific capacitances. However, this dissertation has focused on transition metal oxides for the properties of both multiple redox states and good electrical conductivity that can offer a number of advantages as supercapacitor electrodes. Materials such as RuO_2, NiO, $Ni(OH)_2$, MnO_2, Co_2O_3, IrO_2, FeO, TiO_2, SnO_2, V_2O_5, and MoO have been explored for these applications. [99-103] RuO_2 has been widely studied because it is conductive and has three oxidation states reachable with in 1.2 V, which means it can provides high pseudocapacitance. [104]

It is important to note that power density still has its limits in EDLCs due to the redox reactions that resulted in ions mass transportation. [105] Ions transportation occurred to neutralize the net charge during electrons transfer, when ions with opposite charge from electrolyte enter the electrode. Electrode stability is also common kinetic issues in supercapacitors when electron transfer took place in the electrode. In order to solve these

difficulties, it is often helpful to decrease the size of the electrode structure to increase path for redox reaction. [106]

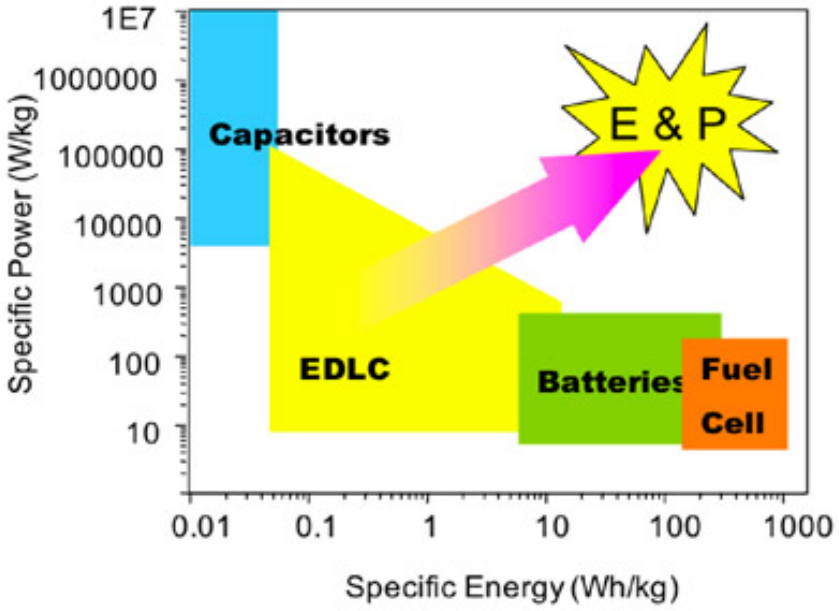

Figure 11 Ragone Plot [107] © SAE International

Overall, anodic oxide nanomaterials have the potential to improve the performance of various types of capacitors. Fig. 11 is the Ragone Plot, capacitors have high power but low energy density. Batteries, on the other hand, have large energy but without high power. Nanomaterials are potentially used to building a capacitor with high power and high energy. For MIM capacitor, nanomaterials can be used to increase metal-insulator interface, enlarge the capacitance. [91] Nanofabrication can also be used to form thinner and more uniform dielectric layer. [108] On the other hand, nanomaterials contribute to many improvements and developments to supercapacitors. Nanomaterials with large surface areas can provide larger interface for forming double layer to charge/discharge in EDLCs. [18] Nanostructures

also provide the possibility for a better mechanism for ion transportation in the redox reaction. These properties of capacitive nanomaterials can be applied to supercapacitors for a better and improved performance. [19]

3. 3-D MICRONEEDLE AND MICRONEEDLE ARRAY WITH NANOPOROUS SURFACE*

3.1 Introduction

Anodic Aluminum Oxide, also known as Al_2O_3 or AAO, is a ceramic with a high melting point and high hardness. Anodic alumina is known by various names: anodic aluminum oxide (AAO) [30, 109-112], anodic alumina nanoholds (AAN) [31], anodic alumina membrane (AAM) [113, 114], or porous anodic alumina (PAA) [115]. AAO is also an environmentally friendly and biologically compatible material used in medical and biotechnology applications [116-119]. In many different applications, a large AAO surface can be beneficial to being host for chemical absorption. The surface area of AAO ($\pi R^2 \rho D$) can be computed based on structural parameters such as thickness (D), pore size (2R), pore density (ρ), and sample size (unit area).

On the other hand, puncturing the human skin with a needle or a patch is the most common invasive medical procedure to deliver or extract fluids from the human body. During the past few years, developing painless needles or patches to replace the traditional hypodermic needles has been investigated. [120-122] The mosquito's proboscis could be a good model for painless insertion. Up to 1.5 mm penetration depth can be painless. [123] Silicon has been processed to make microneedles and microneedle arrays by conducting

* Part of this section is reprinted with permission from "Fabrication and Characterization of Chemically Sensitive Needle Tips with Aluminum Oxide Nanopores for pH Indication" by Po-Chun Chen, Sheng-Jen Hsieh, Chien-Chon Chen, and Jun Zou, 2013. *Ceramics International*, Vol. 39, 2597, Copyright [2013] ELSEVIER B. V.
Part of this section is reprinted with permission from "A Three-Dimensional Enormous Surface Area Aluminum Microneedle Array with Nanoporous Structure" by Po-Chun Chen, Sheng Jen Hsieh, Chien Chon Chen, and Jun Zou, 2013. *Journal of Nanomaterials*, Vol. 2013, 164953, Copyright [2013] Hindawi Publishing Co.

micromachining or photolithography technology. This microneedle array, with a needle length of 0.15 mm, diameter of 80 um at the base and a tip radius of 1 um, can be a painless device for injecting or extracting.[124] However, crystal silicon anisotropy limits the sharpness of the microneedle, and micromachining of silicon is costly and complex. Since the micromachining technique is able to construct a high density micropillar array on aluminum, we propose to use aluminum as an alternative material for fabricating microneedles or arrays of microneedles.

Bromphenol blue and universal indicators are two organic dyes commonly used for pH indication or the chemical stoplight demonstration. Bromphenol blue and universal indicator can dissolve in ethanol and slightly dissolve in water. The bromphenol blue indicator changes from yellow (pH 2) to violet (pH 7), but it decomposes in a strong basic solution and becomes transparent. Universal indicator is an ethanol solution containing 0.05 wt.% of each of the following: methyl red, methyl yellow, thymol blue, and bromthymol blue. The working indicated range of universal indicator is from pH 4 to 10, but it decomposes in strong acid and basic solutions. Universal indicator changes from red (pH 2) to green (pH 7), and to purple (pH 11) when the pH value goes from acid to basic. [125]

In this section, we grew AAO film on Al rods and needles and utilized the large surface area of AAO film to absorb pH indicators. Al needles with indicator-absorbed AAO film was sensitive to variations of pH-value and can be used as precise measurement tips in bio-technology, physical, or chemical applications. On the other hand, we also combine electrochemical and mechanical micromachining techniques to produce AAO microneedle array. Al is a soft material. Precision diamond saw is used for the micromachining process and able to cut Al without consuming the diamond blade. Besides, the entire machining

process is combined micromachining and electrochemical sharpening which can also modify the surface roughness when the diamond blade starts degrading. Thus, electrochemical sharpening can be conducted to form microneedle array, and help to extend the lifetime of diamond saw as well. The microneedle array provides a 3-D structure that possesses several hundred times more surface area than a traditional nanotube template. Moreover, we also introduce nanoindenter to make pyramid indents on Al surface in order to produce a female microneedle array mold. Therefore, the microneedle array can potentially be used in many kinds of applications. This 3-D microneedle array device can not only be used for painless injection or extraction, but also for storage, highly sensitive detection, drug delivery, and microelectrodes [126, 127].

3.2 Single AAO Microneedle

3.2.1 Experimental Work

In order to fabricate 3-D AAO/Al structures, we first used 6061 Al rods (8 mm) for anodizing in a 3 wt. % oxalic acid ($C_2H_2O_4$) electrolyte at 20^{o}C for 1 hour at 40 V. The random AAO pores were further improved to ordered pores by immersing the AAO sample in 6 vol. % H_3PO_4 for 20 to 45 minutes at 20^{o}C.

Al needle tips with 1μm diameter were fabricated by electrochemical micromachining. Al wire (1 mm diameter, 99.99% purity) was sharpened at 30 V in a sharpening electolyte of 15 vol.% perchloric acid ($HClO_4$), 70 vol.% ethanol (C_2H_5OH), and 15 vol.% butyl cellosolve ($CH_3(CH_2)_3OCH_2CH_2OH$) solution at 20 ^{o}C for 5 min. Then the Al needle surface was anodized at 40 V in 3 wt. % oxalic acid ($C_2H_2O_4$) electrolyte at 20 ^{o}C for 30 minutes.

The topographies of the AAO-coated rods and were observed using an FEI QUANTA 600 field emission scanning electron microscope. To absorb the rods and needles with pH indicators, they were immersed in bromphenol blue indicator and universal indicator for 5 minutes at room temperature. The sensitivity of the absorbed AAO was tested in HCl solutions of various concentrations, DI-water, and diluted NH_4OH solutions of various concentrations.

3.2.2 Results and Discussion

Fig. 12a is an SEM image of Al needles formed by electro-polishing. Because the current density was focused on the tip, the diameter of the tip was reduced to a submicron size during electro-polishing. Fig. 12b shows AAO formed on the needle tip by anodization in 1 vol. % H_3PO_4 solution at 80V for 30 minutes, and Fig. 12c is an enlarged image showing the nano-pore structure of that AAO. Fig. 12d is an SEM image of AAO grown on the needle tip by anodization in oxalic acid solution at 40V for 30 minutes, and Fig. 12e is an enlarged image showing the nano-pore structure of that AAO on the needle tip. The pore diameter of AAO is controllable from 10 to 500 nm by anodization in sulfuric acid, oxalic acid, and phosphoric acid electrolytes. The small pores and resultant large surface area of AAO act as a host for the second materials. Fig. 12f shows the structure of a broken needle, revealing the inner Al substrate and outer film of AAO template, which give the needle both toughness and hardness. Fig. 12g and h show side view images of AAO, revealing the barrier layer on the bottom and isotropy of the cross-growth barrier layer, which provides the saw-tooth shaped of the AAO pore wall. It is also important to note that the ceramic property of the AAO tip also makes the Al needle harder and stronger for contacting with test samples.

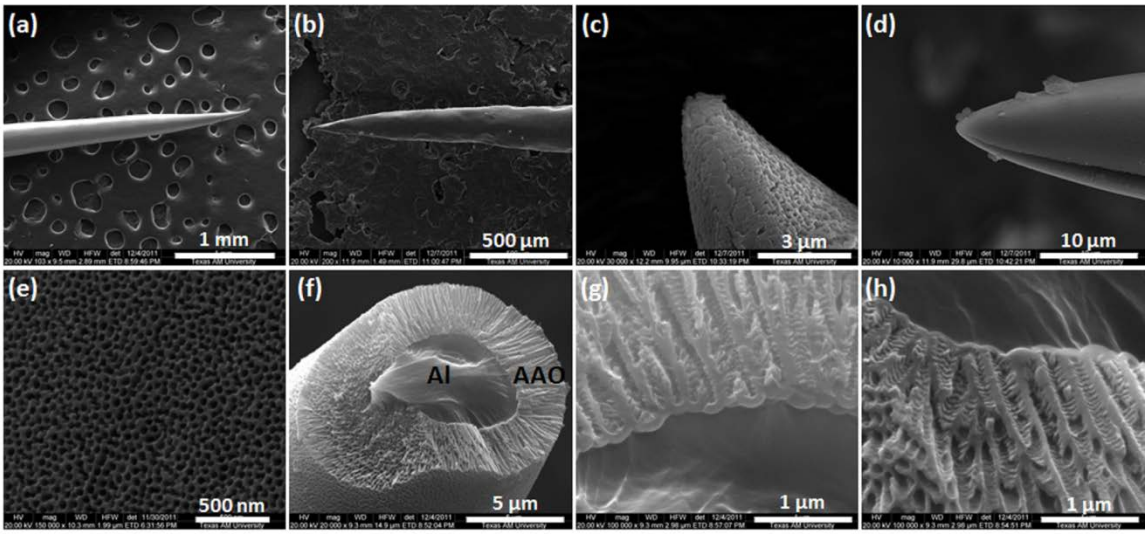

Figure 12 SEM images of aluminum microneedle

Fig. 13 shows the different etching rates on the top and sidewall of aluminum because current densities are different during the sharpening process, and this also reveals the mechanism of the electrochemical micromachining for producing microneedle.

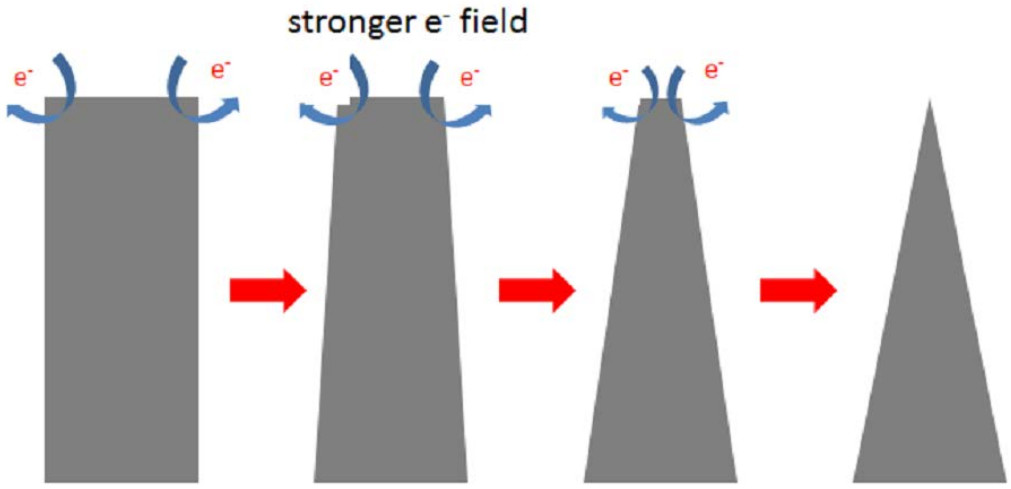

Figure 13 Schematic diagram of the growth mechanism of AAO microneedle

3.3 AAO Microneedle Array for Drug Delivery

3.3.1 Experimental Work

The aluminum micropillar array was fabricated by micromachining process using a diamond blade on an aluminum piece (99.99% purity) with 10 mm thickness. There were 20 cuts in each direction (x and y), and the distance between two pillars were 500 um and the depth was 5 mm. Fig. 14a shows the schematic diagram of the 400 microneedles on aluminum piece. The sharpening process was conducted at 15V in the same sharpening solution at 5 ^{o}C for 10 min. Lower temperature and longer sharpening time can prevent generating too much heat during the process because of the enormous reacting surface. Then the aluinum needle array was anodized at 40 V in 3 wt. % oxalic acid ($C_2H_2O_4$) electrolyte at 20 ^{o}C for 30 minutes. After anodization, a 3-D micro-needle array structure with large AAO surface area can be formed. Fig. 14b shows the schematic diagram of the aluminum needle array.

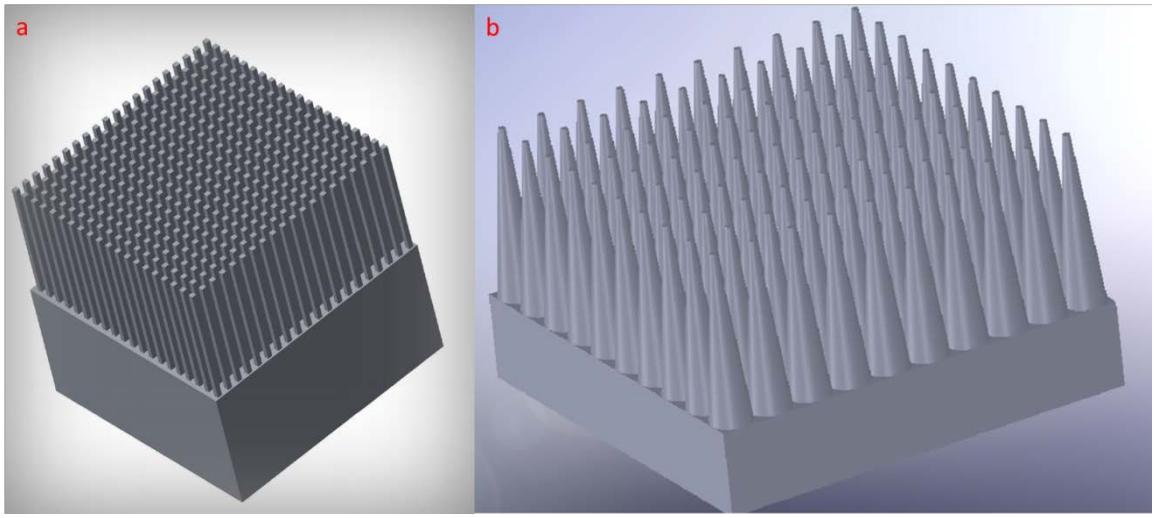

Figure 14 Schematic diagrams of Al micropillar and microneedle arrays

On the other hand, we also introduced nanoindenter to make micro-indentation array onto a pure aluminum piece (99.999 %). Hysitron Triboindenter Nanoindenter (341-F) performed the nanoindentatino process with a 1 um diameter probe. A 5 x 5 indentation array was formed on the aluminum piece. Then the indented aluminum piece was anodized at 120 V using a platinum plate as the counter electrode in 1 vol. % phosphoric acid (H_3PO_4) electrolyte at 10^{o}C for 2 hours. Through this process, we expect to obtain a female mold for fabricating nanoporous microneedle array with more options of materials.

The topographies of the microneedle array and micro-indentation array were observed using an FEI QUANTA 600 field emission scanning electron microscope.

3.3.2 Results and Discussion

Fig. 15a shows the SEM image of the aluminum microneedle array on a 10 mm thickness aluminum piece, and Fig. 15b shows the SEM image of the needle tips. There were some wider tips because aluminum is soft and easy to break. Fig. 15c is the SEM image of the microneedle covered by an AAO film. The surface area of the microneedle array became much larger after anodization. Furthermore, anodizing the aluminum needles not only increases the surface area, but also enhances the mechanical strength. The ceramic property of the AAO tips makes the micro-needle array harder and stronger for contact or attachment with test samples. Fig. 15d shows the SEM image of the nanoporous structure on the microneedle array. The pore diameter is about 60 nm, and the pores density is $10^{10}/cm^2$. [28]

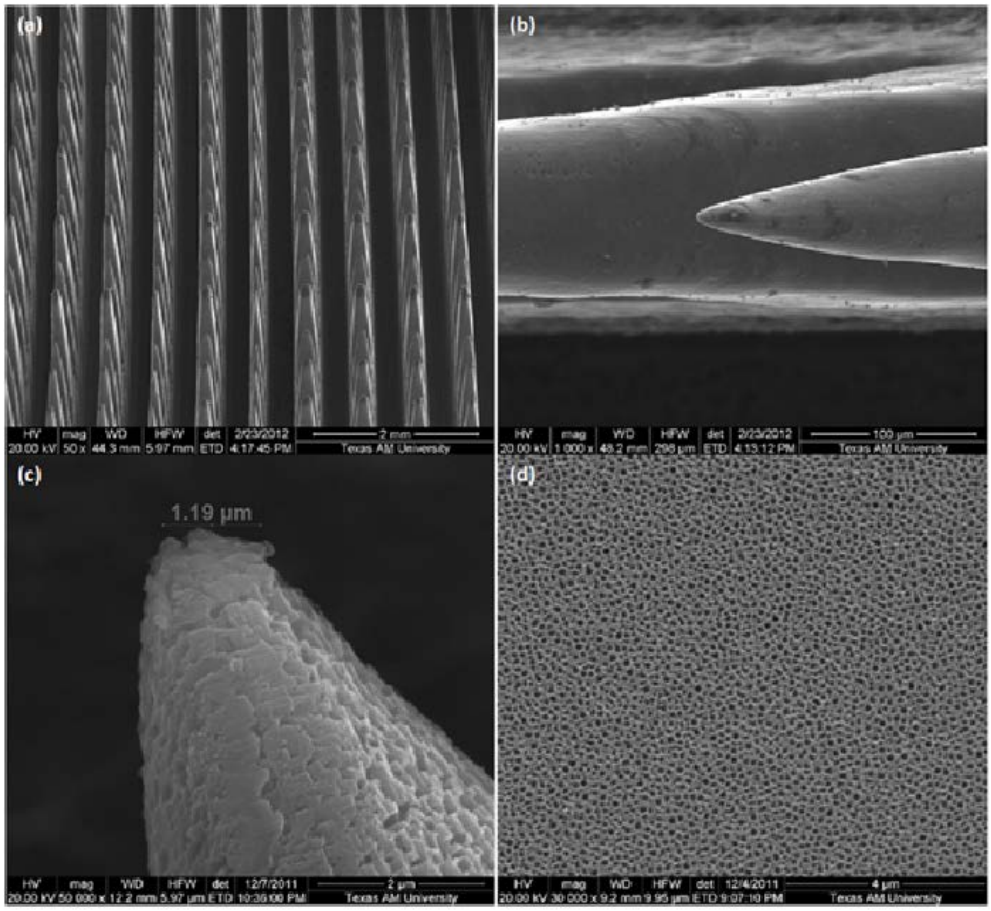

Figure 15 SEM images of aluminums microneedle array

The surface area of a single microneedle is πRL (L is the length of the microneedle, and R is the pillar radius). Comparing to a 2-D AAO structure, the surface area of having 400 microneedles increase significantly. For the microneedle with 5 mm length and 0.3 mm bottom diameter, the surface area of the microneedle array can be calculated as 10 cm^2 in a 1 cm x 1 cm sample. If we compare this AAO microneedle array with 2-D AAO plate, the surface area increased 10 times. Therefore, the aluminum microneedle array has 10 times more surface area for forming AAO than an aluminum piece.

The capacity of the painless microneedle array can be calculated from the surface area of the painless microneedle tip. According to Khumpuang's report [123], 1.5 mm depth and 100 um diameter can be painless. Thus, the aluminum pillars can be sharpened by electropolishing to obtain 5 mm length and 300 um bottom diameter microneedles as mentioned above. The upper 1.5 mm part of microneedle has 75 um diameter, so the total surface area for 400 microneedles is 1.41 cm^2. The aluminum microneedle tip can be anodized to form AAO nanoutubes with 5 um length, 60 nm diameter, and $10^{10}/cm^2$ pores density. Hence, the capacity of the microneedle array can be calculated as $2x10^{-4}$ cm^3 in a 1 cm x 1 cm sample by the Eq. 3-1. Where A is the total surface area for the 400 microneedle tips. ρ is the pore density, r is the pore size, and D is the length of AAO nanotube we fabricated.

$$Capacity = A \times \rho \times \pi \times r^2 \times D \qquad \text{(Eq. 3-1)}$$

From the calculation we made, the microneedle array not only increases surface area, but also enlarges the capacity of the device. Moreover, the other benefit is that using AAO microneedle array is more flexible for drug delivery. Because the releasing rate, time, and amount are controllable by simply adjusting nanopore size and nanotube length on the needle array.[71] Therefore, the microneedle array can be used on various detecting, storing, or drug delivering applications.

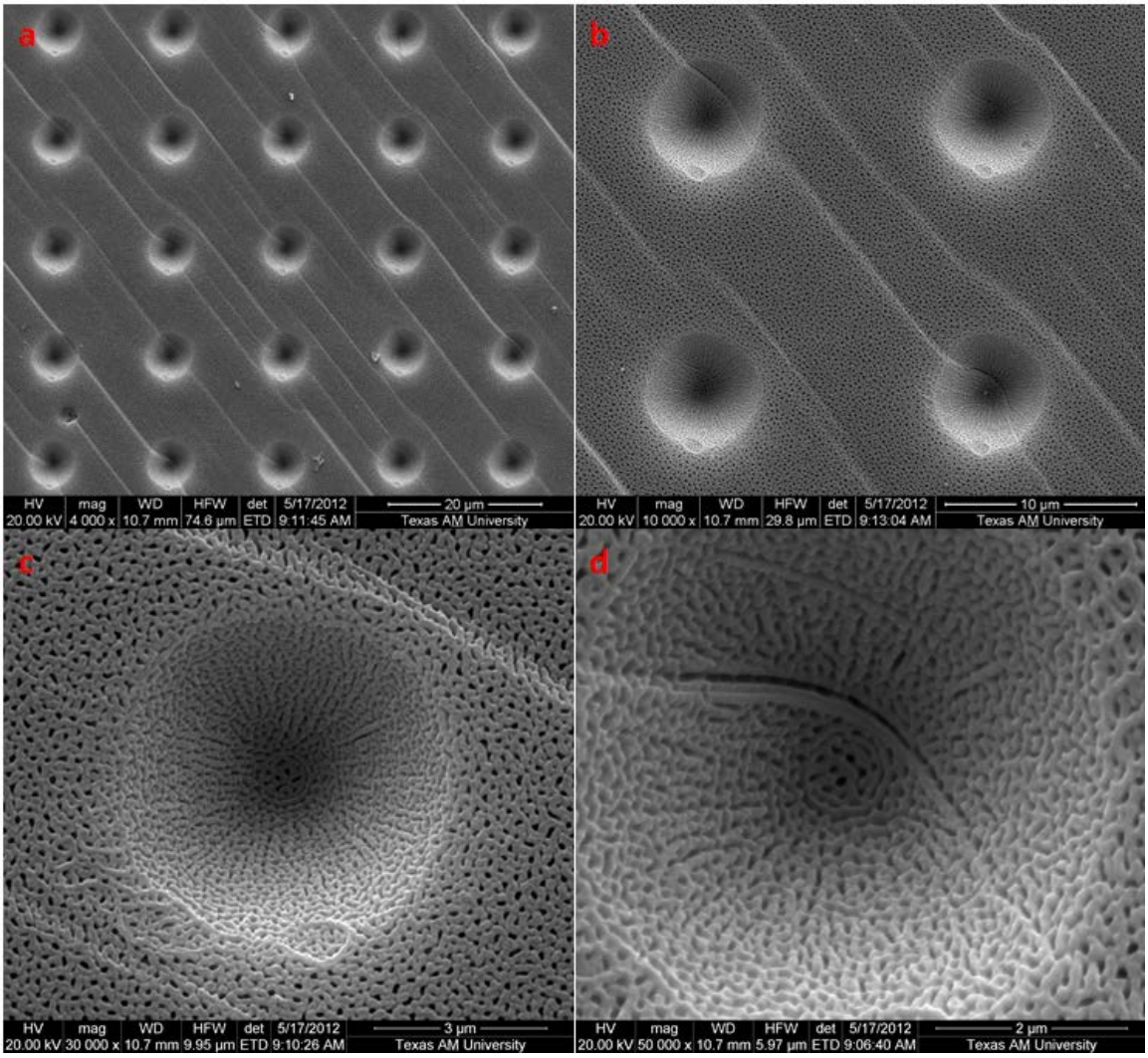

Figure 16 SEM images of the results of anodization on the indented aluminum

Similar structures can also be obtained from a female mold. For the indented aluminum piece, Fig. 16 shows SEM images of the results of anodization on the indented aluminum in various magnifications. A 5 by 5 indentations array was formed on an aluminum substrate; the tips were 1 um and very uniform. Anodizing occurs in the directions normal to the aluminum surface, so the entire surface of the indentation was nanoporous structure. In this case, filling the female mold with low melting point metals or polymers that

can be filled into it can successfully, as shown in Fig. 17, lead to a nanostructural microneedle array. More applications can be developed by these innovating fabrications.

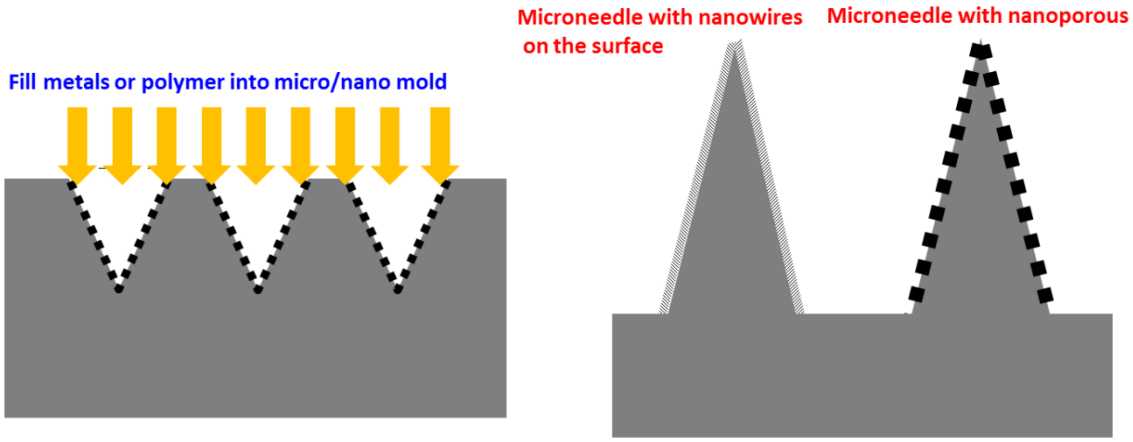

Figure 17 Schematic diagram of filling metals or polymer into micro/nano female mold

3.4 Application in pH Sensing

The macro size of 6061 Al with a surface coating of AAO and absorbed pH indicator is convenient for detection rods for acid-basic testing. Fig. 18a shows the optical image of the raw surface of 6061 Al rod, and Fig. 18b presents the bright and smooth Al surface after electro-polishing. In order to obtain a high quality AAO film on the Al surface, the Al rod must be electro-polished. Fig. 18c shows AAO film deposited on the surface by anodization, which offers a larger host surface area for the absorption of chemical agent. Fig. 18d is an image of the rod absorbed with bromphenol blue and tested in pH 7.0 of DI-water. The rod turned violet. When the rod was further tested in dilute HCl solution with pH 2.0, it turned yellow (Fig. 18e). In repeated testing of the rod in the pH 7.0 and 2.0 solutions, the color alternated between violet and yellow.

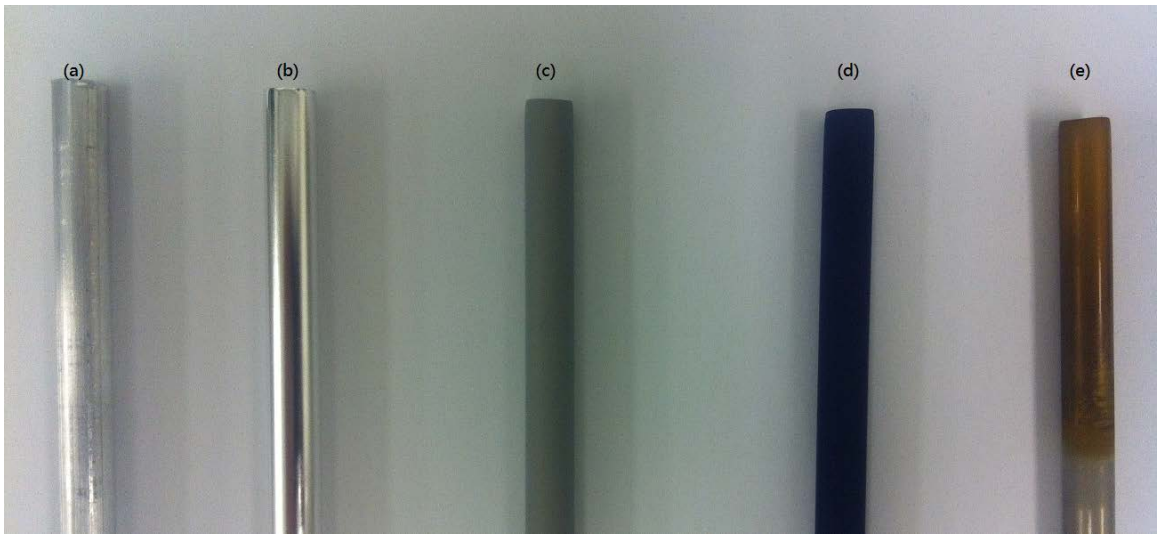

Figure 18 Images of 6061 Al rods morphologies

Fig. 19a shows an optical microscope image of the Al needle tip formed by electro-polishing. Universal indicator has a wider pH detection range than that of bromphenol blue**.** Fig. 19b shows an optical image of AAO needles absorbed with universal indicator and tested in various solutions and vapors. Needle 1, covered by AAO film absorbed with universal indicator, was tested in an HCl solution (pH 2) and turned red. Needle 2 was tested in a pH 4.0 dilute HCl solution, and the color changed to orange. Needle 3 was immersed in pH 9.0 NH_4OH solution, and it turned green. Needle 4 turned gold after immersion in DI water, and Needle 5 turned blue when tested in 0.1 M NH_4OH solution. Fig. 19c shows needles with AAO film absorbed with bromphenol blue after immersion in DI water (violet) and 0.1 M HCl solution (gold). Fig. 19d shows that the tips changed color immediately upon contact with different solutions. The AAO needle tip is very sensitive to testing materials because the nanoporous structure of the tip provides an extremely large surface area for indicator absorption.

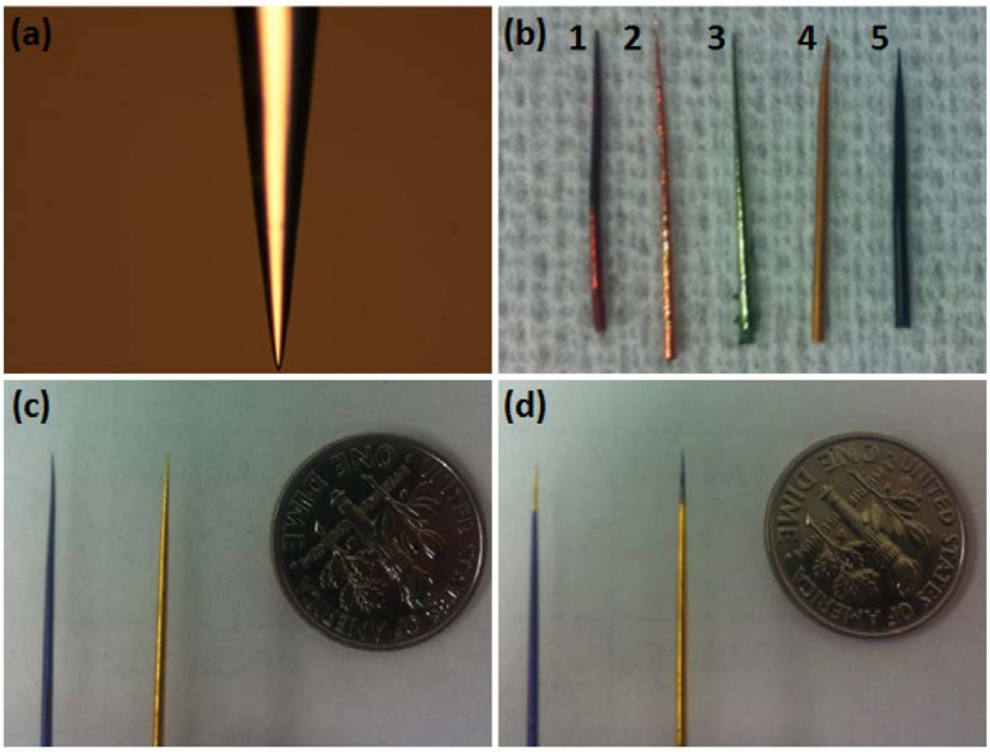

Figure 19 Images of microneedles covered by AAO

3.5 Conclusion

In summary, we presented convenient and low-cost processes to fabricate nanostructures on Al rods, microneedles, and microneedle arrays by electrochemical micromachining and anodization processes.

The rod and microneedle surfaces covered with nanoporous oxide layer can be used as sensors or detectors. With the large surface area, the material can quickly absorb indicators, making it a great candidate for chemical or biological detection. In this section, we demonstrated this idea by using pH indicator to detect changes in air or solutions. Another interesting application would be to integrate with thermal and hydrophilic-hydrophobic sensitive films, e.g., poly (N-isopropylacrylamide, PNIPAM), in order to increase accuracy

in biotechnological detection. Our research also suggests that nanostructural microneedles can be made possible by other metals which can form oxide nanotubes, such as Ti, W, Ta and Mo. Furthermore, AAO film can also be grown on other materials by coating an Al layer and then anodizing it, this largely increase the selection of possible materials.

These 3-D structures are covered by AAO films, so they can enlarge the surface area and capacity, and enhance the mechanical properties as well. The machining process is combined micromachining and electrochemical sharpening which can also smooth the surface when the diamond blade starts degrading. Therefore, electrochemical sharpening can form microneedle array, and extend the lifetime of diamond saw as well. The aluminum microneedle array and other materials arrays made by the AAO female mold, which are potentially able to absorb with detecting indicators, can be used for chemical or biological detection. [20] It can also be applied to drug delivery or storage applications because it can approach painless injection/extraction and high capacity.

4. AAO TEMPLATE NANOENGINEERING AND FABRICATION OF HYBRID NANOSTRUCTURES

4.1 Introduction

Anodic aluminum oxide (AAO) has nanoporous structure, and this structure has advantages of high aspect ratio, highly-ordered, uniform, controllable pore sizes (from 10 nm to 500 nm), and stability in chemical and thermal surroundings. In last decade, AAO nanoporous structure with naturally self-ordered nanotubes have been investigated and demonstrated as an important assisting material. For instance, magnetic [128], electronic [129], optoelectronic [130], biological [131], and micromechanical devices [132] can be effectively improved by using AAO as a template. Furthermore, nanowires, nanotubes, nanorods, and nanodots can be formed from AAO templates. All of these possibilities make AAO templates very promising assisting materials.

Metals, ceramics, and polymers all have been investigated to fabricate nanostructures for years, and they have been filled into AAO templates in various shapes as well. For metals (including alloys), nanowires, nanorods, nanotubes, and nanodots have been produced by using AAO as templates, such as copper, nickel, Sn/Bi [133], etc. Melting injection [134], PVD [135], ALD [136], CVD [137] electroplating [61], and electroless deposition [138] are all possible fabrication processes to fill metals into AAO template to form those nanostructures mentioned above. On the other hand, AAO assisted nanostratural ceramics, such as TiO_2, ZnO and $BaTiO_3$, can be formed by PVD [139], ALD [140] and sol-gel deposition [141]. Polymers are normally melting at lower temperatures, so melting injection

is the common process for nanostructure formation with AAO template [142]. However, some viscous polymers are difficult to fill into AAO by injecting; sol-gel deposition is often used as an alternative method for filling under this circumstances [143].

There are, however, limits to the application of AAO. The long-range self-assembly nanostructure can only been observed under certain anodization conditions with specific dilute acidic solutions (sulfuric acid, oxalic acid, and phosphoric acid). AAO nanoporous is a self-ordering structure generating random location of nanopore in a hexagonal close-packed arrangement. Secondary anodization is a method to fabricate nearly defect free AAO template, which creates a pattern through removing the first anodized layer. The pattern later helps form the AAO structure by following those nanoindents in bowl shape. [144] Under the influence of this concept, many researches focus on the pretreated aluminum and attempt to control the location of nanopore. Lee's group used the traditional photolithography fabrication to replicate a nickel imprint stamp with defectless hexagonal pattern in order to produce an ideal AAO nanoporous structure. [35] Focus ion-beam lithography [36], scanning probe microscopic lithography [37], optical diffraction grating [38], and microbeads [39] have all been investigated as pretreatments for aluminum. However, these fabrication processes are slow and expensive. In light of all alternatives, nanoimprint seems to be a promising technique to pre-pattern with low cost and high yield results. [40] Chung's group fabricated square array AAO nanopores on Si assisted by nanoimprint. [41] Choi et al. reported that using nanoimprint pre-pattern can change the nanopore distance from the lattice constant. [42] Furthermore, Jin's group not only fabricated long-range location controllable AAO, but also created different sizes of nanopores on the same aluminum substrate with nanoimprint guiding the anodization. [43]

In this section, metals, ceramics, and polymers nanostructure can be produced by various processes. More importantly, we propose to combine those fabricating processes to fill multiple layers into AAO nanopores. Hence, there will be more and wider applications developed. In addition, we designed nanoimprint molds with different order, pillar size and inter-distance to investigate how to control location of forming AAO nanopores. Moreover, growing various sizes of nanopores can be done with nanoimprint assistance. Therefore, fabricating AAO with different nanopores on the same aluminum piece has also been demonstrated.

4.2 Hybrid Nanowire and Nanotube Fabrication

4.2.1 Experimental Work

Fundamental to this experiment is to obtain AAO template and to remove the aluminum substrate and barrier layer. AAO templates are either fabricated from second anodization with pure aluminum pieces (99.999 %), or purchased from Whatman Co. Certain characteristics of purchased commercial AAO templates are predetermined because the pore sizes and thickness are fixed. On the other hand, the options of one side or both sides open depends on the further fabrication process when using lab-made AAO to produce nanostructural materials. Common procedure can also include removing the aluminum substrate and barrier layer, which can be achieved by immersing AAO templates in a saturated $CuCl_2$ aqueous solution for 30 minutes to remove aluminum substrate, and then etching in a 5 vol. % H_3PO_4 solution for 5.5 hours at room temperature to dissolve barrier layer.

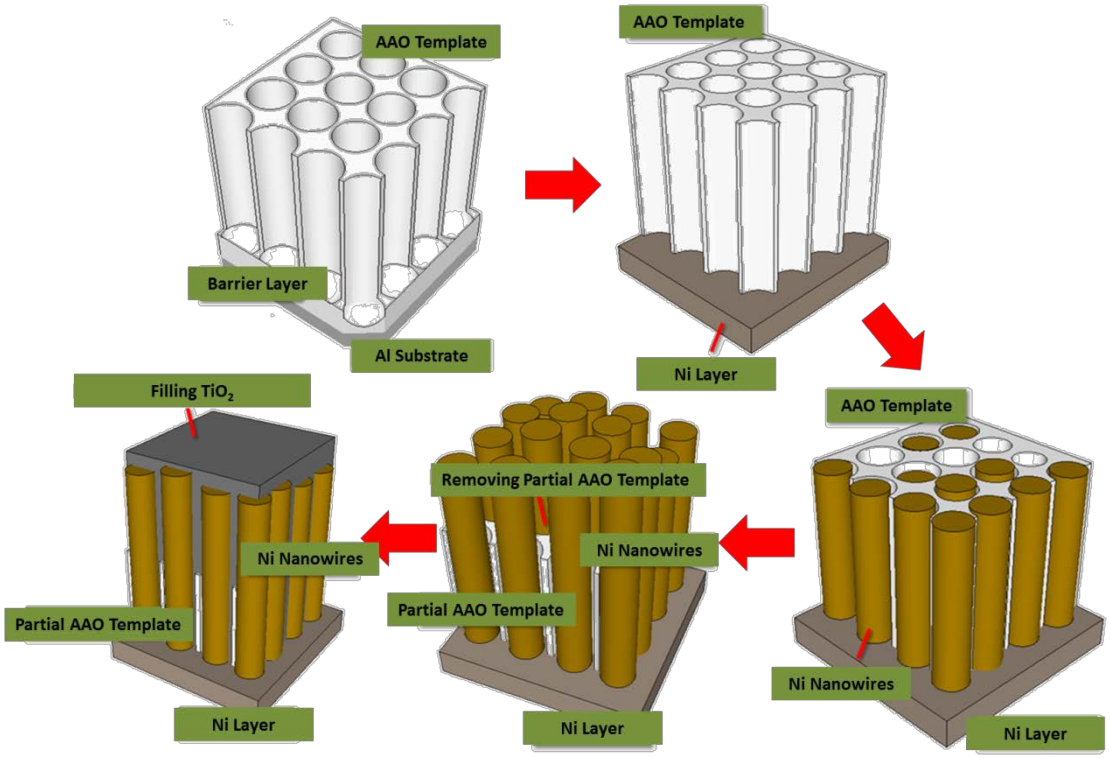

Figure 20 Schematic diagram of hybrid nanostructure fabrication

First, Ni nanowires and TiO_2 nanotubes are deposited onto the AAO template. Ni nanowires can be fabricated with AAO template by electroplating. In order to perform this process, aluminum substrate and barrier layer of AAO have to be removed. Then, deposit a 200 nm metallic layer (Pt, Ni, Cu, etc.) as the working electrode during electroplating process. AAO with nickel electrode was immersed into a solution of $NiSO_4 \cdot 6H_2O$ (120 g/L), $NiCl_2$ (60 g/L), H_3BO_3 (30 g/L), and PEG2000 (2 g/L). The pH-value is controlled at 4 at room temperature. The electroplating is conducted at a constant current density of 50 mA for 30 and 60 minutes. After electroplating, AAO template can be partially remove by a 1 M NaOH solution. The TiO_2 nanotubes can then be filled into nickel nanowires array by sol-gel deposition. The nickel nanowires array was immersed in a 0.004 M TiF_4 (pH = 1.0−1.3,

adjusted by HCl) solution for 10 minutes. At this point, the structure can be taken out and add NH_4OH to adjust the pH-value of TiF_4 solution to 3.0－3.3. Then immere nickel nanowires array againg into the TiF_4 solution (pH = 3.0−3.3, adjusted by NH_4OH) for 40 minutes. The titanium dioxide was deposited inside the vacant space. The schematic diagram of the entire processes is shown in Fig. 20.

Another structure that can be fabricated using the AAO template is a core-shell structure of Ni and $BaTiO_3$ nanotubes. First, Ni nanotubes can be formed by electroless deposition with AAO template assisted, and AAO can be either one-side or both sides opened. Sensitization and activation were pretreatments for nickel electroless deposition process. Sensitization was conducted in a solution composed of 0.3 wt. % $SnCl_2$ and 2.5 vol. % HCl for 3 minutes. The activation was carried out in a solution of 0.1 wt. % $PdCl_2$ and 0.1 vol. % HCl for 3 minutes. After pretreatments, nickel nanotubes were filled into the AAO template by electroless plating for 30 minutes at 70^{o}C. The electroless plating solution is composed of $NiSO_4$ (20 g/L), NaH_2PO_2 (20 g/L), $Pb(NO_3)_2$ (2 ppm), and sodium citrate (20 g/L). After nickel nanotubes were formed in the AAO template, sol-gel deposition of BaTiO3 was filled into nickel nanotubes/AAO structure. A solution was prepared for sol-gel deposition with 0.2M $TiCl_4$ and 0.05 M $Ba(OH)_2 \cdot 8H_2O$ in Na_4OH solvent at 100°C for 1hr. Fig. 21 is the schematic diagram of the entire fabrication process flow.

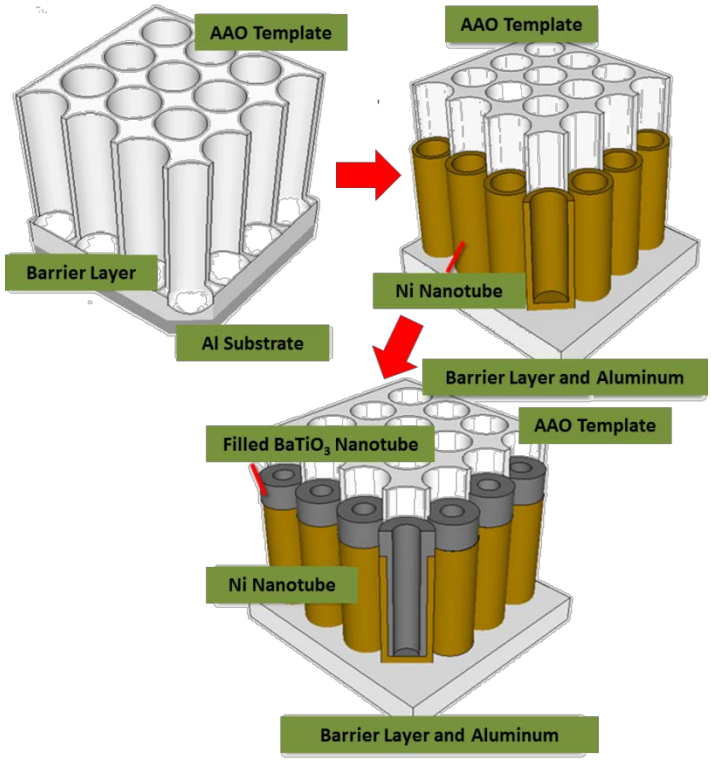

Figure 21 Schematic diagram of Ni/$BaTiO_3$ core-shell structure fabrication process

Additionally, ultra high molecular weight polyethylene (UHMWPE) nanotubes can be formed with the commercial AAO template assisted by melting injection. UHMWPE powder was first uniformly covering the AAO template, and then set up with the melting injection chamber shown in Fig. 22. After UHMWPE was molten, applying 40 psi pressure to push UHMWPE into AAO for 12 hours. Constant pressure for a long period of time is required in this process due to the viscous nature of the polymer.

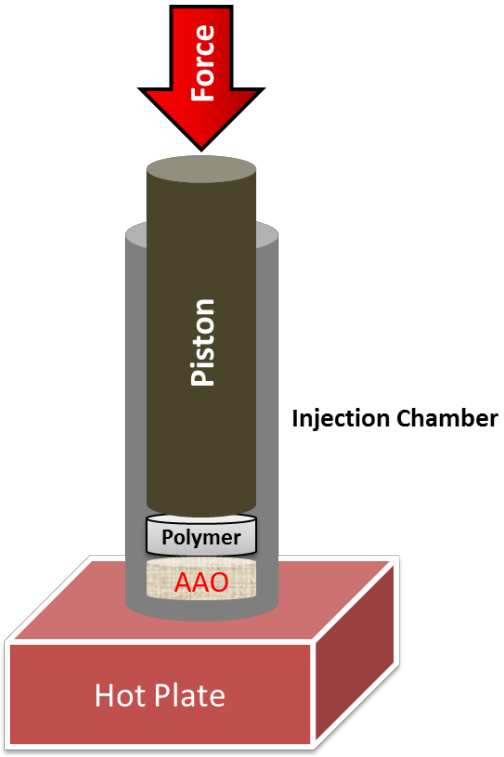

Figure 22 Schematic diagram of polymer melting injection

The microstructures of the specimens were analyzed by field emission scanning electron microscope (SEM) (FEI Qunta 600 and JEOL JSM-7500). The composition was analyzed by energy dispersive X-ray spectrum (EDS, Oxford).

4.2.2 Results and Discussion

Fig. 23 shows SEM images of Ni nanowire/ TiO_2 nanotube structure. Fig. 23a is the cross-section view of the AAO template with nickel nanowire inside after 30 min electroplating at 50 mA/cm^2, and the length of nanowires are about 19 μm. Fig. 23b is the result of the electroplating for 60 min at 50 mA/cm2, and the length of nanowires are about 34 μm. Fig. 23c and d show the results of removing the partial AAO template by 1 M NaOH for 5 min. There is about half of template remaining at the bottom and nickel nanowires are

free-standing without the AAO template. Fig. 23e and f show the cross-section views of nickel nanowires coated with sol-gel TiO_2.

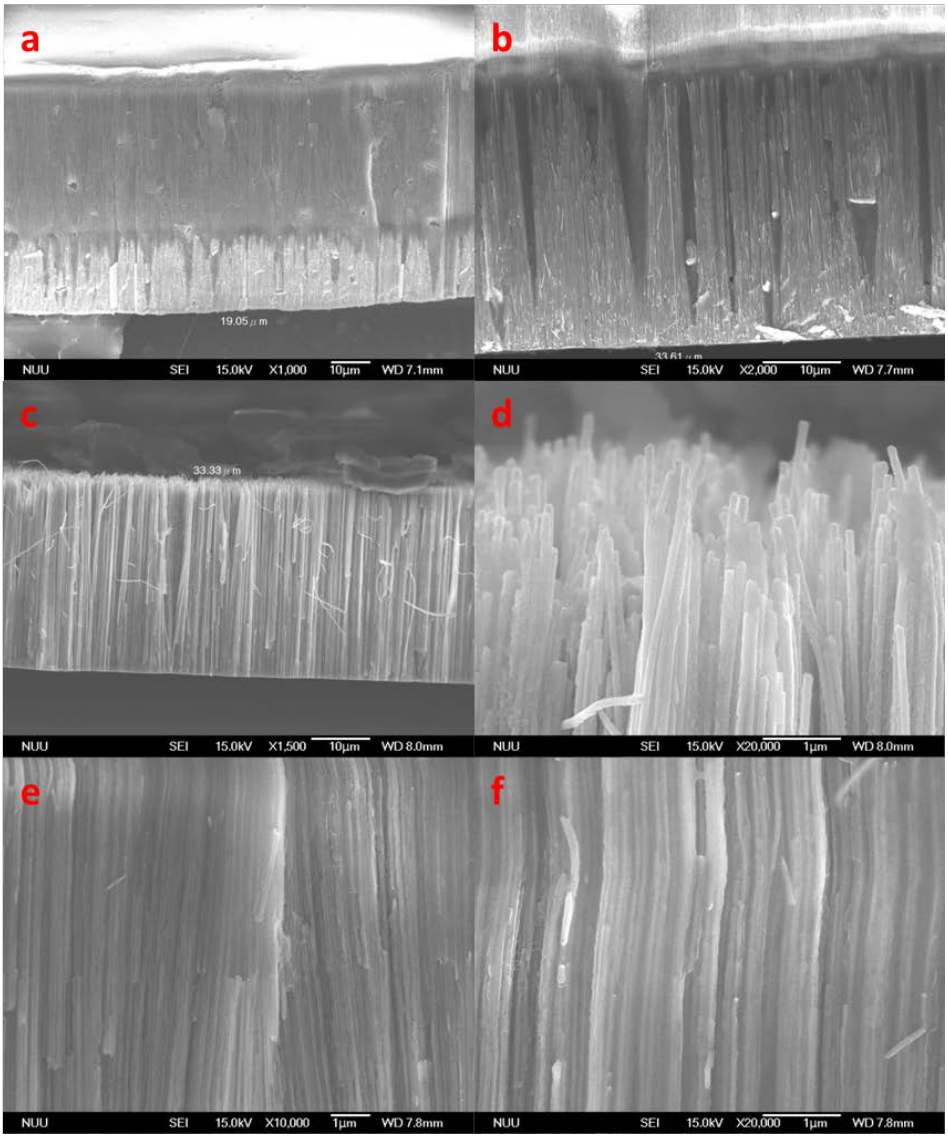

Figure 23 SEM images of Ni nanowire/ TiO_2 nanotube structure

Fig. 24 shows SEM images of Ni/$BaTiO_3$ core-shell nanotube structure. Fig. 24a to f are the results of filling $BaTiO_3$ into AAO templates to form the nanotubes. Fig. 24f is the EDX result of these nanotubes and it shows Ti and Ba both exist in the nanotube composition.

Fig. 24g is a cross-section view of Ni/$BaTiO_3$ core-shell nanotubes structure, and Fig. 24h is a top view of core-shell nanotubes. There are some nanoparticles coated on the top of nanotubes. However, a core-shell structure can be observed from Fig. 24g.

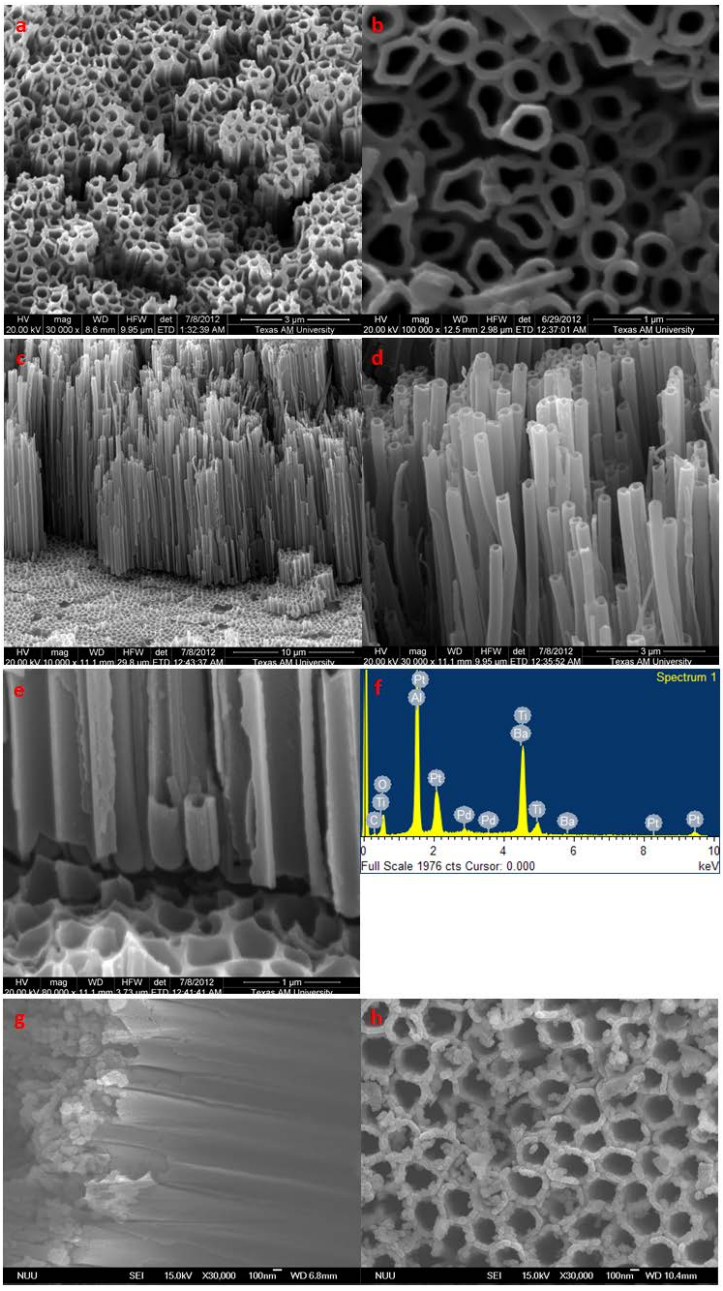

Figure 24 SEM images and EDX results of $BaTiO_3$ nanotubes and Ni/BaTiO3 core-shell nanotubes

Fig. 25 shows SEM images of the UHMWPE nanotubes array. Since UHMWPE is a very viscous polymer, the melting injection process took a longer time than other polymers, such as HDPE, to fill the entire commercial AAO template (60 µm). Nanotubes structure can be observed in Fig. 25c and d. It is important to note that the nanotube structure was observed from the melting injection instead of nanowires is due to the poor thermo conductivity of the AAO template. With a thermo conductivity worse than air, the AAO template results in a much higher temperature during the cooling process compared to the surrounding air. Therefore causing UHMWPE to contract towards the AAO template and resulted in the structure of nanotubes instead of nanowires.

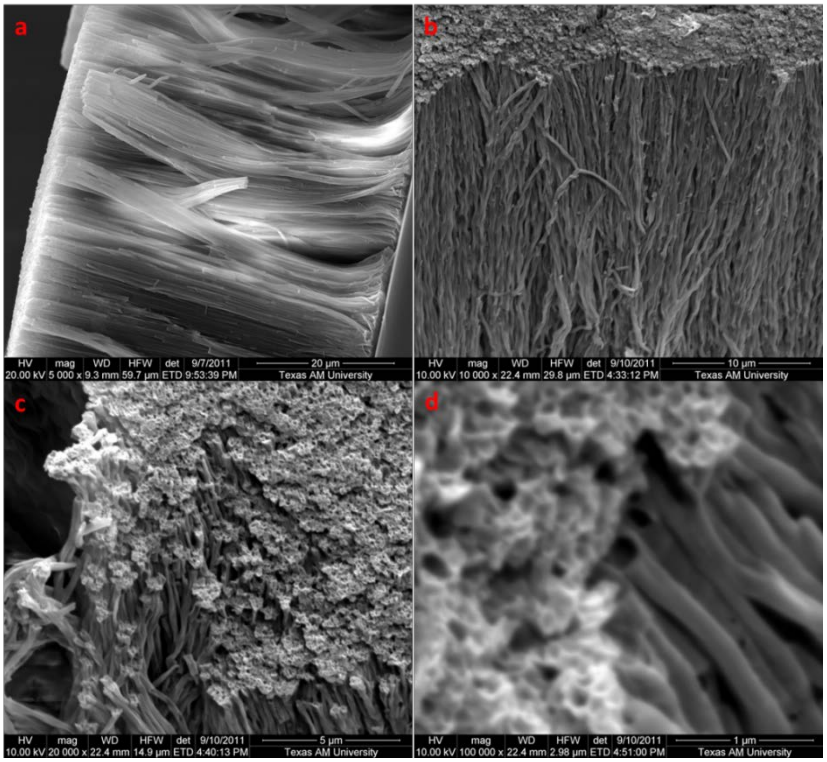

Figure 25 SEM images of UHMWPE nanotubes

4.3 Nanoengineering of the AAO Templates

4.3.1 Experimental Work

The experimental work in this subsection is conducting nanoimprinting process that leads to produce innovative AAO template. A pure Al piece (99.999%) was refined and smoothened by mechanical polishing and electropolishing in order to prevent any possible defect to affect nanoimprint process. The Al piece was first mechanically refined and polished, and annealed at 400 ^{o}C for 30 min to relieve residual stresses. The electropolishing was conducted in an electrolyte of 15 vol. % perchloric acid ($HClO_4$), 70 vol. % ethanol (C_2H_5OH) and 15 vol. % butyl cellosolve ($CH_3(CH_2)_3OCH_2CH_2OH$) solution with 40 V applied voltage at 5 ^{o}C for 10 min.

The nanoimprint mold was designed with hexagonal array of pillars in different order, pillar sizes, and inter-distance. Fig. 26 shows the SEM images of imprint mold. The pillar sizes are either ~160 or ~120 nm; the inter-distances are either ~360 or ~240 nm. There are also some designed vacancies on the imprinting mold, and the open sizes are also either ~360 nm or ~240 nm. The electropolished Al piece was directly indented by the designed imprinting mold with pressure of 100 psi. The nanoimprinted aluminum piece was anodized at 120 V in a 1 vol. % phosphoric acid (H_3PO_4) solution at 0 ^{o}C for 3 hours. The microstructures of the specimens were analyzed by field emission scanning electron microscope (SEM) (FEI Qunta 600 and JEOL JSM-7500).

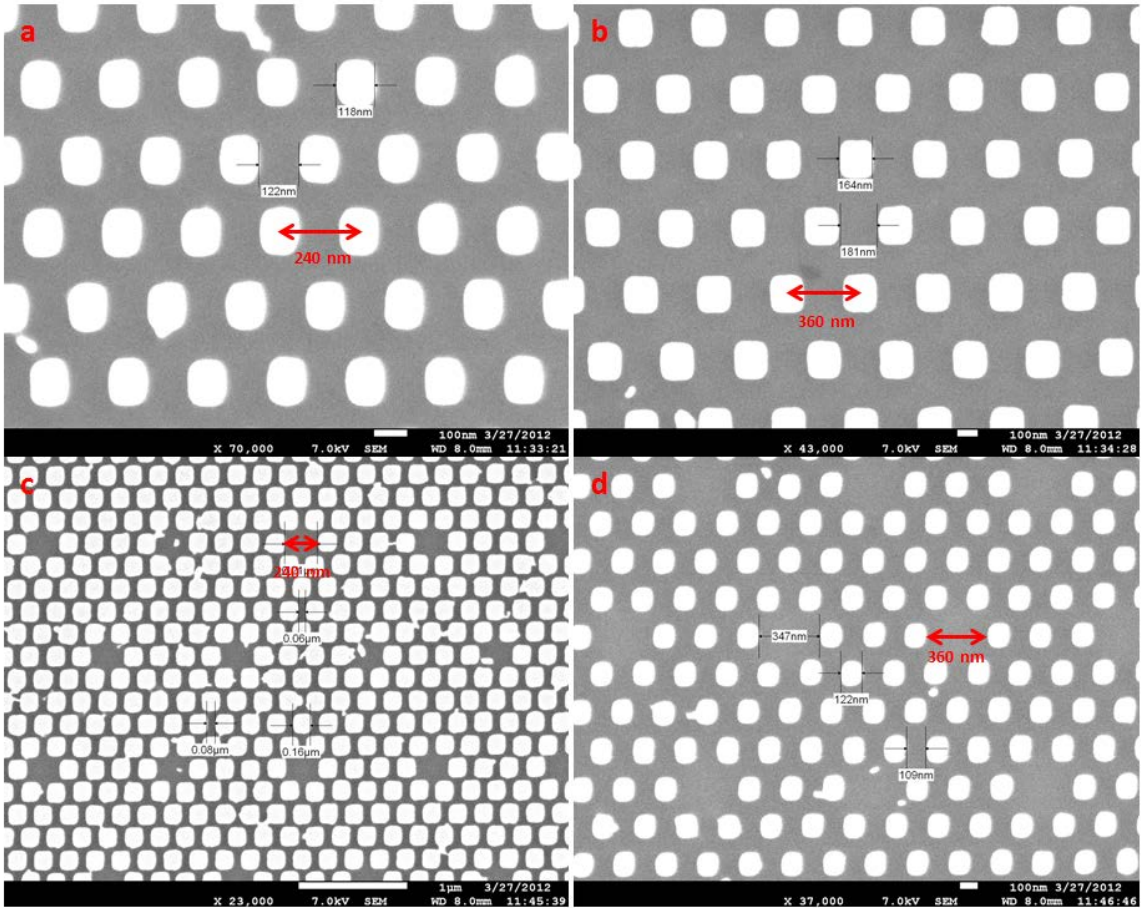

Figure 26 SEM images of imprint mold; (a) pillar size of 120 nm and inter-distance of 240 nm, (b) pillar size of 160 nm and inter-distance of 360 nm, (c) vacancy size of 240 nm, and (d) vacancy size of 360 nm

4.3.2 Results and Discussion

In order to fabricate a nanoimprinted aluminum piece, a very flat surface is critical. To indent an aluminum substrate with nanometer scale accuracy, surface roughness even with a few nanometers can be undesirable. Fig. 27 shows optical microscopic (OM) images of electropolished aluminum pieces. Fig. 27a is image of the un-annealed aluminum piece after electropolishing, and Fig. 27b shows image of the annealed one. Grain sizes and grain boundaries in Fig. 27a are much smaller than in Fig. 27b. Since grain boundaries can often be

regarded as defects on the aluminum piece for nanoimprinting, annealing not only relieves residual stresses, but drives crystalline growth to enlarge grain sizes and eliminate grain boundaries. The grains in Fig. 27b are much bigger than the nanoimprinting pattern regime, making the aluminum piece suitable for nanoimprint.

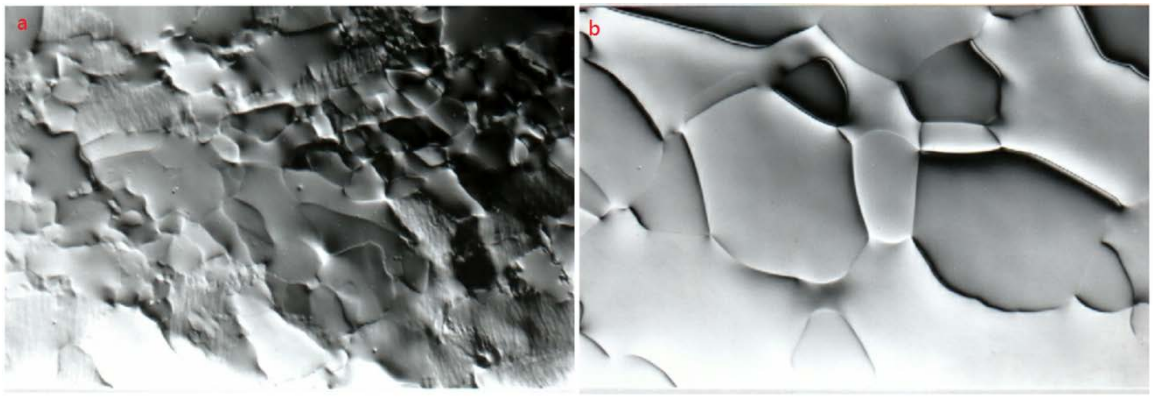

Figure 27 Images of optical microscope of electropolished aluminum pieces; (a) un-annealed, (b) annealed

Fig. 28 shows SEM images of imprinting mold of 160 nm pillar size with 120 nm pillar insertion. A 120 nm pillar substituted in every three pillars is shown in Fig. 28a, and image of a smaller dents replaced in every four pillars is in Fig. 28b. Anodizing voltage has a direct effect on pore sizes [145], and normally nanopores are around 120 nm of diameter at 120 V in H_3PO_4 solution. The results shown in Fig. 28 demonstrated that AAO formation only followed 120 nm indentations (marked in red circles). On the other hand, 160 nm indentations were too large for a single pore growth, so there was more than one nanotube formed in a single 160 nm indentation. Therefore, the location of AAO can be controlled by pattern a similar size to AAO nanopore on aluminum before anodizing.

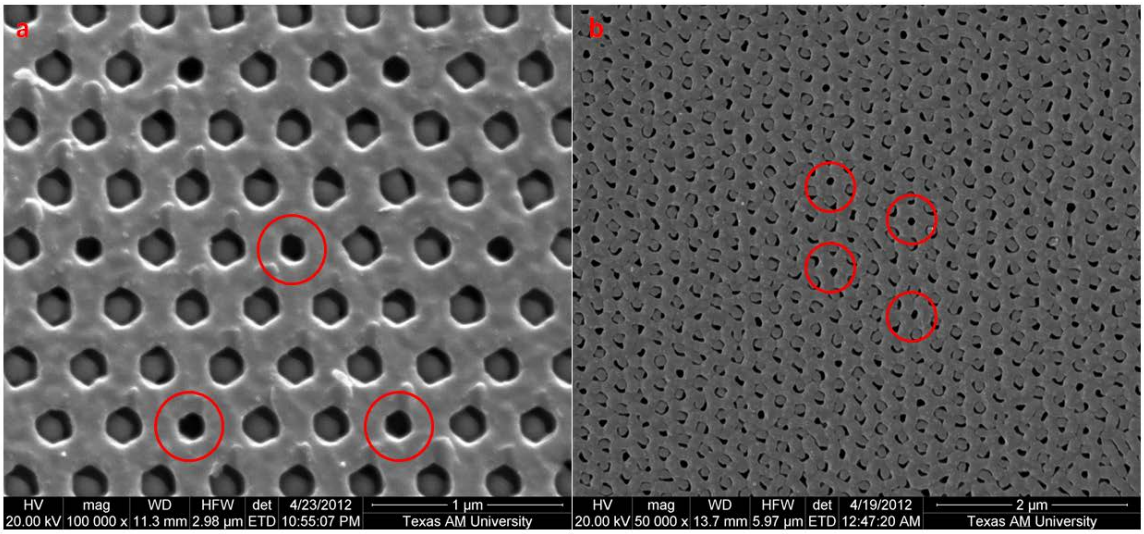

Figure 28 SEM images of imprinting mold of 160 nm pillar size with 120 nm pillar insertion; (a) every 3 pillar and (b) every 4 pillar

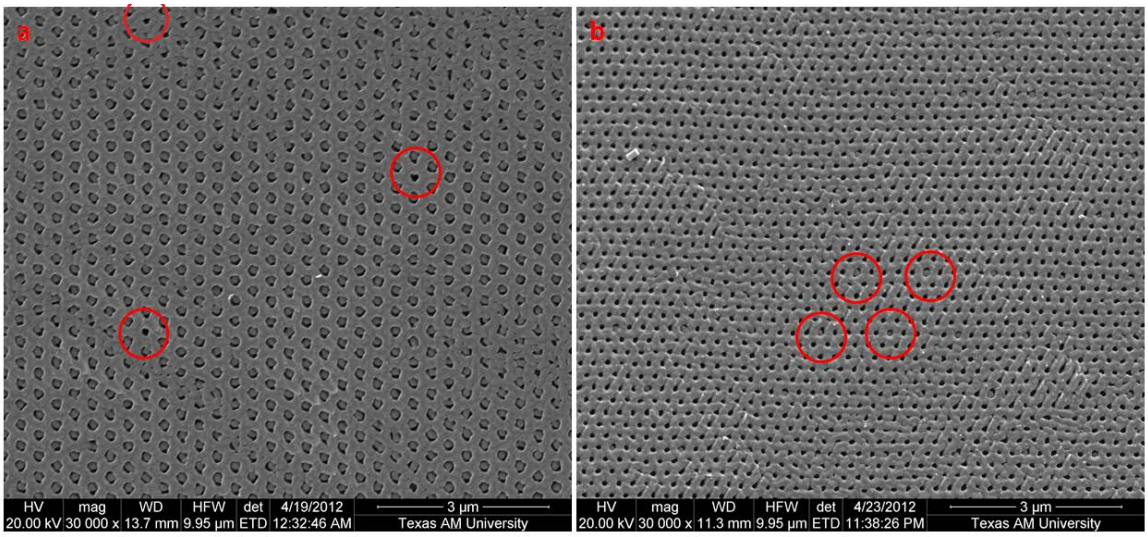

Figure 29 SEM images of AAO with different pattern; (a) smaller indentations surrounded by larger ones and (b) replace some smaller pores by larger ones

Fig. 29 shows SEM images of anodization results with different design patterns, and the results demonstrated the ability to alternate the location of nanopores with both designs. Fig. 29a shows smaller indentations (120 nm) surrounded by larger ones, and Fig. 29b is

SEM image of larger pores surrounded by smaller ones. More importantly, there are different pore sizes formed on the same piece of aluminum which still remains as a limitation of traditional AAO fabrication.

Fig. 30 shows SEM images of anodization results with the other pattern design which includes vacancies in the hexagonal array (Fig. 26c). There were two sizes of AAO nanopores in both patterns. Fig. 30a is SEM images of the AAO array from pattern with one vacancy inserted in every three indentations. Fig. 30b shows the anodized result with pattern of one vacancy introduced in every four dents. This type of design demonstrated that a suitable size of indentation is able to drive AAO forms following the shape, but AAO forms in irregular shapes on a flat surface. Therefore, inserting vacancies is another promising design to obtain different sizes nanopores in a single piece of aluminum.

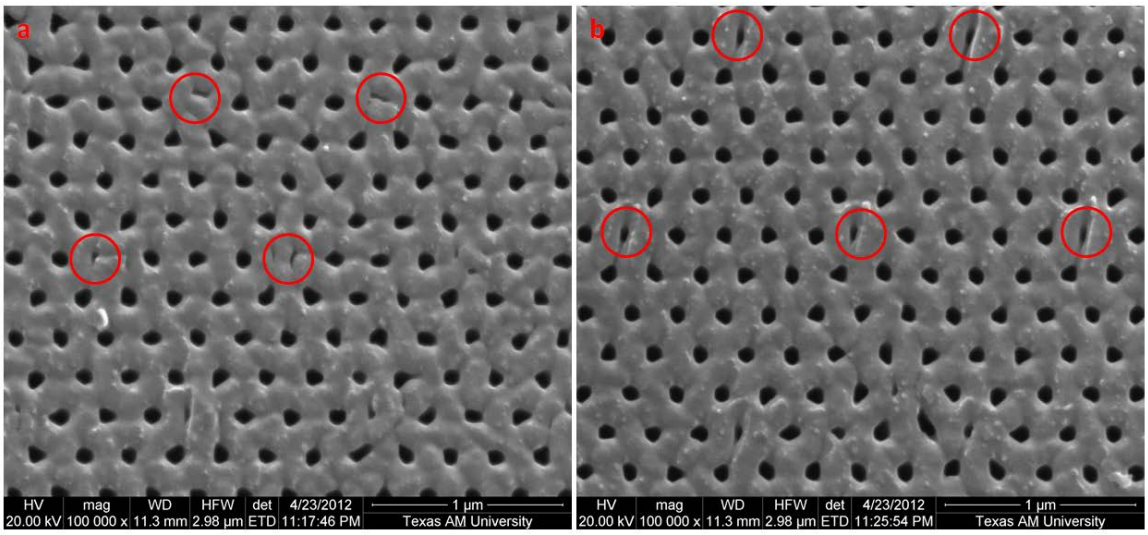

Figure 30 SEM images of AAO from inserting vacancies into patterns; a vacancy inserted (a) in every 3 indentations and (b) in every 4 indentations

4.4 Conclusion

In summary, self-ordered nanoporous AAO can be regarded as templates for fabricating various kinds of nanostructures. Metals, ceramics, and polymers can be filled into the AAO template by many processes. In this chapter, we basically show the ability to fabricate types of nanostructures with different techniques, such as electroplating, electroless deposition, sol-gel deposition and melting injection etc. We also successfully combined those techniques and fabricated Ni nanowires/ TiO_2 nanotubes, Ni/$BaTiO_3$ core-shell nanotubes, and UHMWPE nanowires. Additionally, AAO arrays were formed through a guided anodization assisted by nanoimprint process. We designed nanoimprinting patterns followed by the mechanism of AAO growth which is an ordered hexagonal array and pore sizes. We directly imprinted the designed patterns onto well-polished aluminum pieces. The guided anodization process performed the ability of controlling AAO forming locations, and more importantly it shows periodically ordered AAO array with different sizes of nanopores.

This section demonstrates applications of AAO as templates for producing ordered nanomaterials, and shows an innovative AAO fabrication process to overcome the limitation of traditional AAO array. For further developments: (1) introducing the results in this study for electronic, magnetic, or biological applications; (2) following the above results, design other nanoimprinting pattern for more specific applications; (3) introducing other fabrication processes to further control the pore densities.

5. ANODIC TITANIUM BASED ALLOY OXIDE NANOTUBES*

5.1 Introduction

The demands for energy storage and energy generation are increasing rapidly with the global energy crisis. Ultracapacitor is a technology for energy storage with advantages of low cost and high efficiency. Barium titanate ($BaTiO_3$), which exhibits a very high dielectric constant, is a good material for ultracapacitor fabrication. [146-149] However, the processes of producing $BaTiO_3$, such as hydrothermal treatment [150, 151], metal-organic process [152], alkoxide hydrolysis [153, 154], R.F.-sputtering [155], and sol-gel process [156], have been reported and they are very complex and costly. Titanium dioxide (TiO_2) can be formed nanotube by one-step anodizing process compared with the complex processes fabricating $BaTiO_3$. However, the dielectric constant of TiO_2 is not as high as $BaTiO_3$, but TiO_2 nanotube could be an ideal dielectric template due to its high surface area. A typical TiO_2 nanotube fabrication can be achieved by anodization [157], and the ordered channel-array of anodic titanium oxide nanotubes are able to serve as multiple parallel dielectric layers for the ultracapacitor.

On the other hand, metals (Al [158], Hf [159], Nb [160], Ta [161], W [162], V [163]) and alloys (Ti-Mo [164], Ti-W [165], Ti-Nb [166],Ti-V [167], Ti-Zr [168],Ti-Ta [169], Ti-Al [170]) have been reported that they can also be formed high surface area of nanoporous oxide film. WO_3, Ta_2O_5, and $TaTiO_3$, which have higher dielectric constants than TiO_2, of 1000

* Part of this section is reprinted with permission from "The Microstructure and Capacitance Characterizations of Anodic Titanium Based Alloy Oxide Nanotube" by Po-Chun Chen, Sheng Jen Hsieh, Chien Chon Chen, and Jun Zou, 2013. *Journal of Nanomaterials*, Vol. 2013, 157494, Copyright [2013] Hindawi Publishing Co.

[171], 110 [172], and 200 [173], are the alternate dielectric materials for ultracapacitor. Unfortunately, they cannot form nanotubes structures as good as TiO_2 nanotubes. Thus, in this section, we used a simple process of anodization to fabricate TiO_2, TiO_2-MoO_3, and TiO_2-Ta_2O_5 nanotubes. Their high dielectric constants and large surface areas are very useful materials to build ultracapacitors. Based on the nanotube structural properties, such as diameter, porosity, and length, we also investigated the specific capacitances of the different titanium alloys.

5.2 Experimental Work

5.2.1 Materials and Methods

An ordered channel-array of anodic titanium and titanium alloy oxides were fabricated by anodizing Ti, Ti-10Ta (90 wt. % Ti +10wt. % Ta), Ti-20Ta (80 wt. % Ti +20wt. % Ta), and Ti-10Mo (90 wt. % Ti +10wt. % Mo) alloys. The metal substrates were first put through electro-polishing (EP). The EP electrolyte included 5 vol. % perchloric acid ($HClO_4$), 53 vol. % ethylene glycol monobutylether ($HOCH_2CH_2OC_4H_9$), and 42 vol. % methanol (CH_3OH). EP processes of Ti and Ti alloys were conducted at 15 ^oC under 52 V for 1 minute and 28 V for 13 minutes with platinum as a counter electrode at a constant stirring rate of 200 rpm. After EP, the samples were etched in 5 vol. % HF for 5 min to form an additional thin anodic film on the metal substrates. TiO_2, TiO_2-Ta_2O_5, and TiO_2-MoO_3 nanotubes were anodized in an electrolyte of 0.5 wt. % ammonium fluoride (NH_4F, 99.9%) and 2 wt. % H_2O in ethylene glycol ($C_2H_4(OH)_2$) solvent at a constant voltage of 60V for 2 hours. After anodic films were formed by anodization, the films were then annealed in an air furnace at 450 ^oC for 1 hour for crystallization. The surface morphologies of the anodic oxides were observed

by using a scanning electron microscope (SEM, FEI Quanta 600). The alloy oxide nanotubes compositions can be analyzed by Energy Dispersive Spectrometer (EDS) (Oxford).

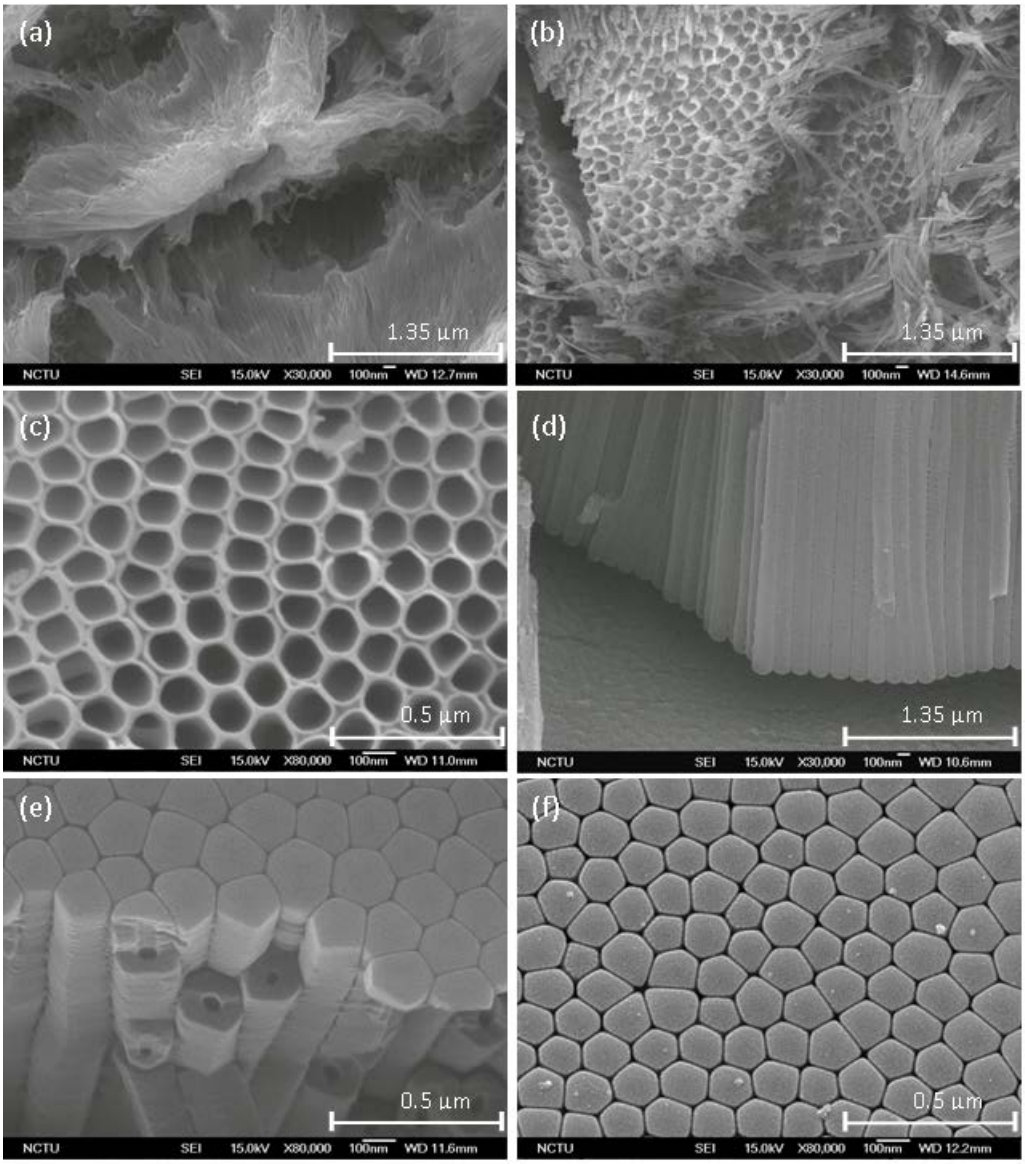

Figure 31 SEM images of TiO_2 NT; (a) an unwanted film cover on TiO_2 NT, (b) removed partial unwanted film, (c) removed all unwanted film and presented TiO_2 NT, (d) TiO_2 NT side view, (e) TiO_2 NT bottom view, and (d) an barrier layer on the TiO_2 NT bottom.

5.2.2 Electrolytic Characterization

Cyclic voltammetry (CV) performances were evaluated by an electrochemical analyzer (CH Instruments, Model 600B, USA) using a standard three-electrode cell system with platinum as a counter electrode and silver-silver chloride electrode (Ag/AgCl) as a reference electrodes in 0.5M H_2SO_4 solution at room temperature. The CV scan rate was set as 20 mV/s in a potential range of 0 V to 0.9 V (Ag/AgCl).

5.3 Discussion and Conclusion

Fig. 31 presents the SEM images of long-range ordered nanochannel TiO_2 NT structures form anodizing pure Ti foil, (a) an unwanted film covered on TiO_2 NT, (b) removed partial unwanted film, (c) removed all unwanted film and the top view of TiO_2 NT, (d) side view of TiO_2 NT, (e) bottom view of TiO_2 NT, and (f) an barrier layer under the TiO_2 NT. TiO_2 NT feature a pore diameter ~120 nm, pore density ~8×10^9 pores cm^2, and wall thickness ~25 nm; the length of the NT can be controlled from several μms to hundred μms with different types of the electrolytes (for example NH_4F) and the anodization times at a constant applied voltage (for example 60V).

Immersing titanium in electrolyte occurs complex reactions with 16 forms of Ti ions and oxides. [28] The Pourbaix diagram is useful to simplify the complex reactions. [174] Based on the Pourbaix diagram of Ti (Fig. 32a), TiO^{+2} ion is a favorite formation when pH value lower than 2.3 and voltage higher than -0.2 V (SHE) at 25°C. TiO^{+2} can further react with H_2O to from $Ti(OH)_4$ which is anodic titanium oxide. Similarly, Ta Pourbaix diagram (Fig. 32b) shows that TaO^{2+} is formed and converted to Ta_2O_5 under the condition of pH < 5.1 and applying voltage > -1.2 V (SHE) at room temperature. As well as Mo Pourbaix diagram (Fig. 32c) implies that Mo^{3+} can be produced and form MoO_3 in the condition of pH

is below 4.2 and voltage is higher than -0.35 V (SHE) at 25°C. However, anodic TiO_2, MoO_3, and Ta_2O_5 can be formed in the neutral pH value electrolyte when it contains halogen element in it.

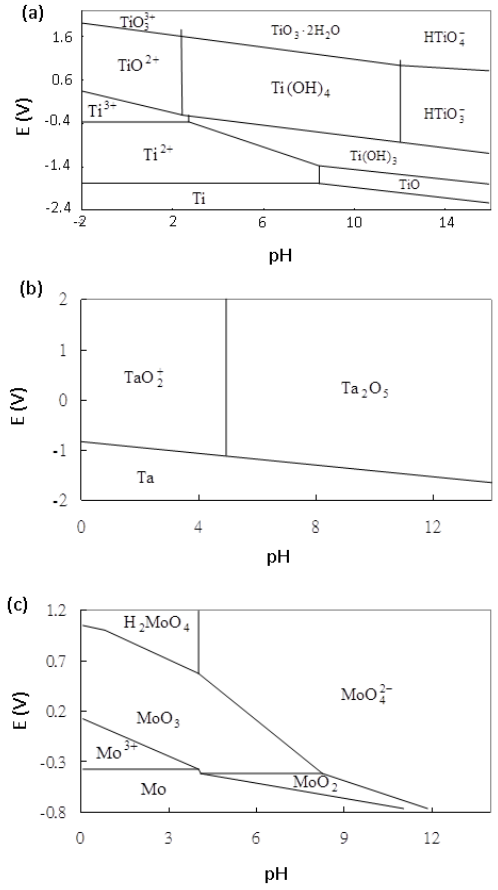

Figure 32 Pourbaix diagrams of (a) Ti, (b) Ta, and (c) Mo

Anodization of titanium forms close-packed and vertical-aligned nanotubes in a non-aqueous organic polar electrolyte with F^- ions and minimizing water content. These eletcrochemical processes can be described as follows [175-178]:

$$Ti \rightarrow Ti^{4+} + 4e^- \qquad \text{(Eq. 5-1)}$$

$$H_2O \rightarrow 2H^+ + O^{2-}$$ (Eq. 5-2)

$$Ti^{4+} + 2O^{2-} \rightarrow TiO_2$$ (Eq. 5-3)

$$Ti^{4+} + 2H_2O \rightarrow 4H^+ + TiO_2$$ (Eq. 5-4)

$$6F^- + TiO_2 + 4H^+ \rightarrow [TiF_6]^{2-} + 2H_2O$$ (Eq. 5-5)

$$[TiF_6]^{2-} + nH_2O \rightarrow [TiF_{6-n}(OH)_n]^{2-} + nH^+ + nF^-$$ (Eq. 5-6)

$$[TiF_{6-n}(OH)_n]^{2-} + (6-n)H_2O \rightarrow [Ti(OH)_6]^{2-} + (6-n)H^+ + (6-n)F^-$$ (Eq. 5-7)

$$[Ti(OH)_6]^{2-} + 2H^+ \rightarrow TiO_2 + 4H_2O$$ (Eq. 5-8)

During anodization, there are oxidation reactions at the interface between metal and electrolyte. Ti^{4+} is formed and the water in the electrolyte is decomposed, reaction (5-1) and (5-2). TiO_2 are then formed between the metal and the electrolyte through ion migration, reaction (5-3) and (5-4). F^- ions etch the TiO_2 forming TiF_6^{2-} and then combine with the H_2O to form $[TiF_{6-n}(OH)_n]^{2-}$, reaction (5-5) and (5-6). Because the F^- ions are doped in the TiO_2 but not form a compound, reaction (5-6) can be rewritten as (5-7). Finally, $[Ti(OH)_6]^{2-}$ reacts with $2H^+$ to form TiO_2 nanotubes, reaction (5-8).

Based on the Eq. 5-1 to 5-8, anodization of Ta can be described as:

$$Ta \rightarrow Ta^{5+} + 5e^-$$ (Eq. 5-9)

$$H_2O \rightarrow 2H^+ + O^{2-}$$ (Eq. 5-10)

$$2Ta^{5+} + 5O^{2-} \rightarrow Ta_2O_5 \quad \text{(Eq. 5-11)}$$

$$2Ta^{5+} + 5H_2O \rightarrow 10H^+ + Ta_2O_5 \quad \text{(Eq. 5-12)}$$

$$12F^- + 2TaO_5 + 10H^+ \rightarrow 2[TaF_6]^- + 5H_2O \quad \text{(Eq. 5-13)}$$

$$2[TaF_6]^- + 2nH_2O \rightarrow 2[TaF_{6-2n}(OH)_{2n}]^- + 2nH^+ + 2nF^- \quad \text{(Eq. 5-14)}$$

$$2[TaF_{6-2n}(OH)_{2n}]^- + (6-2n)H_2O \rightarrow [Ta(OH)_6]^- + (6-2n)H^+ + (6-2n)F^- \quad \text{(Eq. 5-15)}$$

$$2[Ta(OH)_6]^- + 2H^+ \rightarrow Ta_2O_5 + 7H_2O \quad \text{(Eq. 5-16)}$$

Also, anodization of Mo can be described as:

$$Mo \rightarrow Mo^{3+} + 3e^- \quad \text{(Eq. 5-17)}$$

$$H_2O \rightarrow 2H^+ + O^{2-} \quad \text{(Eq. 5-18)}$$

$$Mo^{3+} + 3O^{2-} \rightarrow MoO_3 \quad \text{(Eq. 5-19)}$$

$$Mo^{3+} + 3H_2O \rightarrow 6H^+ + MoO_3 \quad \text{(Eq. 5-20)}$$

$$6F^- + MoO_3 + 6H^+ \rightarrow [MoF_6]^{3-} + 3H_2O \quad \text{(Eq. 5-21)}$$

$$[MoF_6]^{3-} + nH_2O \rightarrow [MoF_{6-n}(OH)_n]^{3-} + nH^+ + nF^- \quad \text{(Eq. 5-22)}$$

$$[MoF_{6-n}(OH)_n]^{3-} + (6-n)H_2O \rightarrow [Mo(OH)_6]^{3-} + (6-n)H^+ + (6-n)F^- \quad \text{(Eq. 5-23)}$$

$$[Mo(OH)_6]^{3-} + 3H^+ \rightarrow MoO_3 + 3H_2O \quad \text{(Eq. 5-24)}$$

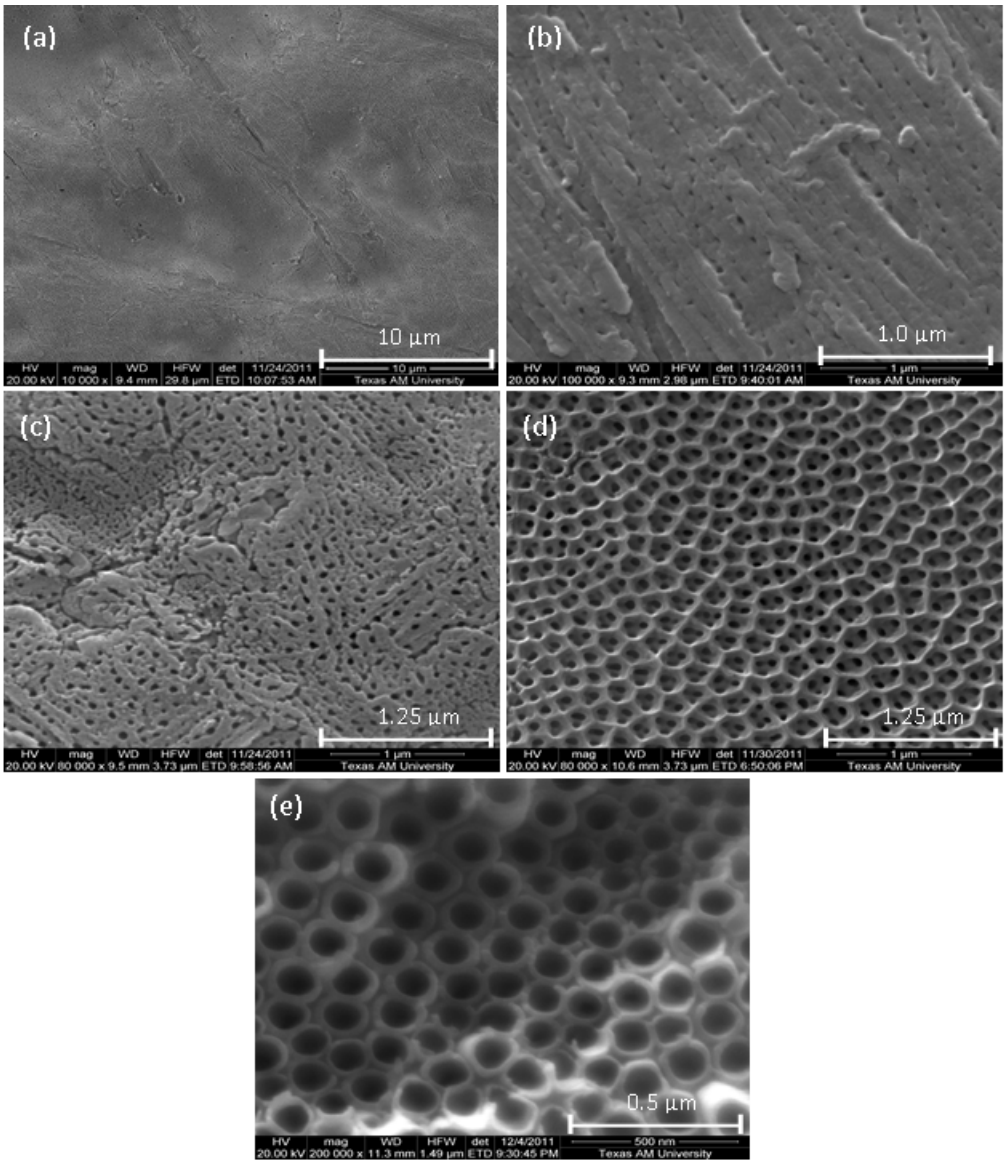

Figure 33 SEM images of Ti-Ta NT film structure; (a) compact layer, (b) partial porous film, (c) porous film (d) net film, (e) Ti-Ta NT.

Fig. 33 shows SEM images of TiO_2-Ta_2O_5 nanotubes structure from anodizing Ti-10Ta alloy. There was a compact layer on the top of nanotubes in Fig. 33a. A continuous

porous layer and grain boundary under the compact layer are observed in Fig. 33b. Fig. 33c shows a porous film is covering the compact layer and following a net structure (Fig. 33d) is covering the gap between ordered TiO_2-Ta_2O_5 nanotubes (Fig. 33e). There were extra continuous porous layer and net structure which were not presented on pure TiO_2 nanotubes. The compact layer, continuous porous layer, and net structure were removed by 5 wt. % of 1 μm Al_2O_3 powders in ethanol solvent assisted by ultrasonic vibration. Similar to Ti-10Ta alloy, Fig. 34 shows SEM images of TiO_2-Ta_2O_5 nanotube by anodizing Ti-20Ta alloy. Fig. 34a shows a net film on the NT top, Fig. 34b without a net film on the NT top, Fig. 34c a barrier layer on the NT bottom, Fig. 34d partial barrier layer under the NT.

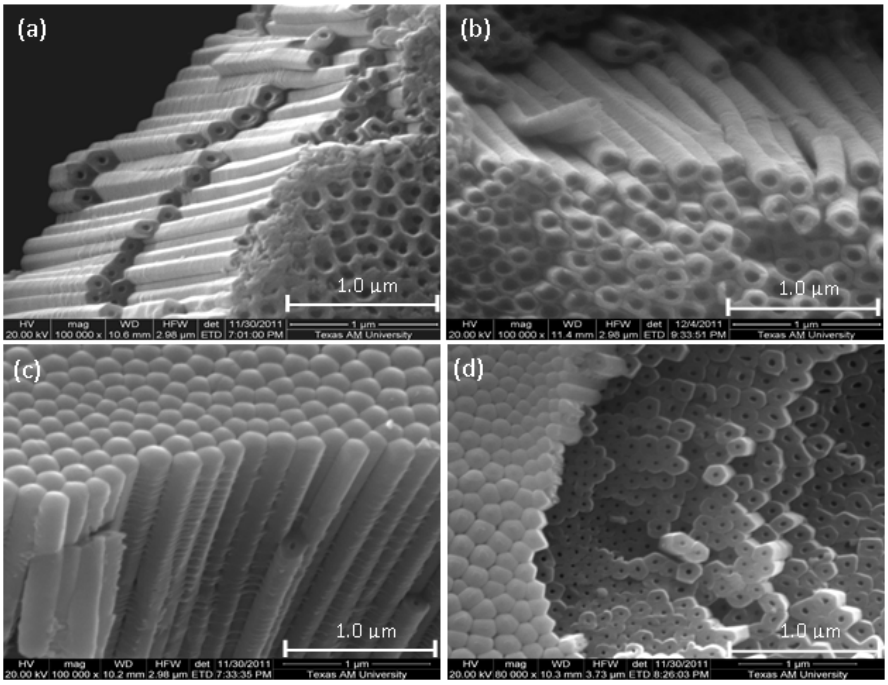

Figure 34 SEM images of TiO_2-Ta_2O_5 nanotubes film by anodizing Ti-20Ta alloy; (a) a net film on the NT top, (b) without a net film on the NT top, (c) a barrier layer on the NT bottom, (d) partial barrier layer on the NT bottom

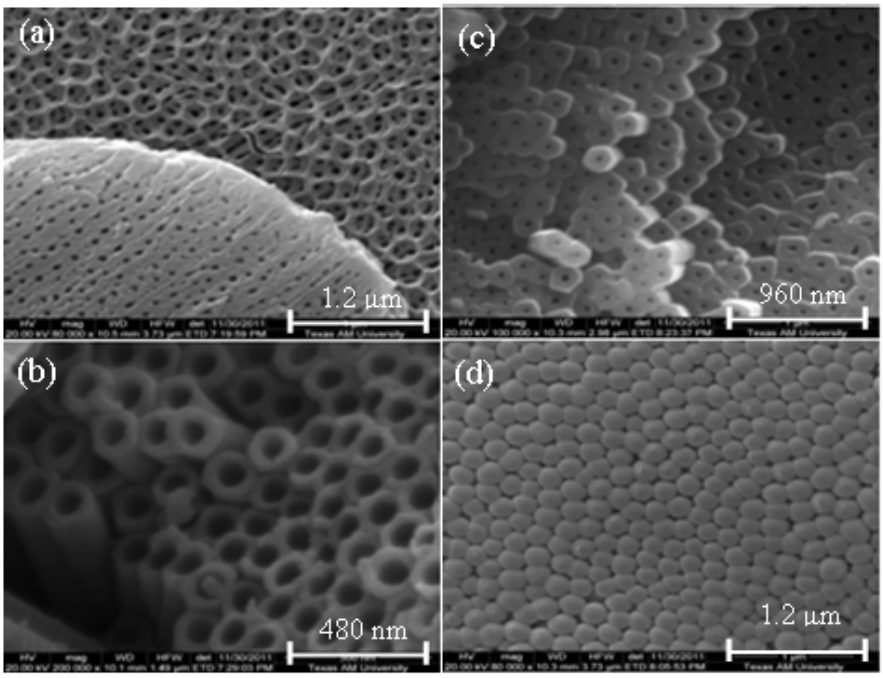

Figure 35 SEM images of TiO_2-MoO_3 nanotubes film by anodizing Ti-10Mo alloy; (a) a top view of the net structure, (b) without a net film on the NT top, (c) smaller pores nanotubes, (d) barrier layer on the bottom

For the Ti-10Mo alloy, Fig. 35a shows partially removed continuous porous layer on the net structure, larger pores on the top of TiO_2-MoO_3 nanotubes (Fig. 35b), smaller pores (Fig. 35c), and barrier layer (Fig. 35d) on the bottom side. According to Fig. 33 to Fig. 35, Fig. 36 is a schematic diagram of anodic Ti-alloy oxide structure with compact layer, continuous porous layer, net structure, and ordered nanotubes on the alloys surfaces.

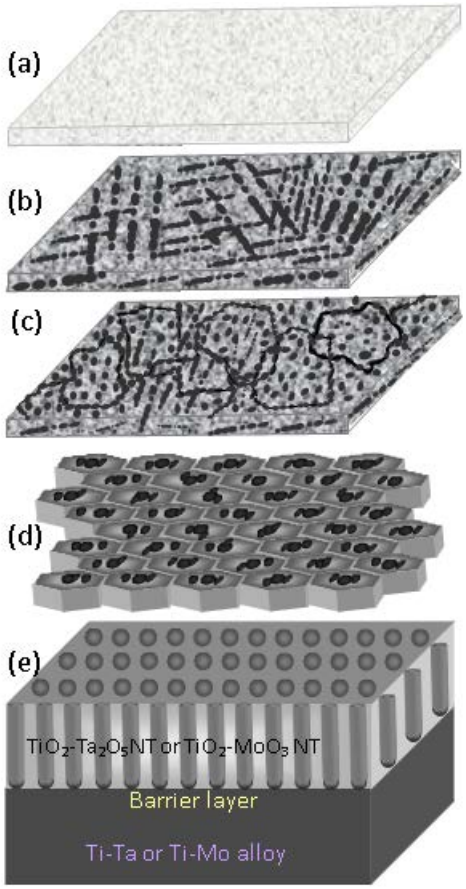

Figure 36 The schematic diagram of TiO_2-Ta_2O_5 NT or TiO_2-MoO_3 NT film structure; (a) compact layer, (b) partial porous film, (c) porous film (d) net film, (e) TiO_2-Ta_2O_5 NT or TiO_2-MoO_3 NT and barrier layer on the Ti-Ta or Ti-Mo alloy

Fig. 37 shows a schematic structure and geometry of the Ti alloy oxide nanotube. Larger open pores are on the top (Fig. 37a), smaller closed pores and a barrier layer in a hexagonal pattern are on the bottom side (Fig. 37b), tube inner surface area (Fig. 37c), and outer surface area (Fig. 37d). Denoting R_1 and R_2, and T_1 and T_2 are the radius and pores width of the top and bottom pores, respective, W is the thickness of the outer barrier layer, and H and L is the inner height and total length of the nanotube. We have $R_1 + T_1 = R_2 + T_2 =$

R_3, and total length of nanotube is $L = H + W$. Thus, the volume of a single alloy oxide can be calculated by $V = V_{outer} - V_{inner}$ where V_{outer} and V_{inner} can be obtained by:

$$V_{outer} = \pi R_3^2 \times L \quad \text{(Eq. 5-25)}$$

$$V_{inner} = \frac{1}{3}\pi \times \frac{H}{R_1 - R_2} \times (R_1^3 - R_2^3) \quad \text{(Eq. 5-26)}$$

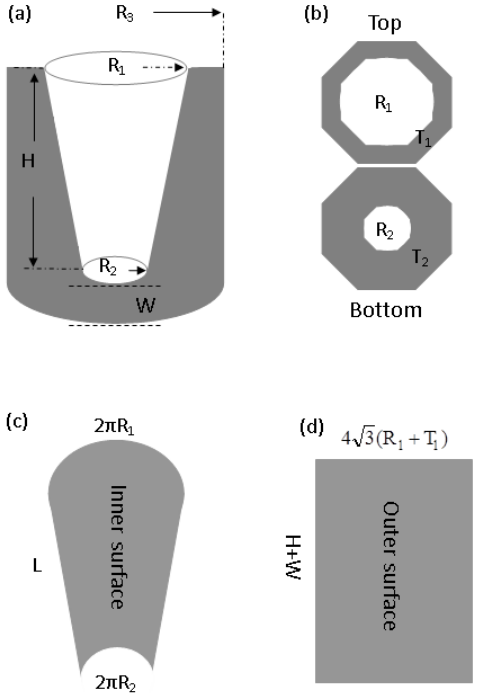

Figure 37 Estimation of TiO_2 NT surface; (a) cone structure of inner tube with radius of R_3, and R_1, and R_2 on the tube top and bottom, tube length with H (b) pore wall thickness with T_1 and T_2 on the tube top and bottom, (c) tube inner surface area, and outer surface area

Based on the SEM images in Fig. 33, 34, 35, R_1, R_2, R_3, and W were 60 nm, 25 nm, 80 nm, and 40 nm, respectively. For two hours anodization process, 20 μm length of Ti alloy oxide nanotubes (L) could be formed on the Ti alloy surface. Thus, V_{outer} was 0.4 μm^3,and V_{inner} was 0.12 μm^3, and the volume of a single alloy oxide nanotube (V) was 0.28 μm^3. The

TiO_2 nanotubes density has recently reported by Chen *et al.* [28] that there are 4,510,548,978 nanotubes per cm^2. Therefore, the total volume of Ti alloy nanotubes was 1.26×10^{-3} cm^3 in 1 cm^2 sample area. Moreover, it has also been reported that nanotube surface area is greatly increased when L = 10 μm, S_{inner} = 120.5 cm^2, S_{outer} = 240.2 cm^2, and L = 100 μm, S_{inner} = 1205 cm^2, S_{outer} = 2402 cm^2. Fig. 38 furthermore accumulated anodic Ti and Ti alloy NT inner and outer surface areas increased with film thickness increased based on 1 cm^2 substrate. Hence, the extremely high surface area is able to provide more chances for electrochemical reactions.

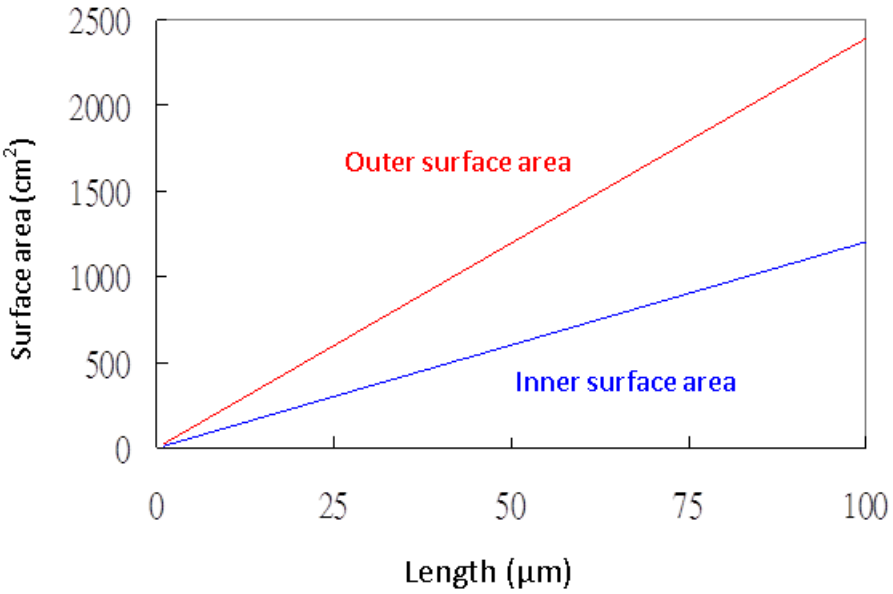

Figure 38 Accumulated anodic Ti and Ti alloy NT inner and outer surface areas based on 1cm^2 substrate

According to the Pourbaix diagrams in Fig. 32, anodize Ti, Ti-20Ta, Ti-10Ta, and Ti-10Mo can form anodic oxide films of these Ti alloys. Therefore, the following alloy anodic oxide films densities are able to be calculated based on the TiO_2, Ta_2O_5, and MoO_3 densities

of 4.2 g/cm^3, 8.2 g/cm^3, and 4.7 g/cm^3, respectively. According to EDS results in Table 1, Ti, Ti-20Ta, Ti-10Ta, and Ti-10Mo formed 100% TiO_2, 83.9% TiO_2+16.1% Ta_2O_5, 91.3% TiO_2+8.7% Ta_2O_5, and 92.8% TiO_2+7.2% MoO_3. The densities of 100% TiO_2, 83.9% TiO_2+16.1% Ta_2O_5, 91.3% TiO_2+8.7% Ta_2O_5, and 92.8% TiO_2+7.2% MoO_3 were 4.23 g/cm^3, 4.84 g/cm^3, 4.54 g/cm^3, and 4.24 g/cm^3, respectively. Therefore, the mass of nanotubes films 1 cm^2 sample for each alloy was listed in Table 2 which were 5.32 mg/cm^2, 6.09 mg/cm^2, 5.72 mg/cm^2, and 5.34 mg/cm^2.

Table 1 EDS results of Ti alloys oxide nanotubes

	TiO_2 (%)	Ta_2O_5 (%)	MoO_3 (%)
Ti-20Ta	83.9	16.1	0
Ti-10Ta	91.3	8.7	0
Ti-10Mo	92.8	0	7.2

Cyclic voltammograms (CV) is used to characterize the capacitors behavior of the alloy oxide nanotubes. Fig. 39 shows capacitance performance evaluations for the Ti alloy anodic oxide nanotubes by cyclic voltammograms. It is clear that Ti alloy oxide nanotubes had larger area of CV curve than pure TiO_2 nanotube did. It means Ti alloys oxide nanotubes had larger capacitances than pure TiO_2 nanotubes. Besides, more Ta_2O_5 content can significantly enhance the capacitor performance by comparing two Ti-Ta alloys curves with different compositions. Moreover, Ti-10Mo alloy oxide nanotubes CV curve shows a symmetrical shape which indicates that the revisable redox reaction of Mo^{2+}/Mo^{3+} was helpful to improve the capacitor performance.

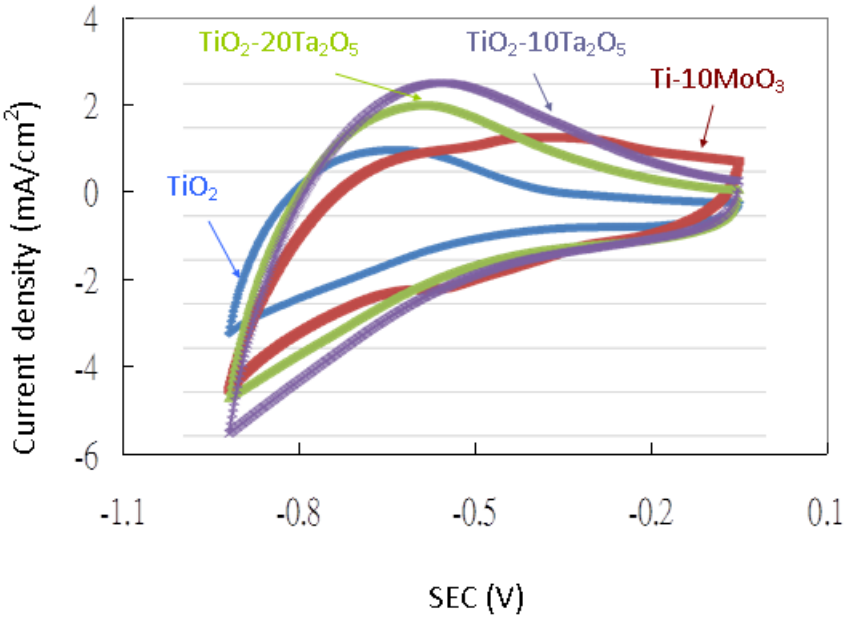

Figure 39 Capacitance performance evaluations for TiO_2 NT, TiO_2-10 Ta_2O_5 NT, TiO_2-20 Ta_2O_5 NT, and TiO_2-10 MoO_2 NT by Cyclic Voltammograms

The specific capacitance (C) can be measured by voltage step, current step, or voltage ramp methods, and evaluated by the equations of, C = Q/V, or C = dQ/dV [179], where V is applied voltage and Q is the quantity of charge on the electrode (which can be evaluated from the area of the CV curve). Table 2 shows the specific capacitance based on $1cm^2$ sample area and 20 μm film thickness of pure Ti, Ti-20Ta, Ti-10Ta, and Ti-10Mo oxide nanotubes films which are 13.7 F/g, 26.1 F/g, 23.3 F/g, and 21.4 F/g, respectively. The specific capacitances of Ti alloys oxide nanotubes films were higher than that of TiO_2-B nanowires/MWCNTs hybrid supercapacitor with specific capacitance of 17.7 F/g [180].

Table 2 Specific capacitance based on TiO_2 NT, Ti-10Ta NT, Ti-20Ta NT, and Ti-10Mo NT films

Sample size ($1cm^2 \times 20\mu m$)	TiO_2 NT	Ti-10Ta NT	Ti-20Ta NT	Ti-10Mo NT
Density (g/cm^2)	3.09	3.19	3.65	3.07
Mass of unit area (mg/cm^2)	6.18	6.38	7.30	6.14
dQ (mC)	65.58	120.02	143.30	102.92
dE (V)	0.9	0.9	0.9	0.9
Specific capacitance (F/g)	11.8	20.9	21.8	18.6

In summary, we fabricated supercapacitors based on the working electrode made of highly ordered anodic TiO_2, Ta_2O_5, and, MoO_3 nanotubes directly formed on pure Ti, Ti-20Ta, Ti-10Ta, and Ti-10Mo substrates. The ordered alloys oxide nanotubes structure has a volume of 1.26×10^{-3} cm^3 in 1 cm^2 sample area with nanotube density of 4.5×10^9 tubes/cm^2. The mass of pure Ti and Ti alloys oxide nanotubes films with 1 cm^2 sample size and 20 μm film thickness can be calculated as 5.32 mg (TiO_2 nanotubes), 6.09 mg (Ti-20Ta oxide nanotubes), 5.72 mg (Ti-10Ta oxdie nanotubes), and 5.34 mg (Ti-10Mo oxide nanotubes), respectively. Furthermore, Ti alloy anodic oxide nanotubes films with 1 cm^2 surface and 20 μm thickness have an inner surface area of 241.0 cm^2 and outer surface area of 480.4 cm^2. Thus, such large surface area of dielectric oxides caused very high specific capacitances. The specific capacitance can further be enhanced by: (1) reacting with barium nitrate ($Ba(NO_3)_2$) [181] or barium hydroxide ($Ba(OH)_2$) [182] to form a very high dielectric constant $BaTiO_3$ film, (2) increasing nanotubes length by longer anodization process, and (3) increasing nanotubes surface area by coating TiO_2 nanoparticles on the nanotubes surface [183].

6. SELECTIVELY DEALLOYING Ti/TiO_2 NANOSTRUCTURE FOR SUPERCAPACITOR APPLICATION

6.1 Introduction

Electrochemical supercapacitor is also called pseudocapacitor. Metal oxides [97], metal oxide/ carbon composites, and conducting polymer/carbon composites [98] are electrode materials to construct supercapacitors that can achieve high capacitances. Some transition metal oxides have been investigated as supercapacitor electrode materials, such as RuO_2, NiO, $Ni(OH)_2$, MnO_2, Co_2O_3, IrO_2, FeO, TiO_2, SnO_2, V_2O_5, and MoO. [184-187] Among the transition metal oxides, TiO_2 is non-toxic, inexpensive and very available. It has been investigated as supercapacitor electrode material or co-material with other metal oxides, such as nanosize TiO_2 and activated carbon. [188-191] However, there is one major disadvantage of these supercapacitors is their low specific stored energy. [103] Therefore, it is impotant to fabricate electrode materials can accumulate large quantity of electrons and energy for supercapacitor needs.

Nanoporous metallic materials have unique properties, such as large surface-to-volume ratio, light weight, and excellent electrical/thermal conductivity. They are able to improve performance in chemical, electrical, optical behaviors, and they also can be used in catalysis, mircofiltration, sensors, drug delivery system. [1-5] Moreover, nanoporous metals contribute many improvements and developments to supercapacitors. Nanoporous metals with large surface areas can provide larger interface for forming double layer to charge/discharge in EDLCs. [18] Nanoporous metals also provide the possibility for a better

mechanism for ion transportation in the redox reaction. These properties of capacitive nanomaterials can be applied to supercapacitors for a better and improved performance. [19] There are various approaches have been approved to fabricate nanoporous metals. [6, 7] Among these processes, dealloying has been demonstrated to be very effective in generating free-standing 3-D nanoporous metals. Unlike traditional nanoparticle-based materials, nanoporous metals obtained by dealloying hold a unique combination of a highly conductive network and a bicontinuous open nanoporousity. Additionally, pore size and porousity can be determined by mechanical methods or heat treatments, such as rolling, and annealing. Dealloying in aqueous solution is a promising technique for preparing homogeneous nanoporous metals. Dealloying processes are affected by many parameters, such as alloy composition, solution composition, temperature, and treatment time. Some alloy systems have been investigated to form uniform nanoporous structure, for example, Au/Zn, Au/Cu, Au/Ag, Pt/Si, Pt/Cu, and Al/(Au,Ag,Pd), etc. [12-17]

In this section, superelastic shape memory alloy “Nitinol”, which is near equiatomically composed of nickel and titanium, is chosen as the raw alloy for dealloying process. Dealloying of nitinol has been investigated by some high temperature process before, such as high-temperature oxochloridation and reduction annealing. [192] Electrochemical selective etching is conducted in this study for removing Ni from nitinol in order to acquire nanoporous titanium structure. Nanoporous titanium has attractive properties including high strength, low weight, corrosion assistance, biocompatibility, and high dielectric constant. TiO_2 also can be converted to $BaTiO_3$, which has very high dielectric constant (ε=1500). [193] Thus, nanoporous $BaTiO_3$ dielectric layer are possible to fabricate with one step

process from Ti or TiO_2 nanoporous structure. [194] In this section, we proposed to develop a nanoporous TiO_2 with metal network inside for supercapacitor application.

6.2 Experimental Work

6.2.1 Dealloying and Oxidation of NiTi Alloy

We used a commercial nitinol wire with 1 mm diameter, and the alloy composition is atomically 50-50% of nickel and titanium (ρ= 6.45 gcm^{-3}). It was finished with oxide protection and met ASTM F2063 specifications. The dealloying process was conducted by electrochemical etching in 25% nitric acid, and 12.5% hydrogen peroxide at room temperature. After removing nickel, titanium nanoporous structure was formed and oxidized by electrochemical anodization in 1 M phosphoric acid at 20 V for 1 sec at room temperature. Then, anodized sample was annealed at 450 ^oC for TiO_2 crystallization for 30 min.

The surface morphologies of the dealloyed nanostructure were observed by scanning electron microscope (SEM, FEI Quanta 600). The composition changes were analyzed by X-ray diffraction (XRD, Bruker D2 Phaser) and energy dispersive X-ray spectrum (EDS, Oxford).

6.2.2 Electrolytic Characterization

Cyclic voltammetry (CV) performances were evaluated by an electrochemical analyzer (CH Instruments, Model 600B) using a standard three-electrode cell system with platinum as a counter electrode and saturated silver-silver chloride electrode (Ag/AgCl) as a reference electrode in 0.5 M sulfuric acid solution at room temperature. The CV scan rate was set as 20 mV/s in a potential range of 0.1 V to 0.9 V (Ag/AgCl).

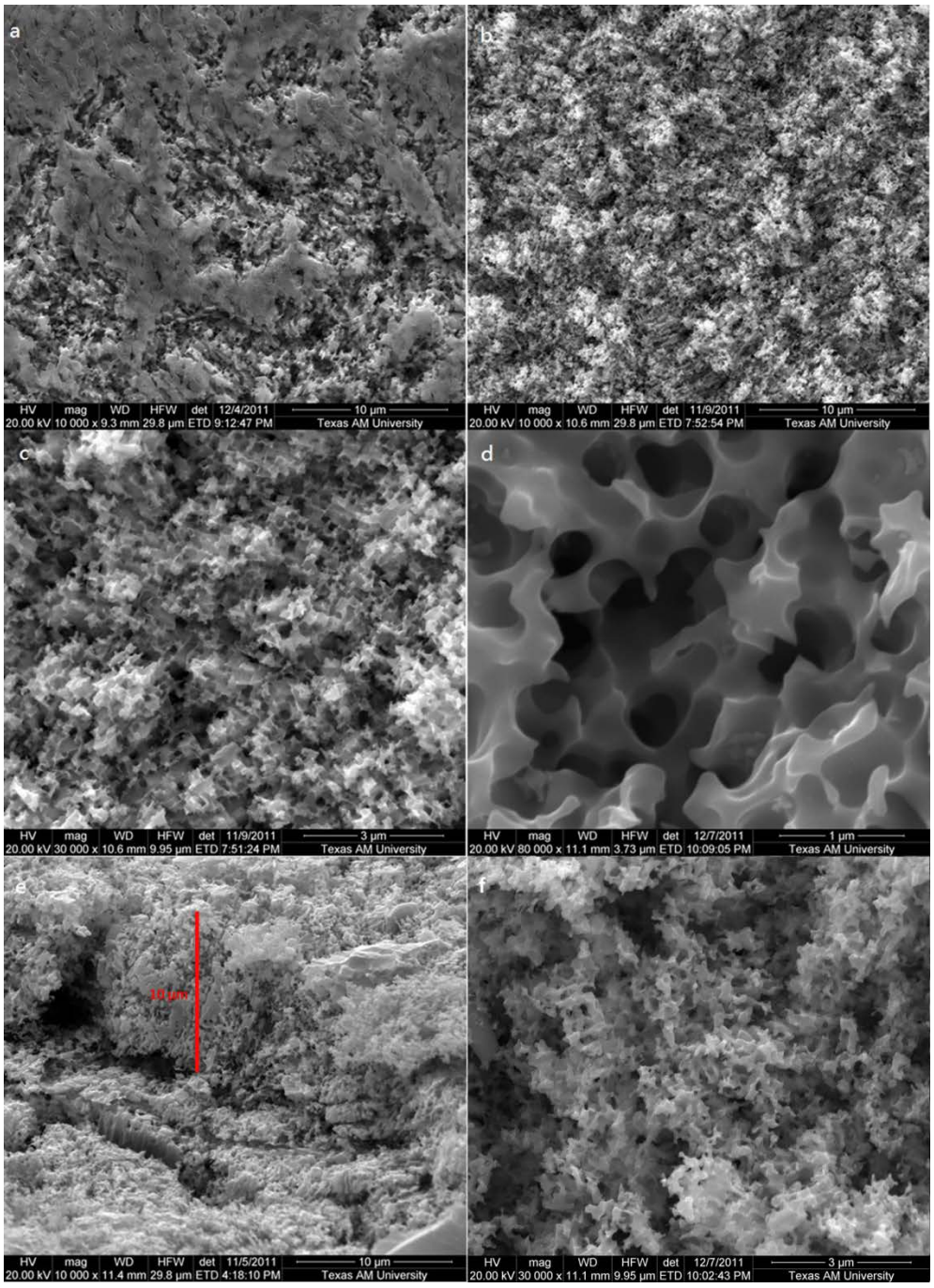

Figure 40 SEM images of dealloyed nanoporous structures

6.3 Discussion and Conclusion

Fig. 40a shows the surface morphology after dealloying at 0.9 V for 1 hour. Nanoporous structure can be formed, but there are still some islands on top of alloy, and these islands are the remaining protecting oxide. Fig. 40b shows SEM image of the nanoporous structure that was dealloyed at 3 V for 2 min and at 0.9 V for 1 hour. In this high voltage to low voltage process, the protecting oxide was first entirely removed and then nickel was selectively etched away at a constant low voltage. Fig. 40b, c and d show the nanoporous structure, pores are around 50 to 100 nm in size and well distributed. Fig. 40e and f show side and top views of the nanoporous TiO_2 after anodization and annealling. Fig. 40e shows a side view of dealloyed titanium nanoporous structure. After 1 hr dealloying, the depth of nanoporous structure is around 10 μm. After growing TiO_2 on the nanoporous structure, uniform nanoporous structure still can be obtained. However, the pores are smaller than dealloyed sample due to the covering TiO_2 on Ti (Fig. 40f).

Table 3 shows composition changes with different dealloying process. EDS was conducted to observe the composition changes during SEM observation. All-low-voltage (LV) process is not able to remove the protecting oxide efficiently, and there are some islands in Fig. 40a. Therefore, nickel quantity was not decreased as expected because part of nitinol was not etched with protecting oxide on top of it. In high-to-low voltage (HV-LV) process, the EDS result shows that there was very little amount of nickel left in the structure. It also can demonstrate a more uniform nanoporous structure without islands in Fig. 40b and c is a continuous titanium network.

Table 3 Composition of Ti/Ni alloy

	Raw (at %)	LV (at %)	HV-LV (at %)
Ti	49.03	55.15	86.81
Ni	50.97	44.85	13.19

The XRD patterns of raw nitinol, dealloyed nanostructure, anodized, and annealed sample were showed in Fig. 41. The pattern of raw nitinol presented two peaks at 42.3^{o} and 44.4^{o} are NiTi and TiO_2, respectively. Raw nitinol wire was finished with a commercial protecting oxide, and it indicated that the oxide was TiO_2 from the surface Ti. This is because the high oxygen affinity of titanium is responsible for the formation of oxide films on NiTi raw material. [195] These films are effective barriers against corrosion or nickel ion release to protect the alloy. The pattern of dealloyed sample showed a peak at 38.3^{o} which presented pure Ti, but the peak of TiO_2 at 44.4^{o} was disappeared because the protecting oxide was removed during the dealloying process. The pre-annealing pattern showed the sample was anodized in 1 M sulfuric acid at 20 V for 10 sec at room temperature, peak of TiO_2 appeared again. The annealed pattern revealed the peak of TiO_2 was getting stronger after annealing at 450^{o}C for 30 min.

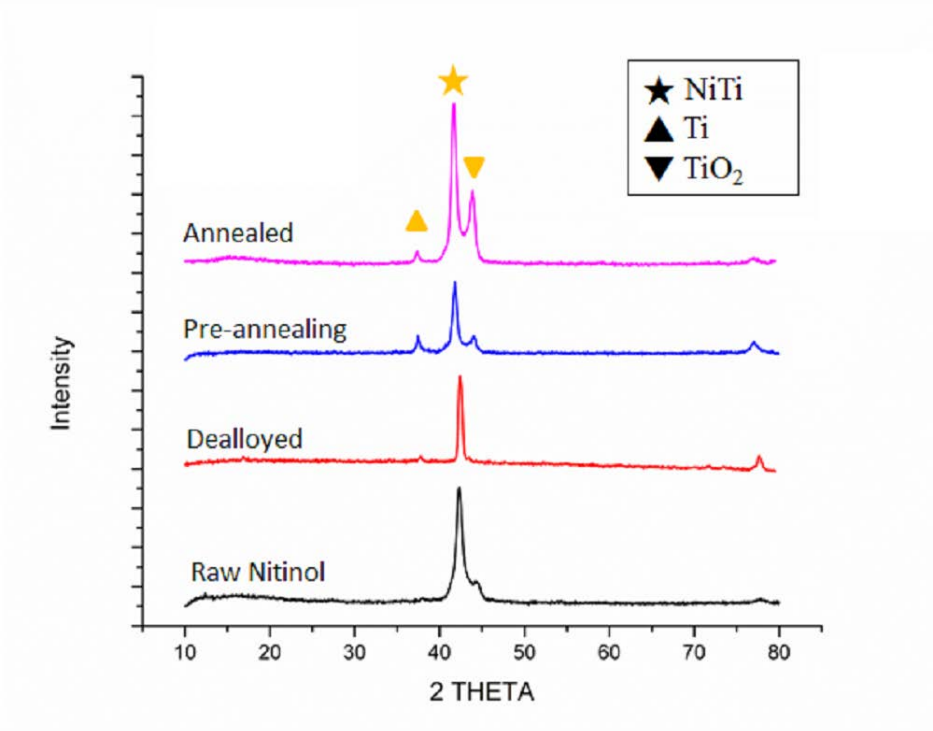

Figure 41 XRD results of raw nitinol, dealloyed nitinol, pre-annealing and annealed samples

Cyclic voltammograms (CV) is used to characterize the capacitors behavior. The test samples were immersed 1 cm into 1 M sulfuric acid. Fig. 42 shows a CV curve of anodized raw nitinol, anodized dealloyed sample, and dealloyed-anodized-annealed sample. Annealed nanoporous TiO_2 after annealing has the best capacitance performance in Fig. 42. The specific capacitance (C) can be measured by voltage step, current step, or voltage ramp methods, and evaluated by the equations of, $C = Q/V$, or $C = dQ/dV$. V is applied voltage and Q is the quantity of charge on the electrode (which can be evaluated from the area of the CV curve). For the annealed nanoporous TiO_2 CV curve, the capacitance is 7.01 mF. Moreover, the specific capacitance can be calculated by estimating the mass of this supercapacitor. The thickness of TiO_2 dielectric is 8 nm after 1 s at 20 V in 1 M phosphoric

acid. [196] The reacting surface area can be calculated by the porous structure. The volume ratio of Ni to Ti is about 1:1, so the total vacancy volume (V) of the porous structure is 1.33 x 10^{-5} cm^3 after removing 85% nickel from the EDX results shown in Table 1. Therefore, there are 2.55 x 10^{10} pores (N) in the dealloyed structure by $N = \frac{V}{\frac{4}{3}\pi r^3}$, where the average pore size is 100 nm (r = 50 nm). (Fig. 1d) Hence, the total surface area (A) of nanoporous structure is 80.1 cm^2 from $A = 4\pi r^2 x\, N$. Thus, the mass of the supercapacitor with 8 nm TiO_2 layer is 1.98 x 10^{-4} g. The specific capacitance (Cs) can be calculated by equation of $Cs = \frac{dQ}{dV \times M}$ or Cs = C/M, where M is mass of dielectric loading. As the result, the specific capacitance for the annealed nanoporous TiO_2 supercapacitor is 35.5 F/g.

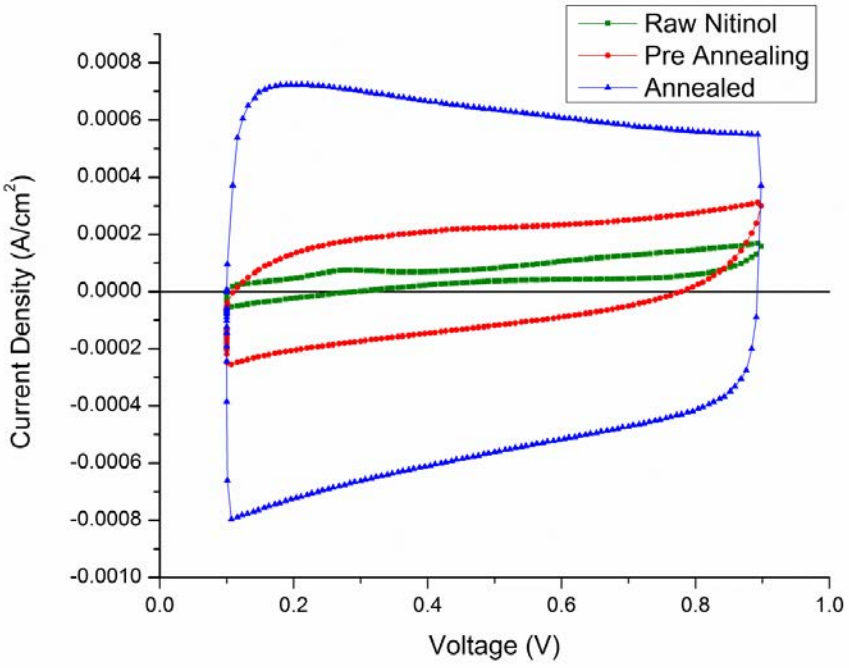

Figure 42 Cyclic Voltammogram (CV) curve of raw nitinol, pre-annealing, and annealed samples

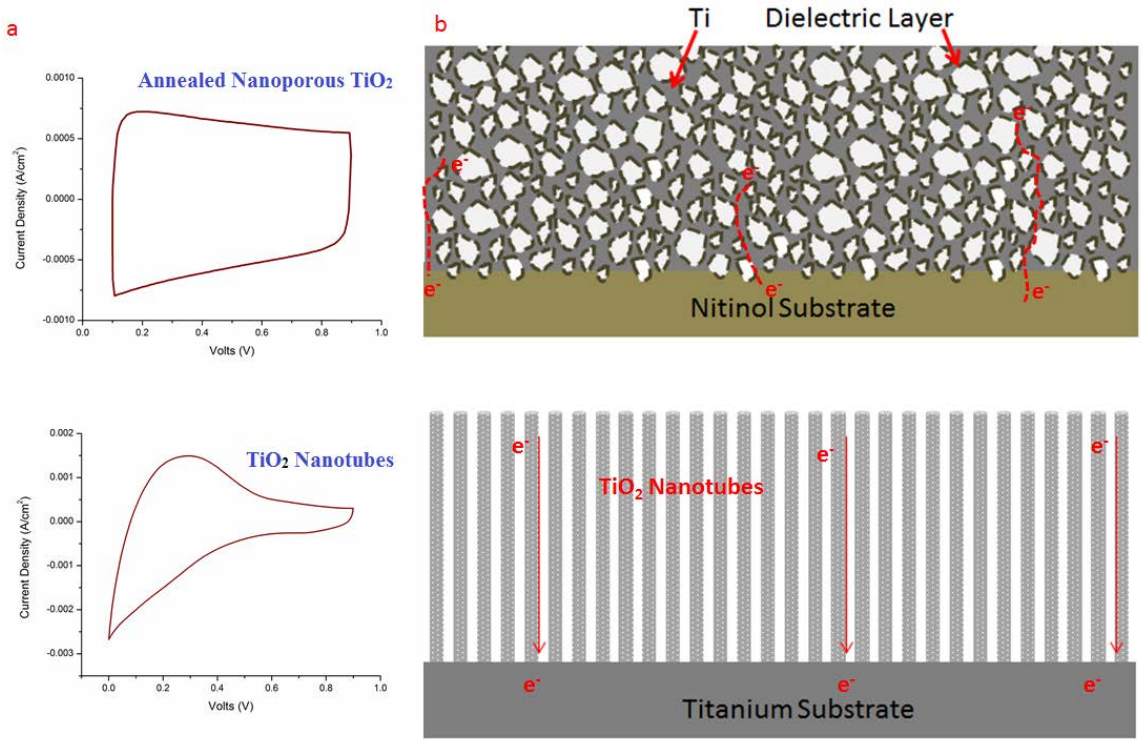

Figure 43 (a) C-V curves and (b) schematic diagrams of structures comparison with dealloyed nanoporous TiO_2 and TiO_2 nanotubes

The specific capacitance of the dealloying TiO_2 nanoporous supercapacitor is higher than the specific capacitance of TiO_2 nanotube (Cs = 11.8 F/g). Moreover, the curve of annealed sample at the x-axis intercept in Fig. 43a is nearly vertical and much steeper compared with the curve of TiO_2 nanotubes. Fig. 43b shows a schematic diagram for these types of supercapacitors. The electrons transport is along the nanotubes to the bottom electrode (Red arrow in Fig. 43b), therefore, it causes an inefficient charge/discharge route due to the high-aspect-ratio nanotubes. On the other hand, the continuous Ti nanoporous network is covered by a very thin layer of TiO_2 after anodization and heat treatment. The electrons transmission path is much shorter, thus, the results show that the dealloyed Ti nanoporous supercapacitor is able to charge/discharge faster and more efficiently.

In this section, high surface area nanoporous Ti/TiO_2 structure was fabricated by a simple electrochemical process. Superelastic shape memory alloy “Nitinol” wire was used in this experiment, and nickel was removed from the alloy. Nanoporous structure with average diameter of 100 nm. Nanoporous TiO_2 has nice capacitance performance and the specific capacitance is 35.5 F/g. Additionally, nanoporous TiO_2 supercapacitor has better capacitor behavior than TiO_2 nanotube supercapacitor does. The path for electron transport is efficient because there is a continuous metal network in the nanoporous structure. This structure can be potentially converting to high-k dielectric, such as $BaTiO_3$. Therefore, dealloying nanoporous structure can be developed to build an all-solid-state ultracapacitor. The titanium nanoporous structure with continuous advantage can be developed for many applications, such as catalysts, sensors, and energy materials, etc.

7. SUMMARY AND FUTURE WORK

7.1 Summary

This dissertation is a study to propose the ideas of the developments of energy storage and sensor applications by anodic processes. Through extensive experiments we were able to demonstrate that the anodization techniques can be applied to generate various types of nanomaterials. The knowledge and techniques necessary to create “anodized nanostructures” were also established in this dissertation. This study stated that 1) fabricating microneedle and its array by anodization processes. The enormous surface areas can be used to build chemical sensors and potentially biosensing and drug delivery devices, as shown in Section 3; 2) the development of innovative AAO templates with nanoimprint assisted. AAO also can be used as templates to produce metal, ceramic, and polymer ordered nanostructures, as presented in Section 4; 3) the supercapacitors applications of TiO_2 nanostructures formed by low-cost electrochemical anodization processes, as shown in Section 5 and 6. Based on the results shown in this study, the conclusions can be drawn in four main aspects: developments of fabrication process, various anodized nanostructures, chemical sensor detection characterics, and energy storage applications. Several achievements are summarized as follows:

A) Developments of Fabrication Processes

- The electrochemical micromachining process, a cost effective fabrication alternative to semiconductor photolithography process, was employed to construct a three-dimensional micro/nano structures.

- Fabrication of AAO templates with a nanoimprint mold led to an innovative breakthrough which overcame the limitations for traditional AAO manufacturing process.

B) Anodized Nanostructures

- Surface area of the microneedle and its array was maximized through anodization processes to obtain nanoporous structures further shorten the reaction time.
- AAO templates with controllable pore sizes, locations, inter-pore distances, and pore densities were established by integrating anodization and nanoimprint processes.
- We combined various fabrication techniques to form nanostructures of metal (Ni), ceramics (TiO_2 and $BaTiO_3$) and polymer (UHMWPE) with AAO templates. Application of the fabrication techniques also led to the production of Ni nanowires/ TiO_2 nanotubes and Ni/$BaTiO_3$ core-shell nanotubes.
- Ti nanoporous structure, which has average diameter of 100 nm with a continuous metallic network, was produced by conducting an electrochemical dealloying process.

C) Detection Characterization

- Al rods and needles were coated with AAO on the surfaces in order to absorb indicators for pH detection. The Al tips used for detection were less than 1 μm which is smaller than the pores on human skin. This further demonstrates the potential of the detecting microtips as biological detectors.
- A 3-D microneedle array with 400 microneedles on a 1 cm Al substrate provides an enormous surface area that can potentially be applied on drug delivery system and body fluids extraction applications.

D) Energy Storage Applications

- Supercapacitors from various Ti based alloys were anodized to form highly ordered anodic oxide nanotubes. The capacity of the Ti based alloys oxides nanotubes were close to two times the capacity comparing to pure TiO_2 nanotubes.

- Improvements on the supercapcitor led to the continuous nanoporous Ti/TiO_2 supercapacitor that has 35.5 F/g of the specific capacitance. It has a better capacitor behavior than ordered TiO_2 nanotubes array supercapacitor due to the more efficient path for electron transport with a continuous metallic network.

7.2 Future Work

Many advances are required to achieve our ultimate goal of applying anodization processes to the fabrication on nanomaterials for energy storage and biological applications. These include several aspects listed below:

- Explore alternate material, such as Ti, W and Ta, that can be anodized to form microneedles since Al microneedles are soft even when covered with ceramic layers (AAO).
- Develop a more efficient and accurate system to produce the Al micropillar arrays for further electrochemical micromachining process to form better microneedle arrays.
- Based on the results of the nanoimprint mold for AAO fabrication, we are going to continue seeking for an easier process, such as anisotropic etching of Si, to generate a larger imprinting mold in place of nanoimprinting mold made by e-beam lithography.
- Utilize the highly-ordered core-shell nanowires and nanotubes array to build all-solid-state capacitors.
- The continuous metallic network structure of the TiO_2 nanoporous form can be further developed into an all-solid-state capacitor, and provide enormous surface area to increase metal-insulator interface. Furthermore, the TiO_2 dielectric layer can be converted into $BaTiO_3$, which has a dielectric constant of 1500, in order to enlarge the capacitance.

REFERENCES

1. Kramer, D., R.N. Viswanath, and J. Weissmüller, *Surface-stress induced macroscopic bending of nanoporous gold cantilevers.* Nano Lett., 2004. **4**(5): p. 793-796.
2. Ding, Y., M. Chen, and J. Erlebacher, *Metallic mesoporous nanocomposites for electrocatalysis.* J. Am. Chem. Soc., 2004. **126**(22): p. 6876-6877.
3. Qian, L.-H., Y. Ding, T. Fujita, and M.-W. Chen, *Synthesis and optical properties of three-dimensional porous core-shell nanoarchitectures.* Langmuir, 2008. **24**(9): p. 4426-4429.
4. Lang, X., L. Qian, P. Guan, J. Zi, and M. Chen, *Localized surface plasmon resonance of nanoporous gold.* Appl. Phys. Lett., 2011. **98**(9): p. 093701-093701-3.
5. Gu, X., L. Xu, F. Tian, and Y. Ding, *Au-Ag alloy nanoporous nanotubes.* Nano Res., 2009. **2**(5): p. 386-393.
6. Lang, X., A. Hirata, T. Fujita, and M. Chen, *Nanoporous metal/oxide hybrid electrodes for electrochemical supercapacitors.* Nature Nanotech., 2011. **6**(4): p. 232-236.
7. Wada, T., A.D. Setyawan, K. Yubuta, and H. Kato, *Nano-to submicro-porous β-Ti alloy prepared from dealloying in a metallic melt.* Scripta Materialia, 2011. **65**(6): p. 532-535.
8. Huang, Y.-J., C.-H. Lai, and P.-W. Wu, *Fabrication of large-area colloidal crystals by electrophoretic deposition in vertical arrangement.* Electrochemical and Solid-State Lett., 2008. **11**(12): p. P20-P22.
9. Erlebacher, J., M.J. Aziz, A. Karma, N. Dimitrov, and K. Sieradzki, *Evolution of nanoporosity in dealloying.* Nature, 2001. **410**(6827): p. 450-453.
10. Huang, Y.-J., C.-H. Lai, P.-W. Wu, and L.-Y. Chen, *Ni inverse opals for water electrolysis in an alkaline electrolyte.* J. Electrochem. Soc., 2010. **157**(3): p. P18-P22.
11. Huang, Y.-J., C.-H. Lai, P.-W. Wu, and L.-Y. Chen, *A facile approach to fabricate Ni inverse opals at controlled thickness.* Mater. Lett., 2009. **63**(27): p. 2393-2395.

12. Huang, J.F. and I.W. Sun, *Fabrication and surface functionalization of nanoporous gold by electrochemical alloying/dealloying of Au–Zn in an ionic liquid, and the self-assembly of L-Cysteine monolayers.* Adv. Func. Mater., 2005. **15**(6): p. 989-994.
13. Renner, F.U., Y. Gründer, P.F. Lyman, and J. Zegenhagen, *In-situ X-ray diffraction study of the initial dealloying of Cu3Au(001) and Cu0.83Pd0.17(001).* Thin Solid Films, 2007. **515**(14): p. 5574-5580.
14. Ding, Y., Y.J. Kim, and J. Erlebacher, *Nanoporous gold leaf:"Ancient technology"/advanced material.* Adv. Mater., 2004. **16**(21): p. 1897-1900.
15. Thorp, J.C., K. Sieradzki, L. Tang, P.A. Crozier, A. Misra, M. Nastasi, D. Mitlin, and S.T. Picraux, *Formation of nanoporous noble metal thin films by electrochemical dealloying of Pt[sub x]Si[sub 1−x].* Appl. Phys. Lett., 2006. **88**(3): p. 033110.
16. Pugh, D., A. Dursun, and S. Corcoran, *Formation of nanoporous platinum by selective dissolution of Cu from Cu0. 75Pt0. 25.* J. of Mater. Res., 2003. **18**(1): p. 216-221.
17. Zhang, Q. and Z. Zhang, *On the electrochemical dealloying of Al-based alloys in a NaCl aqueous solution.* Phys. Chem. Chem. Phys., 2010. **12**(7): p. 1453-72.
18. Chmiola, J., G. Yushin, Y. Gogotsi, C. Portet, P. Simon, and P.-L. Taberna, *Anomalous increase in carbon capacitance at pore sizes less than 1 nanometer.* Science, 2006. **313**(5794): p. 1760-1763.
19. Largeot, C., C. Portet, J. Chmiola, P.-L. Taberna, Y. Gogotsi, and P. Simon, *Relation between the ion size and pore size for an electric double-layer capacitor.* J. Am. Chem. Soc., 2008. **130**(9): p. 2730-2731.
20. Chen, P.-C., S.-J. Hsieh, C.-C. Chen, and J. Zou, *Fabrication and characterization of chemically sensitive needle tips with aluminum oxide nanopores for pH indication.* Ceramics International, 2013. **39**(3): p. 2597-2600.
21. Chen, P.C., S.J. Hsieh, C.C. Chen, and J. Zou, *A three-dimensional enormous surface area aluminum microneedle array with nanoporous structure.* J. of Nanomater., 2013. **2013**: p. 1.
22. Jolivet, J.-P., M. Henry, and J. Livage, *Metal oxide chemistry and synthesis: from solution to oxide*. 2000: John Wiley New York.

23. McMullan, D., *Scanning electron microscopy 1928–1965.* Scanning, 1995. **17**(3): p. 175-185.
24. Náray-Szabó, I., L. Zsoldos, and A. Kálmán, *Introduction to XRD Structure Investigation.* 1965: Association of Hungarian Chemists Budapest.
25. Goldstein, J., D.E. Newbury, D.C. Joy, C.E. Lyman, P. Echlin, E. Lifshin, L. Sawyer, and J.R. Michael, *Scanning electron microscopy and X-ray microanalysis*. 2003: Springer New York.
26. Revie, R.W. and H.H. Uhlig, *Passivity*, in *Corrosion and Corrosion Control*. 2008: John Wiley & Sons, Inc. New York.
27. Gaul, E. and Gaul, *Coloring titanium and related metals by electrochemical oxidation.* J. of Chem. Edu., 1993. **70**(3): p. 176.
28. Chen, C.-C., D. Fang, and Z. Luo, *Fabrication and characterization of highly-ordered valve-metal oxide nanotubes and their derivative nanostructures.* Reviews in Nanosci. and Nanotech., 2012. **1**(4): p. 229-256.
29. Oh, J. and C.V. Thompson, *The role of electric field in pore formation during aluminum anodization.* Electrochim. Acta, 2011. **56**(11): p. 4044-4051.
30. Thamida, S.K. and H.C. Chang, *Nanoscale pore formation dynamics during aluminum anodization.* Chaos, 2002. **12**(1): p. 240-251.
31. Mardilovich, P.P., A.N. Govyadinov, N.I. Mukhurov, A.M. Rzhevskii, and R. Paterson, *New and modified anodic alumina membranes Part I. Thermotreatment of anodic alumina membranes.* J. Membr. Sci., 1995. **98**(1–2): p. 131-142.
32. Ono, S., M. Saito, M. Ishiguro, and H. Asoh, *Controlling factor of self-ordering of anodic porous alumina.* J. Electrochem. Soc., 2004. **151**(8): p. B473-B478.
33. Lee, W., R. Ji, U. Goesele, and K. Nielsch, *Fast fabrication of long-range ordered porous alumina membranes by hard anodization.* Nature Mater., 2006. **5**(9): p. 741-747.
34. Lee, W., K. Schwirn, M. Steinhart, E. Pippel, R. Scholz, and U. Goesele, *Structural engineering of nanoporous anodic aluminium oxide by pulse anodization of aluminium.* Nature Nanotech., 2008. **3**(4): p. 234-239.
35. Lee, J. and J. Lee, *Ideally ordered anodic aluminum oxide membranes via the replicated nickel imprint stamp.* Adv. Sci. Lett., 2010. **3**(4): p. 411-414.

36. Liu, C.Y., A. Datta, and Y.L. Wang, *Ordered anodic alumina nanochannels on focused-ion-beam-prepatterned aluminum surfaces.* Appl. Phys. Lett., 2001. **78**(1): p. 120-122.

37. Masuda, H., K. Kanezawa, and K. Nishio, *Fabrication of ideally ordered nanohole arrays in anodic porous alumina based on nanoindentation using scanning probe microscope.* Chem. Lett., 2002(12): p. 1218-1219.

38. Mikulskas, I., S. Juodkazis, R. Tomasiunas, and J.G. Dumas, *Aluminum oxide photonic crystals grown by a new hybrid method.* Adv. Mater., 2001. **13**(20): p. 1574-+.

39. Masuda, H., Y. Matsui, M. Yotsuya, F. Matsumoto, and K. Nishio, *Fabrication of highly ordered anodic porous alumina using self-organized polystyrene particle array.* Chem. Lett., 2004. **33**(5): p. 584-585.

40. Lee, W., R. Ji, C.A. Ross, U. Gosele, and K. Nielsch, *Wafer-scale Ni imprint stamps for porous alumina membranes based on interference lithography.* Small, 2006. **2**(8-9): p. 978-982.

41. Kwon, N., K. Kim, J. Heo, and I. Chung, *Fabrication of ordered anodic aluminum oxide with matrix arrays of pores using nanoimprint.* J. of Vac. Sci. & Tech. A Vac., Surfaces, and Films, 2009. **27**(4): p. 803-807.

42. Choi, J., R.B. Wehrspohn, and U. Gosele, *Mechanism of guided self-organization producing quasi-monodomain porous alumina.* Electrochim. Acta, 2005. **50**(13): p. 2591-2595.

43. Noh, K., C. Choi, J.Y. Kim, Y. Oh, K.S. Brammer, M.C. Loya, and S.H. Jin, *Long-range ordered aluminum oxide nanotubes by nanoimprint-assisted aluminum film surface engineering.* J. Vac. Sci. Technol. B, 2010. **28**(6): p. C6M88-C6M92.

44. Yoo, H.S., T.G. Kim, and T.G. Park, *Surface-functionalized electrospun nanofibers for tissue engineering and drug delivery.* Adv. Drug Deliv. Rev., 2009. **61**(12): p. 1033-1042.

45. Jenekhe, S.A. and X.L. Chen, *Self-assembly of ordered microporous materials from rod-coil block copolymers.* Science, 1999. **283**(5400): p. 372-375.

46. Mercier, L. and T.J. Pinnavaia, *Direct synthesis of hybrid organic-inorganic nanoporous silica by a neutral amine assembly route: Structure-function control by*

stoichiometric incorporation of organosiloxane molecules. Chem. Mat., 2000. **12**(1): p. 188-196.

47. Crouse, D., Y.H. Lo, A.E. Miller, and M. Crouse, *Self-ordered pore structure of anodized aluminum on silicon and pattern transfer.* Appl. Phys. Lett., 2000. **76**(1): p. 49-51.
48. Sun, Z.J. and H.K. Kim, *Growth of ordered, single-domain, alumina nanopore arrays with holographically patterned aluminum films.* Appl. Phys. Lett., 2002. **81**(18): p. 3458-3460.
49. Jones, S.E., S.A. Ditner, C. Freeman, C.J. Whitaker, and M.A. Lock, *Comparison of a new inorganic membrane-filter (anopore) with a track-etched polycarbonate membrane-filter (nuclepore) for direct counting of bacteria.*Appl. Environ. Microbiol., 1989. **55**(2): p. 529-530.
50. Durtschi, J.D., M. Erali, M.G. Herrmann, M.G. Elgort, K.V. Voelkerding, and R.E. Smith, *Optically improved aluminum oxide membrane through electroless Ni modification.* J. Membr. Sci., 2005. **248**(1-2): p. 81-87.
51. Ingham, C.J., A. Sprenkels, J. Bomer, D. Molenaar, A. van den Berg, J.E. van Hylckama Vlieg, and W.M. de Vos, *The micro-Petri dish, a million-well growth chip for the culture and high-throughput screening of microorganisms.* Proceedings of the National Academy of Sciences, 2007. **104**(46): p. 18217-18222.
52. Vlassiouk, I., P. Takmakov, and S. Smirnov, S*ensing DNA hybridization via ionic conductance through a nanoporous electrode.* Langmuir, 2005. **21**: p. 3.
53. Park, B.G., W. Lee, J.S. Kim, and K.B. Lee, *Superhydrophobic fabrication of anodic aluminum oxide with durable and pitch-controlled nanostructure.* Colloid Surf. A-Physicochem. Eng. Asp., 2010. **370**(1-3): p. 15-19.
54. Matsumoto, F., K. Nishio, and H. Masuda, *Flow-through-type DNA array based on ideally ordered anodic porous alumina substrate.* Adv. Mater., 2004. **16**(23-24): p. 2105-+.
55. Kang, B., U. Yeo, and K.H. Yoo, *Anodized aluminum oxide-based capacitance sensors for the direct detection of DNA hybridization.* Biosensors & Bioelectronics, 2010. **25**(7): p. 1592-6.

56. Kim, D.-K., K. Kerman, M. Saito, R.R. Sathuluri, T. Endo, S. Yamamura, Y.-S. Kwon, and E. Tamiya, *Label-free DNA biosensor based on localized surface plasmon resonance coupled with interferometry.* Anal. Chem., 2007. **79**(5): p. 1855-1864.

57. Tian, Z.Q., B. Ren, and D.Y. Wu, *Surface-enhanced Raman scattering: From noble to transition metals and from rough surfaces to ordered nanostructures.* J. Phys. Chem. B, 2002. **106**(37): p. 9463-9483.

58. Tsou, P.H., H. Sreenivasappa, S.M. Hong, M. Yasuike, H. Miyamoto, K. Nakano, T. Misawa, and J. Kameoka, *Rapid antibiotic efficacy screening with aluminum oxide nanoporous membrane filter-chip and optical detection system.* Biosensors & Bioelectronics, 2010. **26**(1): p. 289-294.

59. Zhang, C., A. Smirnov, D. Hahn, and H. Grebel, *Surface enhanced Raman scattering of biospecies on anodized aluminum oxide films.* Chem. Phys. Lett., 2007. **440**(4): p. 239-243.

60. Grimm, S., R. Giesa, K. Sklarek, A. Langner, U. Gösele, H.-W. Schmidt, and M. Steinhart, *Nondestructive replication of self-ordered nanoporous alumina membranes via cross-linked polyacrylate nanofiber arrays.* Nano Lett., 2008. **8**(7): p. 1954-1959.

61. Chen, P.C., Y.M. Chang, P.W. Wu, and Y.F. Chiu, *Fabrication of Ni nanowires for hydrogen evolution reaction in a neutral electrolyte.* Int. J. Hydrog. Energy, 2009. **34**(16): p. 6596-6602.

62. Buyukserin, F. and C.R. Martin, *The use of Reactive Ion Etching for obtaining "free" silica nano test tubes.* Appl. Surf. Sci., 2010. **256**(24): p. 7700-7705.

63. De La Vega, J.C., P. Elischer, T. Schneider, and U.O. Hafeli, *Uniform polymer microspheres: monodispersity criteria, methods of formation and applications.* Nanomedicine, 2013. **8**(2): p. 265-285.

64. Liu, Y.H., Y.Y. Tsai, H.J. Chien, C.Y. Chen, Y.F. Huang, J.S. Chen, Y.C. Wu, and C.C. Chen, *Quantum-dot-embedded silica nanotubes as nanoprobes for simple and sensitive DNA detection.* Nanotech., 2011. **22**(15).

65. Liu, L., N.-q. Jia, Q. Zhou, M.-m. Yan, and Z.-y. Jiang, *Electrochemically fabricated nanoelectrode ensembles for glucose biosensors.* Mater. Sci. and Eng.: C, 2007. **27**(1): p. 57-60.

66. Ansari, S., Z. Ansari, R. Wahab, Y.-S. Kim, G. Khang, and H.-S. Shin, *Glucose sensor based on nano-baskets of tin oxide templated in porous alumina by plasma enhanced CVD.* Biosensors and Bioelectronics, 2008. **23**(12): p. 1838-1842.

67. Martin, F., R. Walczak, A. Boiarski, M. Cohen, T. West, C. Cosentino, and M. Ferrari, *Tailoring width of microfabricated nanochannels to solute size can be used to control diffusion kinetics.* J. of Controlled Release, 2005. **102**(1): p. 123-133.

68. Shi, W., Y. Shen, D. Ge, M. Xue, H. Cao, S. Huang, J. Wang, G. Zhang, and F. Zhang, *Functionalized anodic aluminum oxide (AAO) membranes for affinity protein separation.* J. Membr. Sci., 2008. **325**(2): p. 801-808.

69. Kwak, D.-H., J.-B. Yoo, and D.J. Kim, *Drug Release behavior from nanoporous anodic aluminum oxide.* J. of Nanosci. and Nanotech., 2010. **10**(1): p. 345-348.

70. Jeon, G., S.Y. Yang, and J.K. Kim, *Functional nanoporous membranes for drug delivery.* J. of Mater. Chem., 2012. **22**(30): p. 14814-14834.

71. Kang, H.-J., D.J. Kim, S.-J. Park, J.-B. Yoo, and Y. Ryu, *Controlled drug release using nanoporous anodic aluminum oxide on stent.* Thin Solid Films, 2007. **515**(12): p. 5184-5187.

72. Gong, D., V. Yadavalli, M. Paulose, M. Pishko, and C.A. Grimes, *Controlled molecular release using nanoporous alumina capsules.* Biomedical Microdevices, 2003. **5**(1): p. 75-80.

73. La Flamme, K.E., K.C. Popat, L. Leoni, E. Markiewicz, T.J. La Tempa, B.B. Roman, C.A. Grimes, and T.A. Desai, *Biocompatibility of nanoporous alumina membranes for immunoisolation.* Biomater., 2007. **28**(16): p. 2638-2645.

74. Noh, K., K.S. Brammer, C. Choi, S. Kim, C.J. Frandsen, and S. Jin, *A new nano-platform for drug release via nanotubular aluminum oxide.* J. of Biomater. and Nanobiotech., 2011. **2**(3): p. 226-233.

75. Yang, S.Y., J.-A. Yang, E.-S. Kim, G. Jeon, E.J. Oh, K.Y. Choi, S.K. Hahn, and J.K. Kim, *Single-file diffusion of protein drugs through cylindrical nanochannels.* ACS Nano, 2010. **4**(7): p. 3817-3822.

76. Losic, D. and S. Simovic, *Self-ordered nanopore and nanotube platforms for drug delivery applications.* Expert Opinion on Drug Delivery, 2009. **6**(12): p. 1363-1381.

77. Simovic, S., D. Losic, and K. Vasilev, *Controlled drug release from porous materials by plasma polymer deposition.* Chem. Commun., 2010. **46**(8): p. 1317-1319.
78. Vallet-Regí, M., F. Balas, and D. Arcos, *Mesoporous materials for drug delivery.* Angewandte Chemie International Edition, 2007. **46**(40): p. 7548-7558.
79. Lee, K.J., S.H. Min, and J. Jang, *Vapor-phase synthesis of mesostructured silica nanofibers inside porous alumina membranes.* Small, 2008. **4**(11): p. 1945-1949.
80. Schmaljohann, D., *Thermo-and pH-responsive polymers in drug delivery.* Adv. Drug Deliv. Rev., 2006. **58**(15): p. 1655-1670.
81. Son, S.J., J. Reichel, B. He, M. Schuchman, and S.B. Lee, *Magnetic nanotubes for magnetic-field-assisted bioseparation, biointeraction, and drug delivery.* J. Am. Chem. Soc., 2005. **127**(20): p. 7316-7317.
82. Kwon, I.C., Y.H. Bae, and S.W. Kim, *Electrically credible polymer gel for controlled release of drugs.* Nature, 1991. **354**: p291-293.
83. Jeon, G., S.Y. Yang, J. Byun, and J.K. Kim, *Electrically actuatable smart nanoporous membrane for pulsatile drug release.* Nano Letters, 2011. **11**(3): p. 1284-1288.
84. Nishino, A., *Capacitors: operating principles, current market and technical trends.* J. of Power Sources, 1996. **60**(2): p. 137-147.
85. Arlt, G. and D. Hennings, *Dielectric properties of fine-grained barium titanate ceramics.* J. of Appl. Phys., 1985. **58**(4): p. 1619-1625.
86. Neumann, H. and G. Arlt, *Maxwell-Wagner relaxation and degradation of SrTiO3 and BaTiO3 ceramics.* Ferroelectrics, 1986. **69**(1): p. 179-186.
87. Raju, G.G., *Dielectrics in electric fields*. 2003: CRC Press, Marcel Dekker New York.
88. Lewis, T., *Nanometric dielectrics.* Dielectrics and Electrical Insulation, IEEE Transactions on, 1994. **1**(5): p. 812-825.
89. Barber, P., S. Balasubramanian, Y. Anguchamy, S. Gong, A. Wibowo, H. Gao, H.J. Ploehn, and H.-C. Zur Loye, *Polymer composite and nanocomposite dielectric materials for pulse power energy storage.* Mater., 2009. **2**(4): p. 1697-1733.
90. Kim, P., S.C. Jones, P.J. Hotchkiss, J.N. Haddock, B. Kippelen, S.R. Marder, and J.W. Perry, *Phosphonic acid-modified barium titanate polymer nanocomposites with high permittivity and dielectric strength.* Adv. Mater., 2007. **19**(7): p. 1001-1005.

91. Banerjee, P., I. Perez, L. Henn-Lecordier, S.B. Lee, and G.W. Rubloff, *Nanotubular metal–insulator–metal capacitor arrays for energy storage.* Nature Nanotech., 2009. **4**(5): p. 292-296.
92. Niwa, S. and Y. Taketani, *Development of new series of aluminium solid capacitors with organic semiconductive electrolyte (OS-CON).* J. of Power Sources, 1996. **60**(2): p. 165-171.
93. Kastening, B., M. Hahn, B. Rabanus, M. Heins, and U. Zum Felde, *Electronic properties and double layer of activated carbon.* Electrochim. Acta, 1997. **42**(18): p. 2789-2799.
94. Frackowiak, E. and F. Beguin, *Carbon materials for the electrochemical storage of energy in capacitors.* Carbon, 2001. **39**(6): p. 937-950.
95. Liu, H. and G. Zhu, *The electrochemical capacitance of nanoporous carbons in aqueous and ionic liquids.* J. of Power Sources, 2007. **171**(2): p. 1054-1061.
96. Bleda-Martínez, M.J., J.A. Maciá-Agulló, D. Lozano-Castelló, E. Morallon, D. Cazorla-Amorós, and A. Linares-Solano, *Role of surface chemistry on electric double layer capacitance of carbon materials.* Carbon, 2005. **43**(13): p. 2677-2684.
97. Skowroński, J.M. and M. Osińska, *Effect of nickel catalyst on physicochemical properties of carbon xerogels as electrode materials for supercapacitor.* Current Appl. Phys., 2012. **12**(3): p. 911-918.
98. Snook, G.A., P. Kao, and A.S. Best, *Conducting-polymer-based supercapacitor devices and electrodes.* J. of Power Sources, 2011. **196**(1): p. 1-12.
99. Zhang, J., J. Ma, L.L. Zhang, P. Guo, J. Jiang, and X.S. Zhao, *Template synthesis of tubular ruthenium oxides for supercapacitor applications.* Journal of Physical Chemistry C, 2010. **114**(32): p. 13608-13613.
100. Xiao, Y., S. Liu, F. Li, A. Zhang, J. Zhao, S. Fang, and D. Jia, *3D hierarchical Co3O4 twin-spheres with an urchin-like structure: large-scale synthesis, multistep-splitting growth, and electrochemical pseudocapacitors.* Adv. Func. Mater., 2012. **22**(19): p. 4052-4059.
101. Bello, A., K. Makgopa, M. Fabiane, D. Dodoo-Ahrin, K.I. Ozoemena, and N. Manyala, *Chemical adsorption of NiO nanostructures on nickel foam-graphene for supercapacitor applications.* J. Mater. Sci., 2013. **48**(19): p. 6707-6712.

102. Zhu, G., L. Deng, J. Wang, L. Kang, and Z.-H. Liu, *Hydrothermal preparation and the capacitance of hierarchical MnO2 nanoflower*. Colloids and Surfaces A-Physicochemical and Eng. Aspects, 2013. **434**: p. 42-48.

103. Simon, P. and Y. Gogotsi, *Materials for electrochemical capacitors.* Nature materials, 2008. **7**(11): p. 845-854.

104. Zheng, J. and T. Jow, *High energy and high power density electrochemical capacitors.* J. of Power Sources, 1996. **62**(2): p. 155-159.

105. Wang, Y.G., Z.D. Wang, and Y.Y. Xia, *An asymmetric supercapacitor using RuO2/TiO2 nanotube composite and activated carbon electrodes.* Electrochim. Acta, 2005. **50**(28): p. 5641-5646.

106. Aricò, A.S., P. Bruce, B. Scrosati, J.-M. Tarascon, and W. Van Schalkwijk, *Nanostructured materials for advanced energy conversion and storage devices.* Nature Mater., 2005. **4**(5): p. 366-377.

107. Ragone, D., *Review of battery systems for electrically powered vehicles.* Energy, 1968. **2012**: p. 12-11.

108. Wu, F., J.N. Wu, S. Banerjee, O. Blank, and P. Banerjee. *Frontiers in applied atomic layer deposition (ALD) research*. in *Materials Science Forum*. 2013. Trans Tech Publ.

109. Wood, G. and J. O'Sullivan, *The anodizing of aluminium in sulphate solutions.* Electrochim. Acta, 1970. **15**(12): p. 1865-1876.

110. Tonucci, R.J., B.L. Justus, A.J. Campillo, and C.E. Ford, *Nanochannel array glass.* Science, 1992. **258**(5083): p. 783-785.

111. Wood, G.C., P. Skeldon, G.E. Thompson, and K. Shimizu, *A model for the incorporation of electrolyte species into anodic alumina.* J. Electrochem. Soc., 1996. **143**(1): p. 74-83.

112. Akahori, H., *Electron microscopic study of growing mechanism of aluminum anodic oxide film.* Journal of Electron Microscopy, 1961. **10**(3): p. 175-185.

113. Pang, Y.T., G.W. Meng, Q. Fang, and L.D. Zhang, *Silver nanowire array infrared polarizers.* Nanotechnology, 2003. **14**(1): p. 20-24.

114. Wang, Y.W., G.W. Meng, C.H. Liang, G.Z. Wang, and L.D. Zhang, *Magnetic properties of ordered FexAg1−x nanowire arrays embedded in anodic alumina membranes.* Chem. Phys. Lett., 2001. **339**(3–4): p. 174-178.

115. Stoleru, V.G. and E. Towe, *Optical properties of nanometer-sized gold spheres and rods embedded in anodic alumina matrices.* Appl. Phys. Lett., 2004. **85**(22): p. 5152-5154.

116. Park, B.G., W. Lee, J.S. Kim, and K.B. Lee, *Superhydrophobic fabrication of anodic aluminum oxide with durable and pitch-controlled nanostructure.* Colloids and Surfaces A: Physicochemical and Eng. Aspects, 2010. **370**(1): p. 15-19.

117. Buyukserin, F. and C.R. Martin, *The use of Reactive Ion Etching for obtaining "free" silica nano test tubes.* Applied Surface Science, 2010. **256**(24): p. 7700-7705.

118. Losic, D., M.A. Cole, B. Dollmann, K. Vasilev, and H.J. Griesser, *Surface modification of nanoporous alumina membranes by plasma polymerization.* Nanotech., 2008. **19**(24): p. 245704.

119. Wang, M., G. Meng, Q. Huang, M. Li, Z. Li, and C. Tang, *Fluorescence detection of trace PCB101 based on PITC immobilized on porous AAO membrane.* Analyst, 2011. **136**(2): p. 278-281.

120. Oki, A., M. Takai, H. Ogawa, Y. Takamura, T. Fukasawa, J. Kikuchi, Y. Ito, T. Ichiki, and Y. Horiike, *Healthcare chip for checking health condition from analysis of trace blood collected by painless needle.* Jpn. J. Appl. Phys. Part 1 - Regul. Pap. Short Notes Rev. Pap., 2003. **42**(6A): p. 3722-3727.

121. Ogawa, H., M. Nagai, J. Kikuchi, and Y. Horiike. *Blood painless collection system equipping detection functions for search of vein 7th Int*. in *Conf. Miniaturized Chem. and Biochemical Anal. Sys. (741–3 Squaw Valley, CA, USA)*. 2003.

122. Oka, K., S. Aoyagi, Y. Arai, Y. Isono, G. Hashiguchi, and H. Fujita, *Fabrication of a micro needle for a trace blood test.* Sensors and Actuators A- Phys., 2002. **97-8**: p. 478-485.

123. Khumpuang, S., M. Horade, K. Fujioka, and S. Sugiyama, *Geometrical strengthening and tip-sharpening of a microneedle array fabricated by X-ray lithography.* Microsystem Technologies-Micro-and Nanosystems-Information Storage and Processing Systems, 2007. **13**(3-4): p. 209-214.

124. Henry, S., D.V. McAllister, M.G. Allen, M.R. Prausnitz, and Ieee, *Micromachined needles for the transdermal delivery of drugs*. Micro Electro Mechanical Systems - Ieee Eleventh Annual International Workshop Proceedings. 1998. 494-498.

125. Foster, L.S. and I.J. Gruntfest, *Demonstration experiments using universal indicators.* J. of Chem. Edu., 1937. **14**(6): p. 274.

126. Rajaraman, S., S.-O. Choi, R.H. Shafer, J.D. Ross, J. Vukasinovic, Y. Choi, S.P. DeWeerth, A. Glezer, and M.G. Allen, *Microfabrication technologies for a coupled three-dimensional microelectrode, microfluidic array.* J. of Micromech. and Microeng., 2007. **17**(1): p. 163.

127. Takei, K., T. Kawashima, T. Kawano, H. Kaneko, K. Sawada, and M. Ishida, *Out-of-plane microtube arrays for drug delivery-liquid flow properties and an application to the nerve block test.* Biomed. Microdevices, 2009. **11**(3): p. 539-545.

128. Whitney, T.M., J.S. Jiang, P.C. Searson, and C.L. Chien, *Fabrication and magnetic-properties of arrays of metallic nanowires.* Science, 1993. **261**(5126): p. 1316-1319.

129. Stucky, G.D. and J.E. Macdougall, *Quantum confinement and hos guest chemistry - probing a new dimension.*Science, 1990. **247**(4943): p. 669-678.

130. Beck, J.S., J.C. Vartuli, W.J. Roth, M.E. Leonowicz, C.T. Kresge, K.D. Schmitt, C.T.W. Chu, D.H. Olson, E.W. Sheppard, S.B. McCullen, J.B. Higgins, and J.L. Schlenker, *A new family of mesoporous molecular-sieves prepared with liquid-crystal templates.* J. Am. Chem. Soc., 1992. **114**(27): p. 10834-10843.

131. Matsumoto, F., M. Harada, K. Nishio, and H. Masuda, *Nanometer-scale patterning of DNA in controlled intervals on a gold-disk array fabricated using ideally ordered anodic porous alumina.* Adv. Mater., 2005. **17**(13): p. 1609-1613.

132. Masuda, H., F. Hasegwa, and S. Ono, *Self-ordering of cell arrangement of anodic porous alumina formed in sulfuric acid solution.* J. Electrochem. Soc., 1997. **144**(5): p. L127-L130.

133. Chen, S.-H., C.-C. Chen, Z. Luo, and C.-G. Chao, *Fabrication and characterization of eutectic bismuth–tin (Bi–Sn) nanowires.* Mater. Lett., 2009. **63**(13): p. 1165-1168.

134. Bisrat, Y., Z. Luo, D. Davis, and D. Lagoudas, *Highly ordered uniform single-crystal Bi nanowires: fabrication and characterization.* Nanotech., 2007. **18**(39): p. 395601.

135. Márquez, F., C. Morant, T. Campo, J. Sanz, and E. Elizalde, *Ordered metal nanotube arrays fabricated by PVD.* J. of Nanosci. and Nanotech., 2010. **10**(2): p. 1115-1119.

136. Kim, W.-H., S.-J. Park, J.-Y. Son, and H. Kim, *Ru nanostructure fabrication using an anodic aluminum oxide nanotemplate and highly conformal Ru atomic layer deposition.* Nanotech., 2008. **19**(4): p. 045302.

137. Yen, J.-H., I.-C. Leu, M.-T. Wu, C.-C. Lin, and M.-H. Hon, *Effect of nanowire catalyst for carbon nanotubes growth by ICP-CVD.* Diamond and Related Mater., 2005. **14**(3): p. 841-845.

138. Lin, S.-C., C.-H. Lai, and P.-W. Wu, *Conformal deposition of Ni–P on anodic aluminum oxide template.* Electrochem. and Solid-State Lett., 2008. **11**(1): p. D1-D4.

139. Wang, L.S., X. Zhang, and F.H. Zeng. *Synthesis and characterization of ZnO nanowires using a simple PVD approach without catalysts*. *Mater. Sci. Forum*. 2005. Trans Tech Publ.

140. Bajpai, R., M. Zaghloul, D. Gu, H. Baumgart, and T. Abdel-Fattah. *Synthesis and assembly of ZnO nanorods grown by ALD for biosensor application*. in *Semiconductor Device Research Symposium, 2009. ISDRS'09. International*. 2009. IEEE.

141. Chen, Y.-Y., B.-Y. Yu, J.-H. Wang, R.E. Cochran, and J.-J. Shyue, *Template-based fabrication of $SrTiO_3$ and $BaTiO_3$ nanotubes.* Inorganic Chem., 2008. **48**(2): p. 681-686.

142. Cao, G. and D. Liu, *Template-based synthesis of nanorod, nanowire, and nanotube arrays.* Advances in Colloid and Interface Science, 2008. **136**(1): p. 45-64.

143. Song, G., X. She, Z. Fu, and J. Li, *Preparation of good mechanical property polystyrene nanotubes with array structure in anodic aluminum oxide template using simple physical techniques.* J. of Mater. Res., 2004. **19**(11): p. 3324-3328.

144. Chen, C.C., J.H. Chen, and C.G. Chao, *Post-treatment method of producing ordered array of anodic aluminum oxide using general purity commercial (99.7%) aluminum.* Jpn. J. Appl. Phys. Part 1 - Regul. Pap. Brief Commun. Rev. Pap., 2005. **44**(3): p. 1529-1533.

145. Belwalkar, A., E. Grasing, W. Van Geertruyden, Z. Huang, and W.Z. Misiolek, *Effect of processing parameters on pore structure and thickness of anodic aluminum oxide (AAO) tubular membranes.* J. Membr. Sci., 2008. **319**(1-2): p. 192-198.

146. Cross, L.E., *Ferroelectric materials for electromechanical transducer applications.* Materials Chemistry and Physics, 1996. **43**(2): p. 108-115.

147. Hilton, A. and R. Frost, *Recent developments in the manufacture of barium titanate powders.* Key Eng. Mater., 1992. **66**: p. 145-184.

148. Cross, L.E., *Ferroelectric ceramics: tailoring properties for specific applications*, *Ferroelectric ceramics*. 1993: Birkhauser Basel.

149. Pandey, D., A. Singh, and V. Tiwari, *Developments in ferroelectric ceramics for capacitor applications.* Bulletin of Materials Science, 1992. **15**(5): p. 391-402.

150. Kajiyoshi, K., N. Ishizawa, and M. Yoshimura, *Preparation of tetragonal barium titanate thin film on titanium metal substrate by hydrothermal method.* J. of the Am. Ceramic Soc., 1991. **74**(2): p. 369-374.

151. Horikawa, T., N. Mikami, T. Makita, J. Tanimura, M. Kataoka, K. Sato, and M. Nunoshita, *Dielectric properties of (Ba, Sr) TiO_3 thin films deposited by RF sputtering.* Jap. J. of Appl. Phys., 1993. **32**: p. 4126-4126.

152. Shaikh, A.S. and G.M. VEST, *Kinetics of $BaTiO_3$ and $PbTiO_3$ formation from metallo-organic precursors.* J. of Am. Ceramic Soc., 1986. **69**(9): p. 682-688.

153. Okamura, H. and H.K. Bowen, *Preparation of alkoxides for the synthesis of ceramics.* Ceramics International, 1986. **12**(3): p. 161-171.

154. Kirby, K.W., *Alkoxide synthesis techniques for $BaTiO_3$.* Mater. Res. Bulletin, 1988. **23**(6): p. 881-890.

155. Bhattacharya, P., T. Komeda, K. Park, and Y. Nishioka, *Comparative-study of amorphous and crystalline (Ba, Sr)TiO_3 thin-films deposited by laser-ablation.*Jpn. J. Appl. Phys. Part 1 - Regul. Pap. Short Notes Rev. Pap., 1993. **32**(9B): p. 4103-4106.

156. Tahan, D.M., A. Safari, and L.C. Klein, *Preparation and characterization of BaxSr1-xTiO3 thin films by a sol-gel technique.* J. of the Am. Ceramic Soc., 1996. **79**(6): p. 1593-1598.

157. Chen, C.C., J.H. Chen, C.G. Chao, and W.C. Say, *Electrochemical characteristics of surface of titanium formed by electrolytic polishing and anodizing.* J. Mater. Sci., 2005. **40**(15): p. 4053-4059.

158. Chen, C.-C., Y. Bisrat, Z. Luo, R. Schaak, C. Chao, and D. Lagoudas, *Fabrication of single-crystal tin nanowires by hydraulic pressure injection.* Nanotech., 2006. **17**(2): p. 367.

159. Tsuchiya, H. and P. Schmuki, *Self-organized high aspect ratio porous hafnium oxide prepared by electrochemical anodization.* Electrochem. Commun., 2005. **7**(1): p. 49-52.

160. Sieber, I., H. Hildebrand, A. Friedrich, and P. Schmuki, *Formation of self-organized niobium porous oxide on niobium.* Electrochem. Commun., 2005. **7**(1): p. 97-100.

161. Sieber, I., B. Kannan, and P. Schmuki, *Self-assembled porous tantalum oxide prepared in H2SO4/HF electrolytes.* Electrochem. Solid State Lett., 2005. **8**(3): p. J10-J12.

162. Mukherjee, N., M. Paulose, O.K. Varghese, G.K. Mor, and C.A. Grimes, *Fabrication of nanoporous tungsten oxide by galvanostatic anodization.* J. of Mater. Res., 2003. **18**(10): p. 2296-2299.

163. Stefanovich, G.B., A.L. Pergament, A.A. Velichko, and L.A. Stefanovich, *Anodic oxidation of vanadium and properties of vanadium oxide films.* J. of Physics-Condensed Matter, 2004. **16**(23): p. 4013-4024.

164. Shrestha, N.K., Y.-C. Nah, H. Tsuchiya, and P. Schmuki, *Self-organized nano-tubes of TiO2-MoO3 with enhanced electrochromic properties.* Chem. Comm., 2009(15): p. 2008-2010.

165. Paramasivam, I., Y.-C. Nah, C. Das, N.K. Shrestha, and P. Schmuki, *WO_3/TiO_2 Nanotubes with strongly enhanced photocatalytic activity.* Chem.-A Euro. J., 2010. **16**(30): p. 8993-8997.

166. Ghicov, A., S. Aldabergenova, H. Tsuchyia, and P. Schmuki, *TiO_2-Nb_2O_5 nanotubes with electrochemically tunable morphologies.* Angewandte Chemie-International Edition, 2006. **45**(42): p. 6993-6996.

167. Yang, Y., D. Kim, M. Yang, and P. Schmuki, *Vertically aligned mixed V_2O_5-TiO_2 nanotube arrays for supercapacitor applications.* Chem. Comm., 2011. **47**(27): p. 7746-7748.

168. Jha, H., R. Hahn, and P. Schmuki, *Ultrafast oxide nanotube formation on TiNb, TiZr and TiTa alloys by rapid breakdown anodization.* Electrochim. Acta, 2010. **55**(28): p. 8883-8887.

169. Wei, W., S. Berger, N. Shrestha, and P. Schmuki, *Ideal hexagonal order: formation of self-organized anodic oxide nanotubes and nanopores on a Ti-35Ta alloy.* J. Electrochem. Soc., 2010. **157**(12): p. C409-C413.

170. Tsuchiya, H., S. Berger, J.M. Macak, A. Ghicov, and P. Schmuki, *Self-organized porous and tubular oxide layers on TiAl alloys.* Electrochem. Commun., 2007. **9**(9): p. 2397-2402.

171. Tilley, R., *Correlation between dielectric constant and defect structure of non-stoichiometric solids.* 1977.

172. Lin, J., N. Masaaki, A. Tsukune, and M. Yamada, *Ta2O5 thin films with exceptionally high dielectric constant.* Appl. Phys. Lett., 1999. **74**(16): p. 2370-2372.

173. Segawa, H., K. Mori, M. Itagaki, K. Sakurai, and T. Ishiwata, *Image sensing device*, 1985, Google Patents.

174. Pourbaix, M., *Atlas of electrochemical equilibria in aqueous solutions.* 1974.

175. Lai, C.W. and S. Sreekantan, *Effect of applied potential on the formation of self-organized TiO2 nanotube arrays and its photoelectrochemical response.* J. of Nanomater., 2011.

176. Lim, J.H. and J. Choi, *Titanium oxide nanowires originating from anodically grown nanotubes: the bamboo-splitting model.* Small, 2007. **3**(9): p. 1504-1507.

177. Tao, J., J. Zhao, X. Wang, Y. Kang, and Y. Li, *Fabrication of titania nanotube arrays on curved surface.* Electrochem. Commun., 2008. **10**(8): p. 1161-1163.

178. Kim, D., F. Schmidt-Stein, R. Hahn, and P. Schmuki, *Gravity assisted growth of self-organized anodic oxide nanotubes on titanium.* Electrochem. Commun., 2008. **10**(7): p. 1082-1086.

179. Bard, A.J. and L.R. Faulkner, *Electrochemical methods: fundamentals and applications*. Vol. 2. 1980: Wiley New York.

180. Wang, G., Z.Y. Liu, J.N. Wu, and Q. Lu, *Preparation and electrochemical capacitance behavior of TiO2-B nanotubes for hybrid supercapacitor.* Mater. Lett., 2012. **71**: p. 120-122.

181. Zhang, L., Y. Shi, S. Peng, J. Liang, Z. Tao, and J. Chen, *Dye-sensitized solar cells made from $BaTiO_3$-coated TiO_2 nanoporous electrodes.* J. of Photochem. and Photobio. A-Chem., 2008. **197**(2-3): p. 260-265.

182. Wei, X.Z., *Hydrothermal synthesis of $BaTiO_3$ thin films on nanoporous TiO_2 covered Ti substrates.* J. of Crystal Growth, 2006. **286**(2): p. 371-375.

183. Chen, C.-C., H.-W. Chung, C.-H. Chen, H.-P. Lu, C.-M. Lan, S.-F. Chen, L. Luo, C.-S. Hung, and E.W.-G. Diau, *Fabrication and characterization of anodic titanium oxide nanotube arrays of controlled length for highly efficient dye-sensitized solar cells.* J. of Phys. Chem. C, 2008. **112**(48): p. 19151-19157.

184. Zhang, J., J. Ma, L.L. Zhang, P. Guo, J. Jiang, and X. Zhao, *Template synthesis of tubular ruthenium oxides for supercapacitor applications.* J. of Phys. Chem. C, 2010. **114**(32): p. 13608-13613.

185. Wang, B., J.S. Chen, Z. Wang, S. Madhavi, and X.W.D. Lou, *Green synthesis of NiO nanobelts with exceptional pseudo-capacitive properties.* Adv. Energy Mater., 2012. **2**(10): p. 1188-1192.

186. Xiao, Y., S. Liu, F. Li, A. Zhang, J. Zhao, S. Fang, and D. Jia, *Hierarchical nanoarchitectures: 3D hierarchical Co3O4 twin-spheres with an urchin-like structure: large-scale synthesis, multistep-splitting growth, and electrochemical pseudocapacitors.* Adv. Func. Mater., 2012. **22**(19): p. 4051-4051.

187. Norlin, A., J. Pan, and C. Leygraf, *Investigation of electrochemical behavior of stimulation/sensing materials for pacemaker electrode applications II. Conducting oxide electrodes.* J. Electrochem. Soc., 2005. **152**(7): p. J85-J92.

188. Liang, H., F. Chen, R. Li, L. Wang, and Z. Deng, *Electrochemical study of activated carbon-semiconducting oxide composites as electrode materials of double-layer capacitors.* Electrochim. Acta, 2004. **49**(21): p. 3463-3467.

189. Chang, K.-H. and C.-C. Hu, *Hydrothermal synthesis of binary Ru–Ti oxides with excellent performances for supercapacitors.* Electrochim. Acta, 2006. **52**(4): p. 1749-1757.

190. Brousse, T., R. Marchand, P.-L. Taberna, and P. Simon, *TiO2 (B)/activated carbon non-aqueous hybrid system for energy storage.* J. of Power Sources, 2006. **158**(1): p. 571-577.

191. Wang, Y.-G., Z.-D. Wang, and Y.-Y. Xia, *An asymmetric supercapacitor using RuO2/TiO2 nanotube composite and activated carbon electrodes.* Electrochim. Acta, 2005. **50**(28): p. 5641-5646.
192. Walter Hassel, A., L. Neelakantan, A. Zelenkevych, A. Ruh, and M. Spiegel, *Selective de-alloying of NiTi by oxochloridation.* Corrosion Sci., 2008. **50**(5): p. 1368-1375.
193. Wu, C.-T. and F.-H. Lu, *Electrochemical deposition of barium titanate films using a wide electrolytic voltage range.* Thin Solid Films, 2001. **398**: p. 621-625.
194. Zhang, L., Y. Shi, S. Peng, J. Liang, Z. Tao, and J. Chen, *Dye-sensitized solar cells made from BaTiO3-coated TiO2 nanoporous electrodes.* J. of Photochem. and Photobio. A: Chem., 2008. **197**(2–3): p. 260-265.
195. Hassel, A., *Surface treatment of NiTi for medical applications.* Minimally Invasive Therapy & Allied Tech., 2004. **13**(4): p. 240-247.
196. Sul, Y.-T., C.B. Johansson, Y. Jeong, and T. Albrektsson, *The electrochemical oxide growth behaviour on titanium in acid and alkaline electrolytes.* Med. Eng. & Phys., 2001. **23**(5): p. 329-346.